Aerodynamic-Rotordynamic Interaction in Axial Compression Systems

by

Ammar Adnan Al-Nahwi

B.Sc., King Saud University, Riyadh (1990)
S.M., Massachusetts Institute of Technology (1996)

Submitted to the Department of Mechanical Engineering in partial fulfillment of the requirements for the degree of

Doctor of Philosophy

at the

Massachusetts Institute of Technology

September 2000

Author_____
Department of Mechanical Engineering
August 7, 2000

Certified by_____
Dr. James D. Paduano
Principal Research Engineer, Department of Aeronautics and Astronautics
Thesis Supervisor

Certified by_____
Kamal Youcef-Toumi
Professor of Mechanical Engineering
Thesis Committee Chairman

Accepted by_____
Ain A. Sonin
Professor of Mechanical Engineering
Chairman, Departmental Committee on Graduate Students

Aerodynamic-Rotordynamic Interaction in Axial Compression Systems

by

Ammar Adnan Al-Nahwi

Submitted to the Department of Mechanical Engineering
on August 7, 2000, in partial fulfillment of the
requirements for the degree of Doctor of Philosophy

Abstract

This thesis presents the first integrated treatment of the dynamic coupling between the flowfield (aerodynamics) and rotor structural vibration (rotordynamics) in axial compression systems. This work is motivated by documented observations of tip clearance effects on axial compressor flowfield stability, the destabilizing effect of fluid-induced aerodynamic forces on the rotordynamics, and their potential interaction. This thesis elucidates the nature of this interaction by extending the current understanding of aerodynamic forces acting on the rotor, identifying the main nondimensional design parameters governing this interaction, and assessing its impact on overall stability of the coupled system.

The model developed in this work employs a reduced-order Moore-Greitzer model for the flowfield and a Jeffcott-type model for the rotordynamics. The coupling between the fluid and structural dynamics is captured by incorporating a compressor pressure rise sensitivity to tip clearance, together with a momentum based model for the aerodynamic forces on the rotor. The resulting dynamic model suggests that the interaction is largely governed by two nondimensional parameters: the sensitivity of the compressor to tip clearance and the ratio of fluid mass to rotor mass.

A study of the aerodynamic forces reveals that they arise from three main contributions: turning, pressure, and unsteady effects. Simple, analytical relations are developed which allow these contributions as well as the net force to be evaluated in terms of a given compressor geometry and operating point. These relations indicate that aerodynamic forces are locked to the flowfield nonuniformity, and not to tip clearance asymmetry as is traditionally assumed.

The aerodynamic-rotordynamic coupling is shown to generally have an adverse effect on system stability. For a supercritical rotor and a typical value of the coupling parameter, the stability margin to the left of the design point is shown to decrease by about 5% in flow coefficient (from 20% for the uncoupled case). Doubling the value of the coupling parameter produces a reduction of about 8% in the stability margin, and also gives rise to rotordynamic instability at flow coefficients 7% higher than the design point.

A survey of the nonlinear post-instability behavior of the coupled system is presented, in which a variety of limit cycle type instabilities (such as rotor whirl, rotating stall and surge) are demonstrated, suggesting a rich dynamical character and highlighting several examples that can be the basis for future research.

Thesis Supervisor: Dr. James D. Paduano
Title: Principal Research Engineer, Department of Aeronautics and Astronautics

Acknowledgments

This is an attempt—an inevitably incomplete one—to acknowledge all those who contributed to my rich and invaluable journey through MIT. First and foremost, I would like to thank my advisor, Dr. James D. Paduano, who has superbly (and patiently) supervised this thesis. He continually provided insightful advice and much-needed encouragement. Working with Dr. Paduano has been a great pleasure and a rewarding experience. To him I give my respect and gratitude.

I am also very thankful to my committee members for their constructive critique of this thesis throughout its evolution. In particular, I extend my thanks to Professor Kamal Youcef-Toumi for his encouragement and his advice on modeling and dynamics; Dr. Fredrich Ehrich for his invaluable input on rotordynamics and fluid-induced forces; and Professor Samir Nayfeh for lending me not only his expertise in nonlinear dynamics, but also his immeasurable help, compassionate support and precious friendship throughout my stay at MIT.

I have been very fortunate to receive outstanding guidance and support from several people, among them, Professor Alan Epstein whose support extended well beyond giving me the opportunity to work in the Gas Turbine Lab and supervising my Master's thesis; Professor Edward Greitzer for many useful discussions and for instilling in me a more universal standard for excellence; Professor Ali Nayfeh, at Virginia Tech, whom I am honored to have met and known, albeit briefly; Professors Frank Marble (Caltech) and Nicholas Cumpsty (Cambridge University) for their valuable input during their visits to MIT; and Dr. Choon Tan for several useful discussions and suggestions.

The help of the staff at the Gas Turbine Lab, especially Steve Lukachko, Lori Martinez, and Diana Park, is much appreciated. I have also been fortunate to have known and interacted with many current, former, and visiting students at the Gas Turbine Lab, from whom I learned a great deal about turbomachinery, engineering, and world cultures. Among them are Dr. Martin Graf, Zoltan Spakovszky, Dr. Ken Gordon, Dr. Luc Fréchette, Eric Nelson, Huu Duc Vo, and Dr. Yong Wang (Caltech). I would also like to thank my current officemates, Taek Choi, Simon Evans, and Zack Warfield, for being very supportive, especially during the final stages of this work.

This work has been made possible by the sponsorship of the Saudi Arabian Oil Company (Saudi ARAMCO). I am indebted to the management and staff of Abqaiq Plants for giving me the opportunity to pursue my graduate education, and for providing the necessary funds. The encouragement and support of the following people are especially appreciated: Mr. Abdullah M. Al-Ghamdi, Manager of Abqaiq Plants Operations Department; Dr. Mohammed Samaha, General Supervisor of Abqaiq Plants Operations Engineering Division; Mr. Suhail S. Al-Husseini, Superintendent of the Utilities Maintenance Division and my first ARAMCO mentor at Abqaiq Plants Vibrations Group; and Mr. Esteban (Steve) C. Perez, Senior Rotating Equipment Engineer at Abqaiq Plants Engineering Division. In addition, the staff at the company's office in Houston (ARAMCO Services Company) in general, and Mr. Brad Brumfield in particular, have provided constant encouragement and excellent administrative support throughout this assignment.

To my friends and family

I am thankful for the many friendships I have with an outstanding group of people, from whom I learned something about everything, and to whom I will remain deeply grateful. Among the MIT crowd are: Ahmed Ait-Ghezala, Kareem Akhtar, Abdulfattah Al-Dajani, Abdulaziz Al-Jalal, Basel Al-Naffouri, Tareq Al-Nuaim, Tarik Alatovic, Wissam Ali-Ahmad, Omar Baba, Dr. Bashir Dabbousi, Yassir Elley, Waleed Farahat, Seif-Eddeen Fateen, Aykut Firat, Isam Habboush, Belal Helal, Dr. Husni Idris, M. Bilal Kaleem, Dr. M. Mustapha Khemira, Suheil Laher, Ali Lejlic, Dr. Yehia Massoud, Dr. Ali Merchant, Hasan Nayfeh, Dr. Sabbir Rahman, Farhan Rana, Mohammad Saeed, Numan Waheed, Ahmed Yahia, Namik Yilmaz, and all past and present members of the Muslim community at MIT and the Boston area.

In addition, special thanks are due to Fouzi Al-Essa, Dr. Asif Khalak and Ayman Shabra for their constant encouragement, moral support and everlasting friendship. Special thanks are also due to Mohammad Ali for his moral guidance, invaluable help and precious friendship; Babak Ayazifar for keeping my Arabic language skills (relatively) sharp and for many enlightening discussions; Osamah El Rifai whose outstanding mastery of control theory and vast engineering knowledge have tremendously helped me in preparing for the PhD qualifying exams, as well as for several classes; Kashif Khan for his immense help in countless matters, and for providing instant encyclopaedic answers to dozens of my queries, ranging from the dark mysteries of Jupiter's moons to the historical origin of *biryani* rice; M. Jalal Khan for his precious and compassionate friendship, and for mixing our "brief" and "early" morning sessions of coffee and bagels with a healthy dose of intellectual contemplation, musings, and complaining; and Gassan Al-Kibsi for constantly pointing out the high opportunity cost of our "brief" morning sessions. I am also indebted to my cousin Asaad Al-Asaad and his family for their help and support, and for their much-appreciated company throughout our stay in Boston. I would also like to thank all those who participated in our weekly soccer games, my only means of staying (almost) in shape.

Furthermore, I would like to thank my friends outside MIT whose constant support and encouragement reached me from the farthest corners of the world. Among them are Ammar Abuthurayah, Raad Al-Ali, Dr. Nidal Al-Hanbali, Majed Al-Jeraisy, Ayad Al-Rukbi, Dr. Ahmad El Rifai, Dr. Zuhdi Nagshabandi, and Bader Salmeen. The friendship of Dr. Mohammed Al-Majed during our years at King Saud University, and during and after his years at UC Berkeley will always have a special place in my heart. My gratitude also goes to my previous instructors at King Saud University, whose early tutelage and encouragement have helped me reach this point. In particular I am grateful to Professors Mohamed ElMadany, Khalil Abu-Abdou, Zuhair Abduljabbar, Hasan Homaideh, Sami Tumer and Samim Unlusoy.

Above all, my heartfelt gratitude and appreciation goes to my original and most gracious teachers, my parents Adnan and Aminah, whom I credit, after *Allah*, with all that's good in my life; to my dear brother Bilal for his infinite kindness and compassionate support; to his wife and dear children Razan, Juman and Adnan Jr.; to my dear sister Arwa, her husband Abdelmuti Al-Johary and their five precious children Lubna, Leenah, Lamees, Hazem and Ghadah, for all their love and support; to the memory of my late brother Eyad who greatly shaped my life during his presence and by his early departure; to my youngest brother Muhammad for his exemplary sacrifice and patience during several tough years of being far apart; to my respected parents-in-law, Khalid and Iffat, for their infinite giving, constant love and encouragement, and gracious support; and to my brothers-in-law, Hassan, Ibrahim and Hamza, for staying in touch throughout these years.

Finally, to my beloved wife Nada who had to shoulder a huge burden, and sacrifice and endure tremendously during this long journey; and to my three precious little ones, my son Majed and my daughters Ayah and Nuha, all of whom are my pride and joy, this thesis I dedicate to you.

All praise belongs to Allah, the Lord of the Worlds.

CONTENTS

List of Figures

List of Tables

NOMENCLATURE

$\mathcal{A}$	Area
$A, (A_n)$	Amplitude of the first (n^{th}) harmonic of flow nonuniformity
$a, b, (a_n, b_n)$	Cartesian components of the first (n^{th}) harmonic of flow nonuniformity
$(AR)_r, (AR)_{br}$	Aspect ratio of rotor blade (h/l), rotor blade row $\left(l_Z/R = \frac{\lambda \cos^2 \gamma_r}{N_{st}}\right)$
B	B-parameter, Eq. (2.24)
c	Rotordynamic damping coefficient
e	Eccentricity of rotor's center of mass (from axis of rotation)
$F, \bar{f}$	Force, amplitude of harmonaic forcing
$(F)_i$	Per-stage, nondimensional aerodynamic force
G, g	Nondimensional, dimensional gravitational acceleration
H, W	Parameters of the compressor pressure-rise characteristic
h	Blade radial span (height)
$\mathbf{i}, \mathbf{j}, \mathbf{k}$	Unit vectors
k	Rotordynamic stiffness constant
$L_I, L_E, \mathcal{L}$	Inlet, exit and total effective duct length
l, l_Z	Blade chord, blade axial chord
M, M_{st}	Mass of rotating assembly, mass of one stage of rotating assembly
m	Exit duct approximation parameter, Eq. (2.18)
N, N_{st}	Number of terms in Fourier series, number of compressor stages
P	Rescaled pressure-rise coefficient, $P = \Psi/H$
p, p_t	Static, total pressure
Q, q	Rescaled flow coefficient, $Q = \Phi/W$, $q = \phi/W$
R, r	Mean annular radius, rotor radial displacement
S	Aspect ratio of the compressor pressure-rise characteristic
s	Eigenvalue
t	Dimensional time

U	Mean rotor speed
$\mathcal{V}, v$	Volume, flowfield velocity
X, Y	Cartesian rotor displacements in the inertial frame
XYZ	Inertial frame of reference
xyz	Translating frame of reference (fixed to the rotor center)
$x'y'z'$	Rotating and translating frame of reference (fixed to the rotor disk)
X^*Y^*	Rotating (whirling) frame of reference (fixed to the tip-clearance asymmetry)

Greek

$\alpha, \bar{\alpha}$	Absolute flow angle, blade (metal) angle
$\beta, \bar{\beta}$	Relative flow angle, blade (metal) angle
β^{Al}	The Alford β parameter, Eq. (3.22)
γ	Nondimensional throttle coefficient
γ_r, γ_s	Rotor, stator blade stagger angle
ε	Tip clearance
ζ	Damping coefficient
$\eta, (\eta_n)$	Phase angle of the first (n^{th}) harmonic of flowfield nonuniformity
Θ, θ	Angular (whirl) displacement of rotor center, circumferential coordinate
λ, μ	Inertia parameter of rotor blade rows, all compressor blade rows
ν	Rotor natural Frequency, fraction of Ω, ($\nu = \omega/\Omega$)
$\nu^{He}, \nu^{rs}, \nu^{wh}$	Helmoholtz, rotating stall, and whirl frequency, all fraction of Ω
ξ	Nondimensional time
ϖ	Nondimensional coefficient of nonlinear rotor stiffness
ρ	Density
σ	Detuning parameter
$\tau_c, (\tau_c)_i$	Total, per-stage compressor torque
$\tau_{c0}, \tau_{c1}, \ldots$	Coefficients of compressor torque characteristic
Φ, ϕ	Annulus-averaged, total axial compressor flow coefficient
ϕ_θ	Circumferential compressor flow coefficient
φ	Flow potential
χ	Aerodynamic-rotordynamic coupling parameter
Ψ	Total-to-static system pressure rise coefficient
ψ_c^{ss}, ψ_c	Static-to-static, total-to-static compressor pressure-rise characteristic
$\bar{\psi}_c^C, \bar{\psi}_c^{Cc}, \bar{\psi}_c^{Cs}$	Cartesian form of averaged, cosine and sine moments of ψ_c

$\bar{\psi}_c^p, \bar{\psi}_c^{pc}, \bar{\psi}_c^{ps}$	Polar form of averaged, cosine and sine moments of ψ_c
ψ_{c0}	Shut-off value of ψ_c. (Note that $\psi_{c0}H$ is the shut-off value of ψ_c')
$\psi_{c\varepsilon}$	Sensitivity of compressor pressure-rise characteristic to tip-clearance, $\psi_{c\varepsilon} = -\frac{\partial \psi_c}{\partial \varepsilon}$
Ω, ω	Rotor rotational (spin) frequency ($\Omega = U/R$), rotor natural frequency ($\omega = \sqrt{k/M}$)

Superscripts, Subscripts and Other Operators

X^{in}, X^{out}	Value at inlet, exit plane of blade row
X^{tu}, X^{pr}, X^{un}	Quantities related to turning, pressure, and unsteady force contributions
X^{da}, X^{st}, X^{ns}	Quantities related to damping, linear stiffness, and nonlinear stiffness forces
X^{gr}, X^{ha}	Quantities related to gravity, harmonic excitation forces
X^{rs}	Quantity related to rotating stall
$X_{A,I,E,P,T}$	Referrence to locations $A, I, \ldots$ along the compression system, Figure 2-1
$X_{r(i)}, X_{s(i-1)}, \ldots$	Reference to the i^{th} rotor blade row, the $(i-1)^{\text{th}}$ stator blade row, ...
$X_Z, X_{y'}, X_\Theta, \ldots$	Components along the direction of Z, y', Θ, ...
X_e	Quantity at equilibrium (fixed) point
$\mathbb{X}, \mathbf{x}$	Matrix, vector
$\dot{X}$	Derivative of X with respect to time (t and ξ for dimensional and nondimensional quantities respectively)
$\bar{(\cdot)}$	Averaged quantity
$(\cdot)'$	A quantity for which a rescaled version with no prime exists, Eq. (2.95)
$\delta(\cdot)$	Disturbance or nonuniform component
$\tilde{(\cdot)}$	Dimensional quantity for which a nondimensional counterpart exists
$(\cdot)^*$	Quantity measured in tip-clearance asymmetry frame

CHAPTER 1

INTRODUCTION

1.1 Background and Motivation

The design and operation of axial turbomachines are plagued by different types of aerodynamic and structural instabilities such as surge, rotating stall and shaft whirl. These instabilities may subject the machine to forces and stresses beyond what the components are designed for. In addition to the possibility of costly and catastrophic mechanical failure of these components, the mere interruption of operation may be at least as catastrophic (e.g., aircraft jet engines) or as costly (e.g., gas and oil production plants).

Many advances in understanding and dealing with these phenomena have taken place over the past few decades. Nevertheless, more demanding operational and economic requirements are still posing significant challenges in this field. This study addresses one such challenge; namely, the interaction of rotordynamics and aerodynamics in axial compression systems.

The aerodynamic performance and flowfield stability of axial turbomachines are known to strongly depend on the clearance gap between the tips of the rotating blades and the stationary casing. Across this gap, known as the tip clearance, a leakage flow that traverses the main blade-passage flow is established as a result of the pressure difference between the two sides of each blade. The mixing of the two flow streams

and the growth of the resulting tip vortex as it convects downstream are among the main sources of viscous losses in axial turbomachines. In an axial compressor, for instance, these losses are manifested as a reduction in both pressure rise capability and efficiency, as well as an increase in the stalling mass flow rate (i.e., loss of stability). In general, larger tip clearances correspond to higher losses. Further, change in the mean tip clearance, as well as its circumferential variation, may impact both performance and stability. Such considerations have been the subject of several studies concerned with the flowfield stability of compression systems [31, 56, 57, 34, 44, 30, 28].

Tip clearance may change either permanently (e.g., due to rotor rubs against the casing), or dynamically as the rotor moves within the casing or as the casing deforms in shape. The motion of the rotor is governed by the structural dynamics of the rotor-bearings subsystem (the study if which is known as rotordynamics) and by the aerodynamic forces acting on the rotor blades and hub. Under certain conditions, these forces can be of such magnitude and direction that they cause the rotor center to follow a fixed orbit, possibly of large amplitude—a self-excited instability known as rotor whirl. Such rotordynamic behavior under the influence of these forces is an important consideration in the design and operation of rotating machinery. Together with several other rotordynamic phenomena (e.g., response to imbalance and oil whip in journal bearings), rotor whirl has long been recognized and addressed in the discipline of rotordynamics as an undesirable structural response of potentially severe consequences [75, 3, 79, 7, 19, 6, 49, 71, 69, 73, 22, 2, 74].

These issues are further complicated by the fact that the dynamic behavior of the flowfield and the rotordynamics in axial compression systems may be strongly coupled. The coupling is established through the dependence of the rotordynamics on the aerodynamic forces described above, and through the dependence of the flowfield on the tip clearance. In other words, as a result of the rotor motion and the associated changes in tip clearance distribution, the flowfield—and hence the aerodynamic forces on the rotor—vary such that they influence subsequent rotor motion and flowfield adjustments, see Figure 1.1.

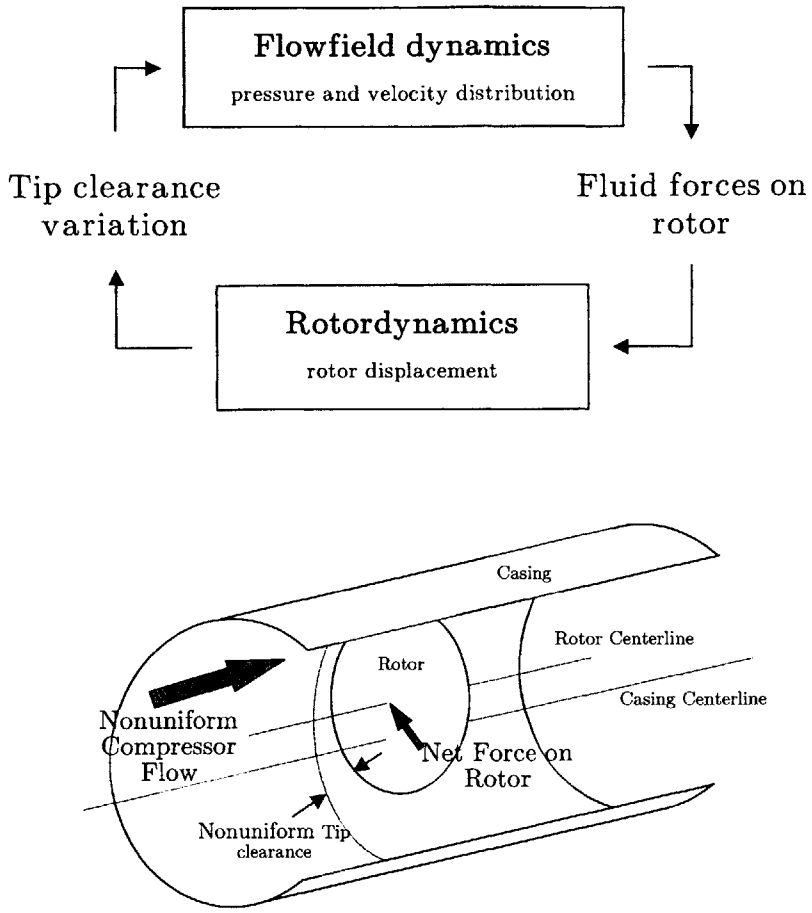

Figure 1-1: Aerodynamic-rotordynamic coupling mechanism.

There is evidence, both experimental (e.g. Weigl [81]), and theoretical (e,g., Gordan [28]), that this interaction is significant in that, under certain conditions, the rotordynamic behavior may potentially alter (either favorably or adversely) the aerodynamic stability, or vice versa. Ultimately, the understanding of such interaction and its implications should open the door for new design and control concepts which yield more reliable and stable machines. Specific examples are given below in Section 1.2.

Given the fact that the performance and stability of axial compression systems are very sensitive to tip clearance variation and distribution—which is directly influenced by movement of the rotor—and that the rotordynamic stability may also depend on

the forces generated by the flowfield, it becomes of interest to understand the overall dynamic picture of the coupled system, where all these subsystems are interacting together. It is the mission of this thesis to take the first steps towards establishing this understanding.

1.2 Previous Work

This thesis builds on a large body of available research in the different disciplines that it brings together; namely, aerodynamic stability of axial compression systems and tip clearance effects on the one hand, and rotordynamics on the other. The following is a brief survey of relevant previous work.

1.2.1 Aerodynamic Stability of Axial Compression Systems

General Stability

The early theoretical and experimental work of Emmons et al. [23] established some of the fundamental concepts needed to examine and understand surge and rotating stall. Greitzer [31] utilized these concepts to construct a lumped parameter, nonlinear surge model. His experiments and numerical simulations showed the importance of system parameters in determining the existence and type of instability. The next main step in this field was due to Moore [56] and Moore and Greitzer [57, 34]. These works provided a class of models that capture the dynamics of both axisymmetric, surge-like and nonaxisymmetric, stall-like disturbances under uniform inlet flow conditions. Hynes and Greitzer [44], and more recently Longley et al. [52], extended this approach to account for the effects of stationary and rotating inlet distortions respectively.

Tip clearance Effects

The early work by Smith [67] addressed the effect of tip clearance on axial compressor performance and provided a compilation of several experimental data correlating compressor pressure rise to tip clearance. Another compilation of such data was given more recently by Baghdadi [4]. Storer and Cumpsty [45] proposed a simple model to predict losses due to the tip clearance leakage flow in an axial compressor. Horlock and Greitzer [42] developed a linearized steady analysis based on actuator-disc theory to predict the distorted flowfield produced by a tip clearance asymmetry.

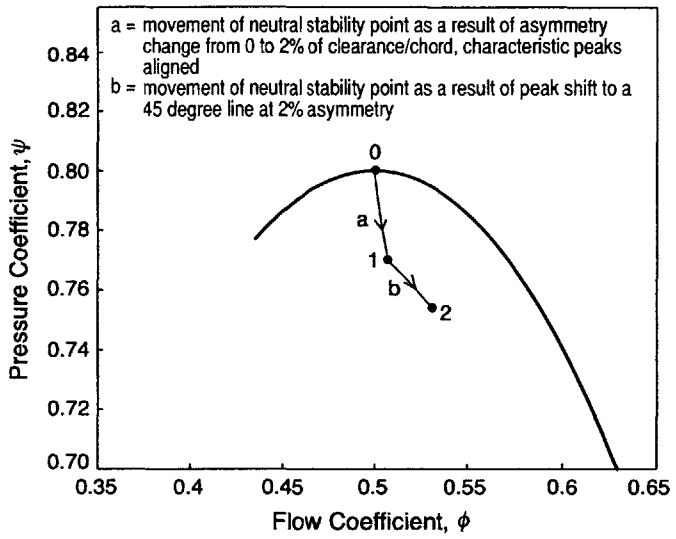

Figure 1-2: Effect of stationary tip clearance asymmetry on compressor stability, from Graf et al. [30].

The effect of tip clearance on aerodynamic stability of axial compression systems was addressed by Graf [29] and Graf et al. [30] who used a modified version of the Hynes-Greitzer [44] model to examine compression system stability, both theoretically and experimentally, under stationary tip clearance asymmetry (e.g., distorted casing). Figure 1-2 shows the locus of neutral stability points as the amplitude and wavelength of the asymmetry are varied. The study showed that the asymmetry has a destabilizing effect which is higher than that of a uniform clearance having the same mean. Gordon [28] generalized that treatment to include tip clearance asymmetries

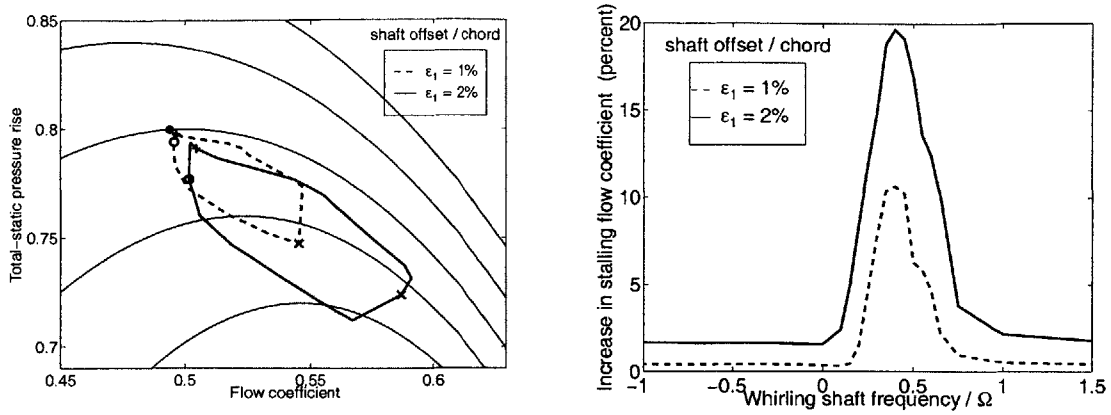

Locus of stall points on family of axisymmetric characteristics for rotor offset $= 0\%, \pm 1\%, \pm 2\%$ *chord (•, stall point for uniform flow;* ∘, $\nu^{wh} = 0$; ×, $\nu^{wh} = 0.35$; +, $\nu^{wh} = 1$*)*

Figure 1-3: Effect of forced rotor whirl on rotating stall inception, numerical results from Gordon [28]. (ν^{wh} is the rotor whirl frequency and ε_1 is the rotor offset.

that may be rotating at any frequency. He showed that the inception of instability is adversely affected as this frequency becomes closer to a critical value, which is in the neighborhood of the rotating stall first mode eigen-frequency. Figure 1-3 illustrates this effect as calculated for the MIT 3-stage axial compressor.

Control of Instabilities

Several experimental and theoretical works branched from the original Moore-Greitzer model, addressing various modifications and extensions. One such extension is of particular significance. The concept of active control of aerodynamic instabilities, first proposed by Epstein et al. [24], has evolved to be a major area of interest in research and industry. A review of active control concepts is given by Paduano et al. [65]. A relevant example from these active control efforts is the concurrent work by Spakovszky [72] in which a detailed experimental investigation of using magnetic bearings to stabilize rotating stall by means of actively moving the rotor and thus adjusting the tip clearance distribution is proposed and assessed.

Nonlinear Aspects

The nonlinear nature of the Moore-Greitzer type models together with the fact that fully developed surge and rotating stall are ultimately nonlinear, limit-cycle type instabilities, have attracted attention from the nonlinear dynamics community. Abed et al. [1] addressed the bifurcation behaviour of the simple, lumped parameter surge model. McCaughan [54] presented a detailed bifurcation analysis of the Moore-Greitzer third order model and outlined the post-instability behaviour—including both surge and rotating stall—of axial compression systems in the B–γ parameter space (B and γ are the ratio of system compliance to inertia and the throttle coefficient respectively). Finally, several investigations (e.g., Nayfeh [62] and Wang [80]) have been conducted to apply nonlinear control concepts to alter the undesirable post-instability behaviour of the system. This, in general, amounts to attempting to change the nature of the bifurcation from subcritical to supercritical. In order to achieve this, Wang [80] theoretically examined the nonlinear aspects of actively controlling surge and rotating stall by means of tip-clearance actuation through magnetic bearings.

1.2.2 Rotordynamic Stability

General

The Jeffcott rotor[1] [46] is essentially stable since it is a damped vibratory system consisting of a mass, springs and dampers. The potential for instability arises from the interaction between centrifugal forces due to whirl-like rotation, and several internal and external forces acting on the rotor. Examples of such forces include fluid forces (such as those generated from tip clearance asymmetry, labyrinth seals flow, and oil flow in journal bearings) and forces due to internal rotor damping. A physical and

[1]The Jeffcott rotor model is a dynamical representation of the rotor structure that consists of a spinning disc with a point mass supported by springs and impeded by viscous damping. Section 2.2 of this thesis presents a detailed description of this model.

concise description of such effects and how they lead to instability can be found in Den Hartog [16] and Crandall [8]. More recent presentation can be found in Ehrich [18] and Childs [6].

Source and Effect of Aerodynamic Forces Induced by Tip Clearance Asymmetry

As we mentioned earlier, the role of aerodynamic forces in producing rotordynamic whirl has long been recognized. In order to explain rotor whirl, Thomas [75] and Alford [3] were the first to suggest simple models to link the whirl-inducing tangential fluid force resulting from a tip clearance asymmetry produced by a displaced rotor. Such models are of a phenomenological nature in that they assume a linear proportionality between the tangential aerodynamic force, F_{Θ}^{ae}, on the rotor and the radial rotor offset, r, with the proportionality factor, q, being based on efficiency arguments [3, 18, 6], i.e., $F_{\Theta}^{ae} = qr$. It is argued that the factor q depends on another parameter which we label as β^{Al}, and which is defined as the change of the turbomachine's thermodynamic efficiency per unit rotor displacement. Alford also carried out a linear stability analysis of a Jeffcott type rotor and showed that the rotor loses stability in the presence of aerodynamic forces according to the simple condition $c > q/\omega$, where c is the damping coefficient and ω is the undamped natural frequency of the rotor structure. There is, however, a great deal of uncertainty involved in estimating β^{Al} and in determining its dependence on the turbomachine's geometry and flowfield conditions.

As an example of the destabilizing effect of these forces on the rotordynamic stability of an actual engine, Akin et al. [2] reported on aerodynamically-induced rotor instability in the TF30 P111 engine. The authors accounted for different sources of destabilizing forces and concluded that, in that case, the Alford-type forces generated on the turbine side of the engine were responsible for the instability. Incorporating an oil-film damper at the bearing was proposed, analyzed and implemented, and was shown to eliminate the problem. The authors concluded, however, that the general

determination of the source of instability is difficult and requires careful testing and analysis.

Measurement and Prediction of Aerodynamic Forces

Following Thomas and Alford's work, there has been a substantial amount of work dedicated to understanding aerodynamic forces in turbomachines. On the turbine side, Song et al. [70] developed and experimentally verified a first-principles based model to predict these forces in an axial turbine. In order to estimate these forces in an axial compressor, Colding-Jorgenson [7] adopted the actuator-disc based model of Horlock and Greitzer [42], whereas Ehrich [19] used a parallel compressor model together with experimental flowfield measurements at different clearance settings.

Very recently there has been a comprehensive study of aerodynamic forces that specifically addresses axial compressors. In a two-part paper by Storace et al. [73] and Ehrich et al. [22], an experimental and analytical effort is reported in which an offset rotor in a low speed four stage research compressor is considered. Detailed measurements of pressure distribution on the two sides of an airfoil as it travels through regions of different tip clearance were recorded and used to calculate the force on that blade. The net force on the rotor was then deduced. In a related work by Spakovszky [71] (also partly reported in Ehrich et al. [22]) aerodynamic forces are calculated by implementing a blade-passage control volume analysis for which flowfield information is obtained from a separate calculation based on a Moore-Greitzer type model. Song et al. [69] also presented an analytical calculation of these forces along the same lines of his earlier work on turbines [70]. Examples of these results are presented and compared to the results of this thesis in Chapter 3.

These efforts have established a foundation for understanding the nature of aerodynamic forces, and produced a database of measurements against which analytical calculations can be compared. Nevertheless, these efforts are limited in one or more of the following ways:

- The configurations considered are usually static or steady in some sense (i.e., either the rotor is fixed or the flowfield dynamics are excluded). The dynamic nature of the problem which ultimately decides the presence and direction of whirl is not addressed, and sometimes is overlooked when making qualitative predictions about stability.
- Except for Spakovszky [71] and Song [69], the force is generally linked directly to the tip clearance distribution, ignoring the fact that the flowfield velocity and pressure nonuniformity—which is the true source of the force—may be considerably out of phase with the geometric tip clearance distribution. The result is a possibly incorrect intuition about the direction of the net force.
- The force contribution due to the hydrostatic pressure nonuniformity is usually not accounted for in the rotordynamic stability analysis, and has been overlooked in most previous treatments.
- Most of these efforts are either specific to one configuration or compression system, restricted to a small range of operating conditions, or are computationally intensive. The result is an inability to extract general trends, to establish dependency on parameters, or to build an overall system dynamic model of a manageable complexity.

1.2.3 Aerodynamic-Rotordyanmic Coupling

In the course of active control experiments of rotating stall, Weigl [81] reported on potential coupling between the rotordynamic and aerodynamic domains when he observed that the frequency of rotor whirl (due to a deteriorating journal bearing) and that of rotating stall coincided when they were simultaneously present. He also observed that the first mode of circumferential flow disturbances had a much higher energy content prior to the onset of instability, as compared to runs with the healthy bearing, Figure 1-4.

Another indication of possible coupling comes from a recent problem observed

during the testing of a new engine which is still in the developmental stage, Ehrich [21]. The problem included the loss of aerodynamic stability (surge event) at the design point in the presence of a rotordynamic, subsyncronous, whirl-like behaviour which has been identified as a subharmonic, nonlinear response to imbalance.

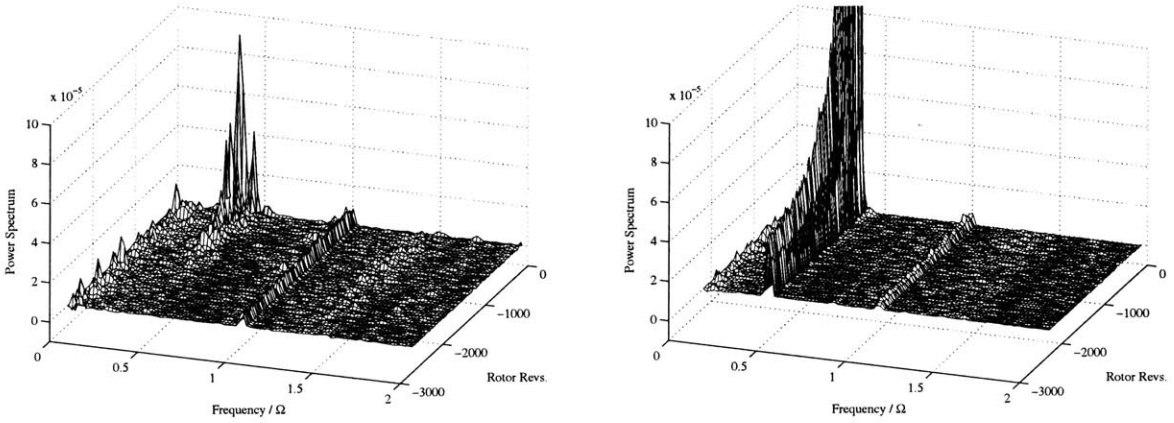

Figure 1-4: Effect of rotor whirl on rotating stall inception, data from Weigl [81].

The above overview of previous research establishes strong links between *some* aspects of axial compressor aerodynamics and rotordynamics in that it sheds light on several ways in which one of the two domains can impact the other. Having said that, and realizing that these two dynamic systems (fluid and structural) are in fact coupled and interacting, the next logical step is to understand this coupling and assess its significance.

1.3 Research Objectives

The mission of this thesis is to present the first integrated treatment of aerodynamic-rotordynamic coupling in axial compression systems. This treatment is aimed at developing a better understanding of phenomena that have not been explored before and that may directly contribute to the design and operation of more stable and reliable compression systems.

To that end, the following research objectives have been identified:

- Extend the current understanding of the nature of aerodynamic forces generated by asymmetric tip-clearance in axial compressors. In particular, establish simple, first-principles based relations, between these forces and a given flow nonuniformity, that accounts for all force contributions and that is valid over a wide range of compressor operating conditions.
- Determine the set of nondimensional parameters governing the coupling of aerodynamics and rotordynamics in an axial compression system, and relate these parameters, and how they scale, to a physical description of the mechanisms at work.
- In terms of these parameters, determine the conditions under which aerodynamic-rotordynamic coupling is important.
- Predict the potential impact of this coupling on the stability of the flowfield and rotor structure. In particular, determine physical arguments and relative design parameter values that are potentially: i) dangerous or destabilizing, and/or ii) beneficial to overall stability.

1.4 Approach and Scope

In order to achieve the above objectives, the following approach is adopted:

Modeling of the coupled System: This involves developing and integrating the following sub-models

- *A fluid dynamic model of the flowfield:* A Moore-Greitzer type model is adopted, with modifications to account for tip clearance variation. Such models have been used extensively by many researchers and have been proven to capture the main aspects of the physics relevant to the study of flowfield stability. In addition, the assumptions and limitations of such models are recognized and understood. Once the model is formulated, a Galerkin procedure is implemented to transform the partial differential equations into a compact set of ordinary

differential equations that are more amenable to analytical work and reliable numerical simulations. In that procedure, a truncated Fourier series is used as the basis function to simplify the periodic circumferential dependence.

- *A rotordynamic model of the structural dynamics:* A simple, Jeffcott-rotor type (mass-spring-damper) model is utilized for the purposes of the "baseline" model. Despite its simplicity, this model is frequently used within the rotordynamic community to demonstrate basic features of the rotor structural response. The limitations of this class of models are also well-understood and can be accounted for.

- *A model of tip clearance effects on compressor performance:* This is the first coupling channel between the two domains. To capture this effect in the current study, the compressor pressure rise characteristic function may be modified with additional term(s) to account for the local loss in pressure rise at locations of large clearances. This is motivated by the desire to avoid modeling the complex details of the tip leakage flow, and is supported by several compilations of experimental data (e.g., Smith [67] and Baghdadi [4]) for different compressors. The same approach has been used by Graf [29] and Gordan [28] in the context of compression system stability

- *A model of the aerodynamic forces on the compressor rotor:* This is the second coupling channel between the two domains. Unlike the first three sub-models, which are readily available for incorporation into this study with only minor modifications, the force model requires special attention and a different approach. As discussed in Section 1.2, the work previously done on aerodynamic forces acting on compressor rotors has so far been inconclusive as to when and how these forces can lead to rotor whirl instability. In addition, it has not provided a general and simple characterization of how these forces depend on both flowfield nonuniformity and system parameters. In the context of aerodynamic-rotordynamic interaction, in which these forces play a dominant coupling role, it is essential to correctly include all the forces on the rotor in the overall dynamic

model. Therefore, a first-principles, control volume approach is adopted in this study. The unsteady momentum balance on this system gives an estimate of the magnitude and direction of the total force on the rotor as a function of flowfield quantities that are available from the reduced-order fluid dynamic model described above. The combined sub-models provide a compact means of simultaneously calculating the flowfield quantities and the aerodynamic forces in one unified model, allowing the dynamics of the overall system to be explored. As a by-product of this modeling approach, a generalized characterization of the nature of these forces may be explored in terms of their dependency on system parameters, such as the compressor characteristics, and flowfield pressure and velocity nonuniformities, which in turn depend on tip clearance.

Analysis of the resulting models: To achieve the objectives of this research, a variety of analytical and numerical tools are applied to the resulting models.

- The features of the overall system equations are examined to determine their numerical structure, physical scaling and other dynamic properties based on the governing nondimensional parameters and general coupling trends.
- Several analytical methods are used to examine the stability of the overall system and the impact of any possible interaction on both aerodynamic and structural domains. Analytical methods to be applied include linear stability analysis, examination of fixed points, and calculation of bifurcations and limit cycles. Direct numerical simulations will be utilized to demonstrate and verify interesting dynamic trends.
- Comparison with simpler, uncoupled models (e.g., the Moore-Greitzer compressor model) is used for assessing the predictive capabilities of this approach in determining the significance of the interaction.

Model Validation. With the exception of the sub-model describing the aerodynamic forces on the rotor, all other sub-models considered in this study have been examined

and utilized both analytically and experimentally by many authors in the literature. Therefore, given the objectives and scope of this study these sub-models are deemed suitable and reliable based on the existing understanding of their assumptions and limitations.

The aerodynamic force sub-model, on the other hand, represents one of the contributions of this research, and will therefore be validated against the recently published data by Storace et al. [73] and the accompanying analysis by Ehrich et al. [22], and presented in Chapter 3.

1.5 Thesis Organization

This thesis is organized as follows. In Chapter 2 we present a generalized development of the aerodynamic-rotordynamic interaction model. We then implement several approximations and assumptions to produce the baseline model upon which the the analysis for the rest of this thesis is based. In Chapter 3 we explore the general features of the interaction phenomena by considering several special, simple cases through which insight may be gained. In particular we investigate the nature of the aerodynamic forces under steady rotor offset and forced rotor whirl at different compressor operating points. Chapter 4 presents the linear stability analysis through which we quantify the impact of coupling on the inception of aerodynamic and rotordynamic instabilities. The post-instability behavior is addressed in Chapter 5 where standard numerical tools are utilized to solve for possible limit-cycles and identify potential coupling effects on the nature of the nonlinear behavior. We finally summarize the findings of this study, discuss their implications on compression system design and operation, and lay out recommendations for future work in Chapter 6.

CHAPTER 2

DEVELOPMENT OF AERODYNAMIC-ROTORDYNAMIC INTERACTION MODEL

In this chapter a generalized model describing the aerodynamic-rotordynamic interaction is developed. Equations describing the flowfield, the rotating structure and their interaction are derived and the underlying assumptions are outlined. Next, several approximations and simplifications are applied to the generalized model yielding a simpler, low-order baseline model which forms the basis for most of the subsequent analysis. Finally, the main nondimensional parameters governing this baseline model are noted and defined.

2.1 Flowfield Description

We consider a high hub-to-tip ratio, low speed axial compression system in which the flowfield may be assumed incompressible and two dimensional. Such a compression system may be adequately described by a slightly modified version of the original Moore-Greitzer model [57] which has been extensively utilized in numerous studies concerned with axial compression systems stability. The main modification in this development (as well as in that of Graf [29], Gordon [28], and Spakovszky [71]) is allowing the pressure-rise characteristic of the compressor to depend on the local tip

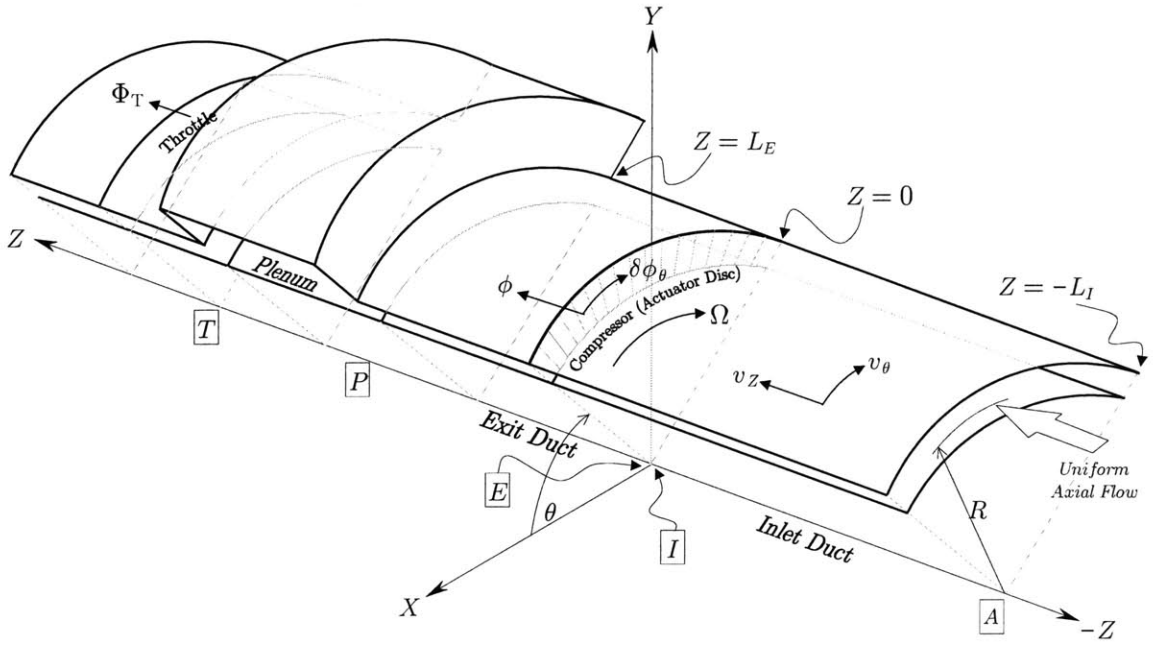

Figure 2-1: Schematic of the compression system model.

clearance.

In what follows we present a summary of the Moore-Greitzer model. Further details can be found in several references (see for example Moore and Greitzer [57] and Longley [51]).

2.1.1 Derivation of the Basic Equations

Flowfield Quantities

Figure 2-1 depicts an axial slice of the compression system being considered, showing the stationary coordinate system XYZ as well as the system's main components, parameters and flowfield quantities. The axial stations A, I, E, P and T refer to the atmosphere, compressor inlet, compressor exit, plenum, and throttle respectively. In this two-dimensional model, where all radial variations are neglected, the flow

is described by the nondimensional[1] velocity field $(v_Z(\theta, Z, \xi), v_\theta(\theta, Z, \xi))$, and the nondimensional pressure distribution $p(\theta, Z, \xi)/(\rho U^2)$. In general, these quantities are nondimensionalized as follows

Velocity:	$v = \tilde{v}/U = \tilde{v}/(R\Omega)$
Pressure:	$p/(\rho U^2) = p/(\rho(R\Omega)^2)$
Lengths:	For large, system-scale dimensions: $Z = \tilde{Z}/R$, $L_I = \tilde{L}_I/R$, $\mathcal{L} = \tilde{\mathcal{L}}/R, \ldots$ and so on. For small, blade-scale dimensions: $r = \tilde{r}/l$, $\varepsilon = \tilde{\varepsilon}/l, \ldots$, and so on, where l is the blade chord.
Time:	$\xi = t\Omega = tU/R$

At the compressor inlet, point I, it is customary to use $\phi(\theta, \xi) = v_Z(\theta, 0, \xi)$ to indicate the axial flow velocity into and throughout the compressor, also known as the flow coefficient. Further, ϕ can be split into two parts

$$\phi(\theta, \xi) = \Phi(\xi) + \delta\phi(\theta, \xi) \tag{2.1}$$

where $\Phi(\xi)$ is the annulus-averaged, axisymmetric axial flow coefficient and $\delta\phi(\theta, \xi)$ is the circumferentially varying (not necessarily small) disturbance representing the angle-dependent flow nonuniformity. These definitions can also be stated as

$$\frac{1}{2\pi}\int_0^{2\pi} \phi(\theta, \xi)\, d\theta = \Phi(\xi) \qquad \text{and} \qquad \frac{1}{2\pi}\int_0^{2\pi} \delta\phi(\theta, \xi)\, d\theta = 0 \tag{2.2}$$

We also note that, even in the case of uniform axial flow at the inlet (i.e. $v_\theta(\theta, Z = -L_I, \xi) = 0$ and $v_Z(Z = -L_I) =$ constant with θ), the presence of a nonzero $\delta\phi$ at the compressor inlet, point I, mandates the existence of a nonzero circumferential

[1]Dimensional quantities that share the same symbol with their nondimensional counterpart are distinguished by a tilde. For example, $\tilde{v}$ and v are the dimensional and nondimensional flow velocities respectively.

component $\delta\phi_\theta \triangleq v_\theta(\theta, Z=0, \xi)$ such that

$$\frac{1}{2\pi}\int_0^{2\pi} \delta\phi_\theta(\theta,\xi)\, d\theta = 0 \tag{2.3}$$

where the subscript θ indicates circumferential flow, rather that differentiation.

Compressor Inlet Duct

The flow in the compressor inlet duct is assumed to be unsteady, incompressible, inviscid, two-dimensional (in θ and Z) and irrotational. Thus, a flow potential function, $\varphi(\theta, Z, \xi)$, which satisfies Laplace's equation exists in the inlet duct and is related to the flow coefficient ϕ according to

$$v_Z = \frac{\partial\varphi}{\partial Z} \qquad \text{and} \qquad v_\theta = \frac{\partial\varphi}{\partial\theta} \tag{2.4}$$

Therefore, the axial flow coefficient at the compressor inlet, point I, may be written in terms of φ as

$$\phi(\theta,\xi) = \left.\frac{\partial\varphi}{\partial Z}\right|_I = \Phi(\xi) + \left.\frac{\partial\,\delta\varphi}{\partial Z}\right|_I \tag{2.5}$$

Integrating the above equation between point A and any point along the Z-axis within the constant-area inlet duct, and invoking the boundary condition at A, namely that $\varphi(\theta, -L_I, \xi) = 0$, we obtain

$$\varphi(\theta, Z, \xi) = (Z + L_I)\Phi(\xi) + \delta\varphi(\theta, Z, \xi) \tag{2.6}$$

We take this one step further by differentiating both sides with respect to ξ and setting $Z = 0$

$$\left.\frac{\partial\varphi}{\partial\xi}\right|_I = L_I\frac{d\Phi}{d\xi} + \left.\frac{\partial\delta\varphi}{\partial\xi}\right|_I \tag{2.7}$$

Now, the momentum balance in the inlet duct is obtained by applying the un-

steady Bernoulli's equation between points A and I

$$\frac{p_{tA}}{\rho U^2} + \left.\frac{\partial \varphi}{\partial \xi}\right|_A = \frac{p_{tI}}{\rho U^2} + \left.\frac{\partial \varphi}{\partial \xi}\right|_I \tag{2.8}$$

Since $\frac{\partial \varphi}{\partial \xi} = 0$ at point A, the pressure difference across the inlet duct can be written as

$$\frac{p_{tA} - p_I}{\rho \Omega^2 R^2} = \frac{1}{2}\left(\phi^2 + (\delta\phi_\theta)^2\right) + \left.\frac{\partial \varphi}{\partial \xi}\right|_I \tag{2.9}$$

Finally, substituting Eq. (2.7) into Eq. (2.10) gives the required pressure balance across the inlet duct

$$\frac{p_{tA} - p_I}{\rho \Omega^2 R^2} = \frac{1}{2}\left(\phi^2 + (\delta\phi_\theta)^2\right) + L_I \frac{d\Phi}{d\xi} + \left.\frac{\partial \delta\varphi}{\partial \xi}\right|_I \tag{2.10}$$

The pressure difference across the inlet guide vanes (IGV's), point I to point 1 (where point 1 refers to the inlet plane of the first rotor blade row), can be expressed as

$$\frac{p_1 - p_I}{\rho \Omega^2 R^2} = \frac{1}{2} K_{IGV} (\delta\phi_\theta)^2 \tag{2.11}$$

We will later assume lossless IGV's for which $K_{IGV} = 1$. This assumption eliminates the presence of $\delta\phi_\theta$ from the final pressure balance equation.

Compressor local momentum balance

Consistent with the actuator disc model of the axial compressor, the pressure rise across the compressor includes a steady state, axisymmetric contribution as well as an unsteady contribution due to fluid inertia within the rotor and stator rows. This is expressed as follows

$$\frac{p_E - p_1}{\rho \Omega^2 R^2} = \psi_c^{ss}(\phi, \varepsilon) - \lambda \frac{\partial \phi}{\partial \theta} - \mu \frac{\partial \phi}{\partial \xi} \tag{2.12}$$

where,

$$\lambda = \sum_{\substack{\text{rotors} \\ \text{only}}} \frac{l}{R\cos\gamma_r} \qquad \text{and} \qquad \mu = \sum_{\substack{\text{all} \\ \text{rows}}} \frac{l}{R\cos\gamma_r} \tag{2.13}$$

where l is the blade chord and γ_r is the stagger angle of rotor blades. For similar rotor-stator pairs, i.e. N repeated stages, the λ and μ parameters may be approximated as

$$\lambda = \frac{N_{st} l}{R\cos\gamma_r} \qquad \text{and} \qquad \mu = \frac{(2N_{st}+1)l}{R\cos\gamma_r} \approx 2\lambda \tag{2.14}$$

where N_{st} is the total number of compressor stages. Note in Eq. (2.12) the explicit dependency of the compressor pressure-rise characteristic, ψ_c^{ss}, on the local tip clearance, $\varepsilon(\theta,\xi)$, which is nondimensionalized by the rotor blade chord, l. In the original Moore-Greitzer model, ψ_c^{ss} depended only on flow coefficient ϕ and was thus called the *axisymmetric* pressure-rise characteristics.

Compressor Exit Duct

Unlike the inlet duct, the flowfield in the exit duct is rotational and thus more complex. We therefore adopt the same simplifying assumption used by Moore [56], and Moore and Greitzer [57] as follows. The quantity $\mathcal{P}$, defined as the deviation of the duct pressure from the plenum pressure:

$$\mathcal{P} = \frac{p_P - p(\theta, Z, \xi)}{\rho\Omega^2 R^2} \tag{2.15}$$

is assumed to be small enough in the exit duct to satisfy Laplace's equation, $\nabla^2\mathcal{P} = 0$. Realizing that the axial flow nonuniformity is assumed to pass through the compressor unchanged (i.e., $\delta\phi|_E = \delta\phi|_I$), the axial momentum equation evaluated at the

compressor exit, point E, can then be written as follows

$$\left.\frac{\partial \mathcal{P}}{\partial Z}\right|_E = \frac{\partial}{\partial \xi}\left(\Phi + \delta\phi|_E\right) = \frac{\partial}{\partial \xi}\left(\Phi + \delta\phi|_I\right)$$
$$= \frac{d\Phi}{d\xi} + \frac{\partial}{\partial \xi}\left(\left.\frac{\partial \delta\varphi}{\partial Z}\right|_I\right) \tag{2.16}$$

This equation has the same form as that of $\frac{\partial \varphi}{\partial \xi}$ from Eq. (2.5). We thus can obtain a solution for $\mathcal{P}$ in the exit duct in terms of $\delta\varphi$ by taking into account the difference in Z direction which, unlike the inlet duct, increases away from the compressor. Recognizing that all disturbances must vanish at $Z = L_E$, we obtain

$$\mathcal{P} = (Z - L_E)\frac{d\Phi}{d\xi} - \frac{\partial \delta\varphi}{\partial \xi} \tag{2.17}$$

Finally, at $Z = 0$ this becomes

$$\begin{aligned} \mathcal{P}_E &= \frac{p_P(\xi) - p_E(\theta, \xi)}{\rho\Omega^2 R^2} \\ &= -L_E\frac{d\Phi}{d\xi} - (m-1)\left.\frac{\partial \delta\varphi}{\partial \xi}\right|_I \end{aligned} \tag{2.18}$$

where the parameter m is introduced as an approximation which depends on the degree of diffusion in the exit duct; for a sudden expansion immediately downstream of the compressor, we set $m = 1$ and the second term is effectively omitted, while for a constant area duct with no expansion, as is the case here, we set $m = 2$.

Overall Pressure Balance

The overall pressure balance across the compressor and inlet and exit ducts (from point A to point P) can now be expressed as follows

$$\begin{aligned} \Psi(\xi) &= \frac{p_P - p_{tA}}{\rho\Omega^2 R^2} \\ &= \frac{p_P - p_E}{\rho\Omega^2 R^2} + \frac{p_E - p_1}{\rho\Omega^2 R^2} + \frac{p_1 - p_I}{\rho\Omega^2 R^2} + \frac{p_I - p_{tA}}{\rho\Omega^2 R^2} \end{aligned} \tag{2.19}$$

Substituting for these pressure differences from the corresponding equations derived above and collecting terms, one finds

$$\Psi(\xi) = (\psi_c^{ss} - \frac{1}{2}\phi^2) - (L_I + \mu + L_E)\frac{d\Phi}{d\xi} - m\left.\frac{\partial\delta\varphi}{\partial\xi}\right|_I - \lambda\frac{\partial\delta\phi}{\partial\theta} - \mu\frac{\partial\delta\phi}{\partial\xi} - \frac{1}{2}(1 - K_{IGV})(\delta\phi_\theta)^2 \tag{2.20}$$

which, for $K_{IGV} = 1$, can be restated

$$\Psi(\xi) - \psi_c'(\Phi + \delta\phi, \varepsilon) + \mathcal{L}\frac{d\Phi}{d\xi} + m\left.\frac{\partial\delta\varphi}{\partial\xi}\right|_I + \lambda\frac{\partial\delta\phi}{\partial\theta} + \mu\frac{\partial\delta\phi}{\partial\xi} = 0 \tag{2.21}$$

where $\psi_c'(\phi, \varepsilon)$ is the total-to-static (as opposed to the static-to-static, ψ_c^{ss}) axisymmetric compressor pressure-rise characteristic[2], and $\mathcal{L} = L_I + \mu + L_E$ is the total effective length of the flow path.

We now can integrate Eq. (2.21) over a cycle of θ realizing that all terms are functions only of time. Doing so and rearranging we obtain

$$\frac{d\Phi}{d\xi} = \frac{1}{\mathcal{L}}\left[\frac{1}{2\pi}\int_0^{2\pi}\psi_c'(\Phi + \delta\phi, \varepsilon)\, d\theta - \Psi(\xi)\right] \tag{2.22}$$

Eq. (2.21) and Eq. (2.22) are two of the three main equations describing the flowfield behavior.

Plenum and Throttle

The third equation that completes the general description of the flowfield comes from balancing the mass entering the plenum from the compressor, the mass leaving the plenum through the throttle, and the mass being stored in the plenum. The processes of gas compression and expansion in the plenum are assumed isentropic. Given the

[2]The prime on any variable, such as ψ_c', indicates that the variable will be *rescaled* later, at which time the prime will be removed.

nondimensionalization adopted so far, the mass balance may be written

$$\frac{d\Psi}{d\xi} = \frac{1}{4B^2\mathcal{L}}\left(\Phi(\xi) - \Phi_T(\xi)\right) \tag{2.23}$$

where

$$B = \frac{U}{2a_s}\sqrt{\frac{\mathcal{V}}{\mathcal{A}\tilde{\mathcal{L}}}} \tag{2.24}$$

is the familiar B-parameter representing the ratio of compliance to inertia in the compression system, a_s is the speed of sound, and $\Phi_T(\xi)$ is the flow through the throttle. In the case of a short enough throttle duct, Φ_T becomes mainly governed by the throttle pressure drop characteristics

$$\Psi = \psi_T'(\Phi_T) \qquad \text{or} \qquad \Phi_T = {\psi_T'}^{-1}(\Psi) \tag{2.25}$$

where the pressure at the exit of the throttle duct is assumed to be the same constant pressure as that at the system inlet, p_{tA}.

2.1.2 Galerkin Approximation of Flowfield Equations

We now set out to transform the PDE in Eq. (2.21) into a set of ODE's by means of a weighted residual method known as the Galerkin approximation [83]. In so doing we exploit the circumferential periodicity of flowfield disturbances by representing them as Fourier series in θ. We thus begin by writing down an approximate solution[3] for the flow potential disturbance, $\delta\varphi$, in the inlet duct, $Z \leq 0$. The following Fourier series of N terms is selected

$$\delta\varphi(\theta, Z, \xi) = \sum_{n=1}^{N} \frac{1}{n}\, e^{nZ}\ \left[a_n'(\xi)\cos(n\theta) + b_n'(\xi)\sin(n\theta)\right] \tag{2.26}$$

[3]The approximation is due to the truncation of the series.

which approximately vanishes at $Z = -L_I$, provided that L_I is large enough such that $e^{n(-L_I)} \approx 0$. The flow coefficient disturbance can now be written as

$$\delta\phi(\theta,\xi) = \left.\frac{\partial\delta\varphi}{\partial Z}\right|_I = \sum_{n=1}^{N} a'_n \cos n\theta + b'_n \sin n\theta \tag{2.27}$$

Substituting the above expression into Eq. (2.21) negates the equality, producing instead a residual $\mathcal{R}$ on the RHS. In order to minimize $\mathcal{R}$, we set the inner product of $\mathcal{R}$ with some weighting functions to zero. In the Galerkin approximation, the weighting functions are chosen to be of the same form as the approximate solution given in Eq. (2.26). These conditions are written as follows

$$\int_0^{2\pi} \mathcal{R}\; d\theta = 0 \tag{2.28}$$

$$\int_0^{2\pi} \mathcal{R}\; \cos(n\theta)\; d\theta = 0 \tag{2.29}$$

$$\int_0^{2\pi} \mathcal{R}\; \sin(n\theta)\; d\theta = 0 \tag{2.30}$$

The first of these integrals reproduces Eq. (2.22), while the second and third integrals produce

$$\frac{da'_n}{d\xi} = \frac{n}{m+n\mu}\left[\frac{1}{\pi}\int_0^{2\pi} \psi'_c\; \cos(n\theta)\; d\theta \;-\; n\lambda b'_n\right] \tag{2.31}$$

$$\frac{db'_n}{d\xi} = \frac{n}{m+n\mu}\left[\frac{1}{\pi}\int_0^{2\pi} \psi'_c\; \sin(n\theta)\; d\theta \;+\; n\lambda a'_n\right] \tag{2.32}$$

where $n = 1, 2, \ldots, N$. The flowfield description is now complete in this general form consisting of $2 + 2N$ equations: the averaged system momentum balance, Eq. (2.21), the plenum mass balance, Eq. (2.23), and the $2N$ equations describing the dynamics of the flowfield nonuniformity, Eqs. (2.31) and (2.32).

It is useful also to derive the polar form of Eqs. (2.31) and (2.32) such that the flowfield nonuniformity is represented in terms of amplitude and phase instead of the Cartesian coordinates a'_n and b'_n. The Fourier series for $\delta\varphi$ and $\delta\phi$ in this case are

given by

$$\delta\varphi(\theta, Z, \xi) = \sum_{n=1}^{N} \frac{1}{n}\, e^{nZ}\; A'_n(\xi)\; \cos\left[n(\theta - \eta_n(\xi))\right] \tag{2.33}$$

$$\delta\phi(\theta, Z, \xi) = \sum_{n=1}^{N} A'_n(\xi)\; \cos\left[n(\theta - \eta_n(\xi))\right] \tag{2.34}$$

For this to be equivalent to Eq. (2.26), one may easily show that the following relations should hold

$$a'_n = A'_n \cos(n\eta_n) \qquad \text{and} \qquad b'_n = A'_n \sin(n\eta_n) \tag{2.35}$$

$$A_n = \sqrt{{a'_n}^2 + {b'_n}^2} \qquad \text{and} \qquad \eta_n = \tan^{-1}\frac{b'_n}{a'_n} \tag{2.36}$$

Following a similar procedure as in the Cartesian case, and using $\cos n\varrho_n$ and $\sin n\varrho_n$ as weighting functions (where $\varrho_n = \theta - \eta_n$, $\dot{\varrho}_n = -\dot{\eta}_n$ and $d\varrho_n = d\theta$), the polar counterparts of Eqs. (2.31) and (2.32) are found to be

$$\frac{dA'_n}{d\xi} = \frac{n}{m + n\mu}\left[\frac{1}{\pi}\int_0^{2\pi} \psi'_c\; \cos n(\theta - \eta_n)\; d\theta\right] \tag{2.37}$$

$$\frac{d\eta_n}{d\xi} = \frac{n}{m + n\mu}\left[\lambda + \frac{1}{nA'_n}\cdot\frac{1}{\pi}\int_0^{2\pi} \psi'_c\; \sin n(\theta - \eta_n)\; d\theta\right] \tag{2.38}$$

This completes the general flowfield model. In order to take this any further, we first need to introduce the geometry of the rotordynamic model and then choose a mathematical representation of the two characteristic functions ψ'_c and ψ'_T. We defer the latter task until we reach the discussion of the baseline model, Section(2.3), and start next with the rotordynamic aspects of the model in order to introduce the relevant geometry.

2.2 Rotordynamic Description

In general the rotating structure in an axial compression system is comprised of a spinning shaft[4] which carries the rotating discs and blades (which we call the rotor-blade rows, as opposed to the stator-blade rows which are mounted to the stationary casing). The shaft is usually supported by some arrangement of bearings which carry the operational load and the weight of the rotating structure. The dynamic characteristics of the bearings play an important role in determining the rotordynamic behavior of the structure as a whole.

The geometry and configuration of this rotating assembly and its support is usually complicated. Nevertheless, the discipline of rotordynamics has produced elaborate analytical and numerical models that—given the detailed configuration of a particular system—provide accurate predictions of the dynamic characteristics of such complex rotating machines.

In this thesis, however, we limit our rotordynamic modeling to the simplest of these models; namely the Jeffcott rotor model [46]. The main reason is that we are mainly interested in understanding the basic nature of the coupling between aerodynamics and rotordynamics, rather than in obtaining accurate quantitative predictions for a specific machine or configuration. For such purposes, the modeling strategy should be one that includes the minimum number of elements and the smallest set of parameters, hence producing models that are readily amenable to analysis and manipulation while capturing the essential aspects of the physical system at hand. Such models usually serve best in revealing the essence of phenomena that may otherwise seem complicated and intractable. Further, the Jeffcott rotor model has been consistently used as the standard tool for this class of analysis throughout the rotordynamic literature.

[4] In modern jet engines, for example, more that one shaft could be arranged inside of one another, separated by bearings and spinning at different speeds.

2.2.1 Overview of the Jeffcott Rotor

The typical Jeffcott rotor is described in several sources such as [18, 6, 78]. However, we adopt a slightly generalized version of the Jeffcott rotor suitable for our purposes. We model the rotating assembly as a single disc whose mass represents the lumped mechanical inertia of the whole rotating assembly, mounted on a massless shaft of finite elasticity and uniform cross section. Both the shaft and the disc spin at a constant speed about their common axis as one unit. The disc center of mass is assumed to be eccentric from the spinning axis producing a "centrifugal force" known as the imbalance force F^{im} which is virtually always present in any type of rotating machinery. Similar to any simple vibratory system, the Jeffcott rotor has a natural frequency ω proportional to the ratio of its stiffness to inertia. Furthermore, the rotating assembly is acted upon by several other internal (e.g., shaft stiffness and internal damping) and external forces (e.g., forces produced by the surrounding fluid and/or support bearings).

Figure 2-2 is a schematic of the basic geometry of the Jeffcott rotor showing the main dimensions and displacements (with highly exaggerated proportions). In this figure, the whirl (or precessional) motion of the rotor is represented by the angle Θ together with the radial displacement of the rotor disc r (i.e., the distance between points O_c and O). The time derivative $\dot{\Theta}$ thus represents the whirl frequency ω^{wh}. Alternatively, the Cartesian coordinates of the rotor disc center X and Y can be used to describe the disc whirling motion. On the other hand, the spin (or running) frequency of the disc about its axis (point O) is labeled Ω. The offset of the disc center of mass (point CG) from the geometric center is known as the amount of imbalance or eccentricity $e = \tilde{e}/l$.

Several important relations can be deduced from the geometry shown in this figure. The local tip clearance normalized by the blade chord, $\varepsilon(\theta, \xi) = \tilde{\varepsilon}/l$, is related to the rotor displacement, $r = \tilde{r}/l$, for small perturbatiosn, as follows

$$\varepsilon(\theta, \xi) = \bar{\varepsilon} - r(\xi)\cos(\theta - \Theta(\xi)) \tag{2.39}$$

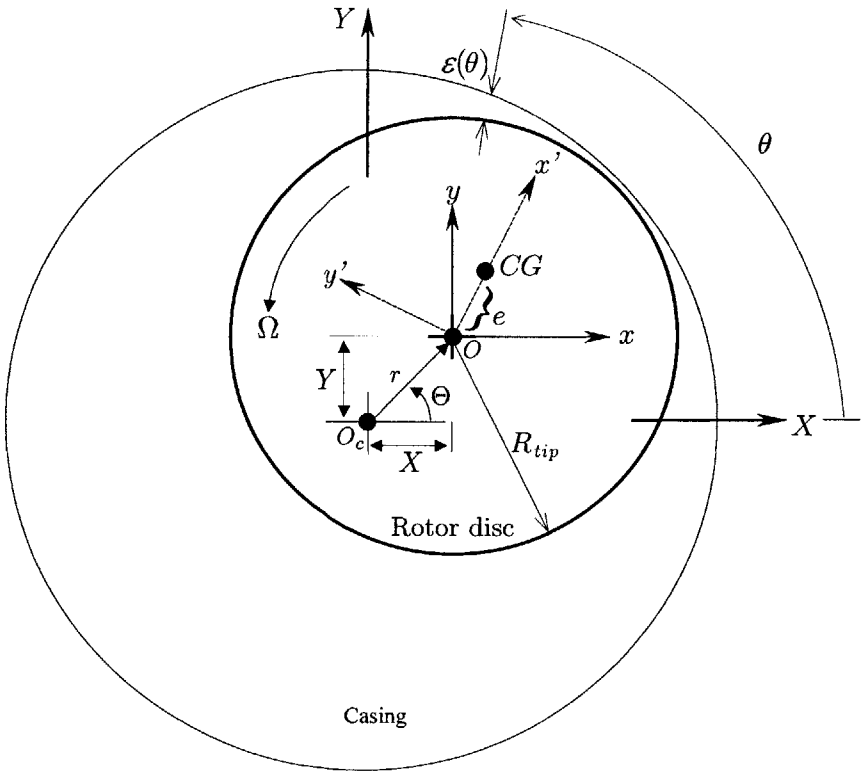

Figure 2-2: A schematic showing the basic rotor geometry (exaggerated proportions).

where $\bar{\varepsilon}$ is the mean tip clearance when $r = 0$. Also the polar and Cartesian coordinates of the rotor center are related as usual by

$$\mathbf{r} = X\,\mathbf{i} + Y\,\mathbf{j} \tag{2.40}$$

$$X(\xi) = r(\xi)\cos(\Theta(\xi)) \qquad \text{and} \qquad Y(\xi) = r(\xi)\sin(\Theta(\xi)) \tag{2.41}$$

$$r = \sqrt{X^2 + Y^2} \qquad \text{and} \qquad \tan\Theta = \frac{Y}{X} \tag{2.42}$$

At this point, it is perhaps instructive to summarize the main features of the classical Jeffcott rotor in order to gain familiarity with the its dynamic character. The effect of imbalance on the dynamic system response is the main phenomenon originally addressed by the Jeffcott rotor model, which established that the presence of imbalance results in a specific rotor response known as synchronous whirl motion, in which the spin and whirl frequencies are equal, i.e., $\Omega = \omega^{wh}$. It also explained

the large amplitude in r observed when the spin frequency Ω (which equals ω^{wh} for imbalance) matches the natural frequency of the rotating assembly, ω, as resonant behavior. Finally, it demonstrated the phase relationship between the motion of the center of mass (point CG) and the motion of the disc center (point O). One counter-intuitive result produced by this model is that when the disc spins at high enough Ω (relative to the natural frequency ω), point CG is flying inward (i.e., point CG is 180° out of phase with r), while the amplitude of the whirl is equal to the imbalance (i.e., $r = e$). In other words, even at high spinning speeds ($\Omega/\omega \gg 1$) and with the presence of imbalance, points CG and O_c coincide and the response is bounded and quite acceptable.

We conclude this section by noting that three important frequencies emerged so far in describing the rotordynamic model, and are restated as follows. The first is Ω, the spinning frequency of the disc and shaft about their common geometric axis. The second is $\omega^{wh} = \dot{\Theta}$, the orbital frequency of point O about point O_c, Figure 2-2, called the whirl frequency. The third is ω, the natural frequency of the rotating assembly, which we will predictably find later to be proportional to the ratio of mechanical stiffness to inertia.

2.2.2 Classification of Forces Acting on the Rotor

We now provide a brief description of forces acting on the rotor, their sources and modeling considerations.

Stiffness forces, (F^{st}). Traditionally, the basic Jeffcott rotor model makes a distinction between stiffness restoring forces due to shaft elasticity and those due to support bearing compliance. The simplest Jeffcott rotor, for instance, assumes an elastic shaft supported by rigid bearings. Adding the effect of bearing compliance can then be viewed as adding another spring in series to that of the shaft. The distinction however allows for a better quantitative evaluation of the stiffness parameters (spring constants) based on the individual configuration and material properties of both the

bearings and the shaft. It also allows the model to better guide the designer in making specific design choices in order to achieve a desired dynamic response. More sophisticated representations of stiffness forces have been included in the Jeffcott rotor model to account for several observed behaviors. These are essentially concerned with:

- Stationary stiffness orthotropy in the bearings: This represents the case of having different bearing spring constants in the X and Y directions. Such orthotropy has a stabilizing effect in that it increases the critical spin frequency[5] Ω above which instability may occur (see for example Childs [6, Section 1.6]).
- Rotating stiffness orthotropy in the rotor: Because of the rotation of the shaft, this kind of orthotropy produces a rotating spring force which does not always act as a pure restoring force. Instead, a component of this spring force contributes to the whirling motion and may thus lead to what is known as a parametric instability.
- Stiffness nonlinearity: This includes hardening and softening spring effects, as well as the variation of stiffness over a cycle of the rotor whirl orbit due to rubbing (known as the normal-tight condition) or due to excessive bearing clearance (known as normal-loose condition). The rotordynamic response under such conditions can be very complicated and may even display chaotic behavior. An overview of this topic is given by Ehrich [20].

In this thesis, we combine the stiffness effect of the shaft and bearings into one lumped stiffness. However, we allow an additional nonlinear (cubic) term to represent a hardening system spring. We also introduce a detuning parameter to allow the X and Y bearing (stationary) stiffnesses to vary independently.

Damping forces, (F^{da}). These include forces due to aerodynamic drag, internal shaft damping, oil-film damping in journal bearings, and squeeze-film damping used commonly with roller-element bearings. Similar to the stiffness case, the internal

[5]It is more accurate to speak of the ratio Ω/ω which is equal to $1/\nu$ in this thesis.

shaft damping may (e.g., in the presence of material hysteresis) produce a force that contributes to whirl-like instabilities. In fact, this historically is the first effect to be recognized as a source of whirl-type, self-excited instabilities. In order to limit the sources of rotordynamic instability, we lump all damping effects in a single linear term of the viscous drag type. We further assume no material hysteresis, yet allow the X and Y damping coefficients to vary independently by introducing a detuning parameter.

Imbalance force, (F^{im}). The source of rotor imbalance is the presence of an offset of center of mass from the geometric, rotational center. No rotor can be perfectly balanced, and thus imbalance is often the main source of excitation in rotordynamics. As we described earlier in Section 2.2.1, the main goal of the Jeffcott rotor model was to address the rotordynamic response to imbalance.

Gravity force, (F^{gr}). There are several effects of gravity on a horizontal rotor, all of which arise from the interaction between the gravity force (which is constant in magnitude and direction) on one hand, and the rest of the forces acting on the rotor on the other. For example, the presence of gravity produces a harmonic forcing for an observer in the rotor frame, which in turn produces alternating bending stresses in the shaft, and hence, can influence the destabilizing effect of internal shaft damping due to material hysteresis. Gravity can also cause the shaft to "sag" during times of shut-down (also known as shaft-bow). Such a bow can change the rotordynamic response to imbalance described above and should be taken into account if present.

In this thesis, however, we do not consider neither internal shaft damping nor shaft-bow. Instead we introduce gravity force merely to produce a class of equilibrium (or "fixed") points in which there is a steady offset in the rotor position corresponding to a stationary tip-clearance asymmetry, and hence a steady nonuniform flow. This class of equilibrium points may change the overall stability picture of the coupled system as will be shown later.

Aerodynamic (fluid) forces, (F^{ae}). *Also known as fluid-induced rotordynamic forces.* In this thesis we restrict these to compressor forces. Other Aerodynamic or fluid related forces, e.g., due to turbines and seals are classified under "other forces" below. Given the current state of understanding of these forces discussed in Section 1.2, the modeling and the effects of compressor aerodynamic forces comprise an important component of this study and are described in detail in the remainder of Chapter 2 and most of Chapter 3.

Harmonic (Periodic) excitation forces, (F^{ha}). These forces are mainly introduced to account for different sources of noise and disturbances to which the rotor might be subjected, and to simulate rotordynamic excitations at any desired amplitude and frequency that could result from external or internal unmodeled effects.

Other forces, (F^{other}). Several other forces may be acting on rotors of axial compressors which are not considered in this study. Examples include Alford-type forces on the turbine side of a gas turbine engine, fluid forces from seals and journal bearings, and actuation forces of magnetic bearings. The uncoupled rotordynamic response to most of these forces have been addressed by many researchers. Further, including these forces in an integrated model such as the one considered in this thesis can result in unwarranted complexity and prevent clear understanding of the basic coupling phenomena. Including these forces may therefore be viewed as a useful extension to the current work that can be considered after the simplest, most basic coupling model has been explored.

2.2.3 Modeling of Forces Acting on the Rotor

Three Contributions of Aerodynamic Forces

We start by realizing that there are in fact *three* contributing effects responsible for generating the total aerodynamic force on the rotor of an axial turbomachine, all of

which can be traced to one source; namely the presence of a nonuniform flowfield surrounding (and exchanging momentum with) the rotor[6]. The first contribution arises from the fact that a nonuniform flowfield generates a circumferential distribution of flow velocity. As the flow passes through the rotor blade rows, the nonuniform flow velocity distribution results in various blades having to do unequal amount of turning and thus being subject to nonuniform loading. The integrated effect of this uneven blade loading is a net force on the rotor we call the turning force, F^{tu}. The second contribution comes from the hydrostatic pressure distribution around the rotor which also produces a net force we call the pressure force, F^{pr}. Finally, the unsteady momentum storage within the rotor gives rise to the third aerodynamic force contribution which we label as the unsteady force, F^{un}. All these forces must be taken into account for a reliable description of the coupling phenomena at hand.

Momentum Equation

To model these effects, we consider a control volume (CV) enclosing the rotating assembly such that the flow entering and leaving every rotor blade row also enters and leaves the control volume by crossing the control surface (CS) as shown in Figure 2-3. Further, we assume that the control volume is *non-rotating* and is fixed to the translating frame, xyz, which is in turn attached to the geometric center of the rotor, point O, and hence has the same rectilinear acceleration as that point. The advantage of selecting such a control volume over other equally valid choices is the convenience of accounting for momentum entering and leaving in terms of the flowfield quantities available from the Moore-Greitzer model in a straightforward manner. The general vector form of the momentum equation applicable to this choice of control volume is given in terms of dimensional quantities (marked by the tilde, e.g., $\tilde{F}$) as follows

$$\sum_{\substack{\text{CS \&}\\ \text{Body}}} \tilde{\mathbf{F}} - \int_{\text{CV, fluid}} \tilde{\mathbf{a}}\ \rho\ d\mathcal{V} - \int_{\text{CV, solid}} \tilde{\mathbf{a}}\ \rho_s\ d\mathcal{V} = \frac{\partial}{\partial t} \int_{\text{CV}} \tilde{\mathbf{v}}_{xyz}\ \rho\ d\mathcal{V} + \int_{\text{CS}} \tilde{\mathbf{v}}_{xyz}\ \rho\ \tilde{\mathbf{v}}_{xyz} \cdot d\mathcal{A} \qquad (2.43)$$

[6]Flow nonuniformity can be the result of several effects. One such effect of particular importance in an axial turbomachine is the tip clearance asymmetry which we consider in this study.

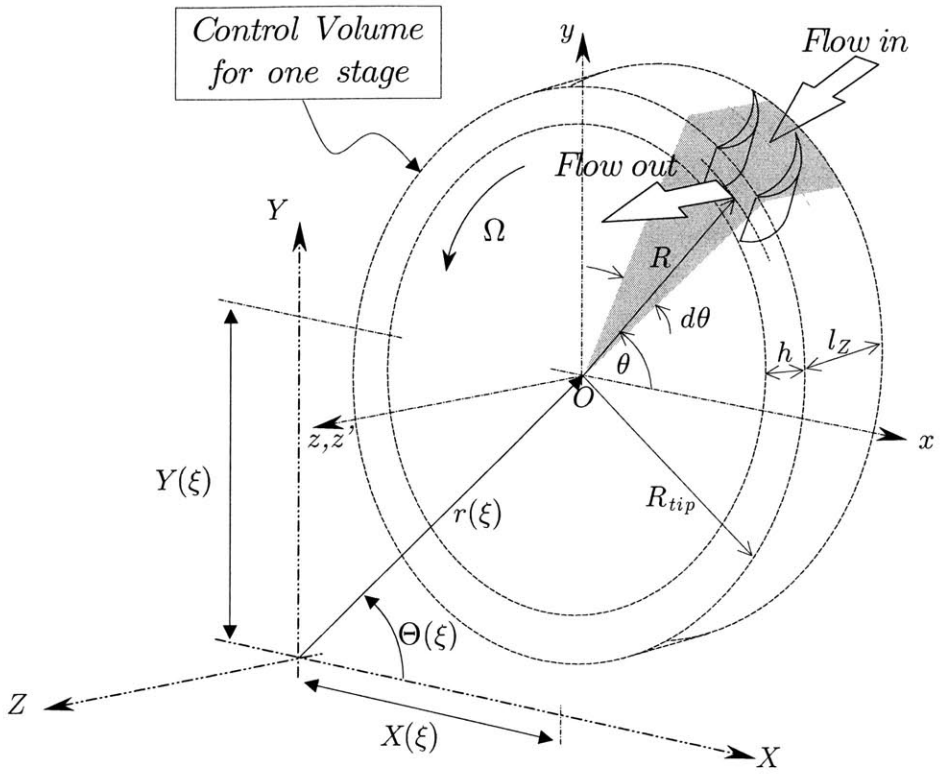

Figure 2-3: A schematic of the control volume for one stage of the rotating assembly.

where all the accelerations are measured in the inertial frame XYZ while the velocities are measured in the translating frame xyz. We may directly realize that the order of the acceleration terms (second and third terms on the left hand side) can be compared by the ratio of fluid to solid densities, ρ/ρ_s, and that the second term could be neglected in comparison to the third as long as $\rho/\rho_s \ll 1$. We thus neglect the second term involving ρ right from the start. Next, we rearrange this equation to take the familiar form $\sum \mathbf{F} = M\mathbf{a}$ by collecting all the force terms on one side, including the momentum influx and unsteady momentum terms which will soon be defined as two of the three aerodynamic forces mentioned above. This generates the following

equation

$$\int_{\text{CV, solid}} \tilde{\mathbf{a}}\ \rho_s\ d\mathcal{V} = \sum_{\substack{\text{CS \&} \\ \text{Body}}} \tilde{\mathbf{F}} - \frac{\partial}{\partial t}\int_{\text{CV}} \tilde{\mathbf{v}}_{xyz}\ \rho\ d\mathcal{V} - \int_{\text{CS}} \tilde{\mathbf{v}}_{xyz}\ \rho\ \tilde{\mathbf{v}}_{xyz} \cdot d\mathcal{A} \tag{2.44}$$

The acceleration term on the left hand side can simply be written as

$$\int_{\text{CV, solid}} \tilde{\mathbf{a}}\ \rho_s\ d\mathcal{V} = M\ \tilde{\mathbf{a}}^{CG}_{XYZ} = N_{st}\ M_{st}\ \tilde{\mathbf{a}}^{CG}_{XYZ} \tag{2.45}$$

where M and M_{st} are the total and per-stage mechanical mass of the rotating assembly, N_{st} is the number of stages and $\tilde{\mathbf{a}}^{CG}_{XYZ}$ is the acceleration of the center of mass of the rotor in the absolute frame XYZ.

Forces

We start with the imbalance force, $\tilde{\mathbf{F}}^{im}$, and show that it emerges from the acceleration term in the last equation. This can be seen by writing $\tilde{\mathbf{a}}^{CG}_{XYZ}$ in terms of the acceleration of point O, $\tilde{\mathbf{a}}^{O}_{XYZ} = \ddot{\tilde{\mathbf{r}}}$, and taking into account the rotation of CG (which is fixed in the frame $x'y'z'$). Note that both O and CG are spinning with the disc at the *constant* rate Ω, see Figure 2-2. Therefore, we may write

$$\begin{aligned}
\tilde{\mathbf{a}}^{CG}_{XYZ} &= \frac{d^2(\tilde{\mathbf{r}} + \tilde{\mathbf{e}})}{dt^2} \\
&= \frac{d^2\tilde{\mathbf{r}}}{dt^2} + \boldsymbol{\Omega} \times (\boldsymbol{\Omega} \times \tilde{\mathbf{e}}) \\
&= (\frac{d^2\tilde{X}}{dt^2} - \tilde{e}\Omega^2 \cos\Omega t)\mathbf{i} + (\frac{d^2\tilde{Y}}{dt^2} - \tilde{e}\Omega^2 \sin\Omega t)\mathbf{j}
\end{aligned} \tag{2.46}$$

We leave only the $(d^2\tilde{\mathbf{r}}/dt^2)$ term on the LHS of the momentum equation, Eq. (2.44), and define the imbalance force $\tilde{\mathbf{F}}^{im}$ on the RHS to be

$$\begin{aligned}
\tilde{\mathbf{F}}^{im} &= -M\ [\ \boldsymbol{\Omega} \times (\boldsymbol{\Omega} \times \tilde{\mathbf{e}})\ ] \\
&= N_{st}\ M_{st}\ \tilde{e}\ \Omega^2\ (\cos\Omega t\ \mathbf{i} + \sin\Omega t\ \mathbf{j})
\end{aligned} \tag{2.47}$$

Going back to Eq. (2.44), the first term on the right hand side represents all the body forces (e.g., gravity) and the forces acting on the control surface which include those due to damping, stiffness, and hydrostatic pressure. In other words,

$$\sum_{\substack{\text{CS \&} \\ \text{Body}}} \tilde{\mathbf{F}} = \tilde{\mathbf{F}}^{da} + \tilde{\mathbf{F}}^{st} + \tilde{\mathbf{F}}^{gr} + \tilde{\mathbf{F}}^{ha} + \tilde{\mathbf{F}}^{pr} + \tilde{\mathbf{F}}^{other} \tag{2.48}$$

We start with the damping and stiffness forces which we define as

$$\tilde{\mathbf{F}}^{da} = -c_X \dot{\tilde{X}}\ \mathbf{i} - c_Y \dot{\tilde{Y}}\ \mathbf{j} \tag{2.49}$$

$$\tilde{\mathbf{F}}^{st} = -(k_X \tilde{X} + k_X^{ns} \tilde{X}^3)\ \mathbf{i} - (k_Y \tilde{Y} + k_Y^{ns} \tilde{Y}^3)\ \mathbf{j} \tag{2.50}$$

where we lump the total damping on the rotor in the linear form of viscous drag, while we include both linear and a cubic terms to represent the stiffness force of a hardening spring. In addition, we allow the X and Y components of each of these forces to be generally different.

The gravity and periodic excitation forces are simply

$$\tilde{\mathbf{F}}^{gr} = -M g_Y\ \mathbf{j} \tag{2.51}$$

$$\tilde{\mathbf{F}}^{ha} = (\tilde{f}_X \cos \Omega^{ha} t\ \mathbf{i} + \tilde{f}_Y \sin \Omega^{ha} t\ \mathbf{j}) \tag{2.52}$$

where the gravity vector is assumed to be in the negative Y direction.

We now point out the first of the aerodynamic forces, $\mathbf{F}^{pr}$, which can be written in the following general form

$$\tilde{\mathbf{F}}^{pr} = -\int_{\text{CS}} p\ d\boldsymbol{\mathcal{A}} \tag{2.53}$$

Next we define the unsteady and turning aerodynamic forces, $\tilde{\mathbf{F}}^{un}$ and $\tilde{\mathbf{F}}^{tu}$, to be the unsteady momentum and momentum influx terms (second and third terms on RHS

of Eq. (2.44) respectively

$$\tilde{\mathbf{F}}^{un} = -\frac{\partial}{\partial t}\int_{\text{CV}} \tilde{\mathbf{v}}_{xyz}\, d\mathcal{V} \tag{2.54}$$

$$\tilde{\mathbf{F}}^{tu} = -\int_{\text{CS}} \tilde{\mathbf{v}}_{xyz}\, \tilde{\mathbf{v}}_{xyz} \cdot d\boldsymbol{\mathcal{A}} \tag{2.55}$$

The above results are general in the sense that, given the flowfield quantities (velocity and pressure distribution) as functions of space and time, the forces on any rotor operating in (and exchanging momentum with) that flowfield may be calculated. It should be noted that in order to evaluate the integrals in the above expressions, details about the flow within the turbomachine (inlet, exit and inter-stage flow quantities) are needed. In the case of an axial compressor, the Moore-Greitzer model derived in the previous section provides knowledge of the flowfield quantities only at the compressor inlet and exit. The detailed inter-stage flow information is not directly available from such a model. To resolve this difficulty, we later introduce assumptions regarding the stage-by-stage performance of a typical axial compressor in order to relate the inter-stage flow velocities and static pressures to those at the inlet and exit of the compressor. In other words, we need to write components of $\mathbf{v}_{xyz}$ entering and leaving each rotor-blade row in terms of the known flow coefficient $\phi = \Phi + \delta\phi$ on the one hand, and write p in terms of the known pressures p_I and p_E on the other.

2.2.4 Coupling Parameters and Nondimensionalization

The above expressions are now rewritten in a nondimensional form consistent with that of the flowfield equations. In addition, we construct the main nondimensional parameters governing this part of the model based on the derived equations and the geometry shown in Figure 2-3. We thus proceed as before by letting $\xi = t\Omega$ and $\mathbf{v} = \tilde{\mathbf{v}}/(R\Omega)$. Pressure is again normalized by the factor $\rho(R\Omega)^2$ while the rotor displacement $\tilde{r}$ (and thus $\tilde{X}$ and $\tilde{Y}$), as well as the imbalance $\tilde{e}$ are all normalized by

the rotor blade chord l. Therefore, the acceleration term becomes

$$\frac{d^2\mathbf{r}}{d\xi^2} = \frac{1}{l\Omega^2}\frac{d^2\tilde{\mathbf{r}}}{dt^2} \tag{2.56}$$

The three aerodynamic forces are nondimensionalized as follows

$$\tilde{\mathbf{F}}^{tu} = -\rho R^2\Omega^2\mathcal{A}^{tu}\int_{\text{CS}}\mathbf{v}_{xyz}\,\mathbf{v}_{xyz}\cdot\frac{d\boldsymbol{\mathcal{A}}}{\mathcal{A}^{tu}} \tag{2.57}$$

$$\tilde{\mathbf{F}}^{pr} = -\rho R^2\Omega^2\mathcal{A}^{pr}\int_{\text{CS}}\frac{p}{\rho R^2\Omega^2}\,\frac{d\boldsymbol{\mathcal{A}}}{\mathcal{A}^{pr}} \tag{2.58}$$

$$\tilde{\mathbf{F}}^{un} = -\rho\Omega^2 R\mathcal{V}^{un}\,\frac{\partial}{\partial\xi}\int_{\text{CV}}\mathbf{v}_{xyz}\,\frac{d\mathcal{V}}{\mathcal{V}^{un}} \tag{2.59}$$

where $\mathcal{A}^{tu}$, $\mathcal{A}^{pr}$ and $\mathcal{V}^{un}$ are needed to complete the nondimensionalization, and are factors proportional to the area through which the flow passes, the area upon which the pressure is acting, and the volume within which the momentum may be stored, respectively. Referring to Figure 2-3 we can see that for an axial compressor of N_{st} similar rotor-blade rows, mean radius R, axial chord $l_Z = l\cos\gamma_r$, and blade span h, we may write these three factors as

$$\mathcal{A}^{tu} = 2\pi\ N_{st}\ R\ h \tag{2.60}$$

$$\mathcal{A}^{pr} = 2\pi\ (2N_{st})\ R\ l_Z \tag{2.61}$$

$$\mathcal{V}^{un} = 2\pi\ N_{st}\ R\ h\ l_Z\tan\gamma_r \tag{2.62}$$

where we take into account the fact that pressure forces act not only on the hub within the rotor-blade row but also on the hub in-between the rotor-blade rows. Hence, the factor $2N_{st}$ is used in $\mathcal{A}^{pr}$ assuming that rotor blade rows and stator-blade rows have approximately the same axial extent. Another approximation used here is that pressure forces act on a cylinder of constant radius R, thus neglecting the variation in CV radius between rotor and stator regions (not significant for high hub-to-tip ratio compressors, which we consider here). We also include $(\tan\gamma_r)$ in the definition of $\mathcal{V}^{un}$ in anticipation of a similar factor produced as a result of averaging the flow

velocity within the control volume as will be shown in the derivation of the baseline model. Finally, in case of the non-similar N_{st} stages, we may choose to define the above factors based on the parameters of the first rotor blade row.

Incorporating the above expressions into Eq. (2.44), dividing through by $(Ml\Omega^2)$, and collecting certain parameters, the momentum equation can be written in the following nondimensional vector form

$$\frac{d^2\mathbf{r}}{d\xi^2} = \mathbf{F}^{da} + \mathbf{F}^{st} + \mathbf{F}^{gr} + \mathbf{F}^{ha} + \mathbf{F}^{im} + \chi \left[-\chi^{tu} \int_{\text{CS}} \mathbf{v}_{xyz}\, \mathbf{v}_{xyz} \cdot \frac{d\mathcal{A}}{\mathcal{A}^{tu}} - \chi^{pr} \int_{\text{CS}} \frac{p}{\rho R^2 \Omega^2} \frac{d\mathcal{A}}{\mathcal{A}^{pr}} - \chi^{un} \frac{\partial}{\partial \xi} \int_{\text{CV}} \mathbf{v}_{xyz} \frac{d\mathcal{V}}{\mathcal{V}^{un}} \right] \tag{2.63}$$

We first turn our attention to the nondimensional parameter, χ, appearing before the aerodynamic force bracket, and with which all the aerodynamic forces scale. This parameter is defined by

$$\boxed{\chi = \frac{N_{st}\, \rho\, (2\pi\, R\, h\, l_Z)}{N_{st}\, M_{st}} = \frac{\text{mass of fluid within CV}}{\text{mass of rotating assembly}}} \tag{2.64}$$

and is called the aerodynamic-rotordynamic coupling parameter. We also note that as $\chi \to 0$ we recover the familiar Jeffcott rotor model in its generalized form. Further, the χ-parameter as constructed above may be viewed as the ratio of fluid mass within the control volume to mechanical mass of the rotating assembly (or the ratio of mass of fluid within one rotor blade row to the mechanical mass of that row). Since M_{st} is also roughly proportional to the dimensions R, h and l_Z, the χ-parameter may be viewed as the ratio of fluid to solid densities, ρ/ρ_s. Therefore, for the same turbomachine geometry, heavier fluid and/or lighter solid would lead to stronger influence of the aerodynamics on the rotordynamics.

Furthermore, it can be seen that the turning, pressure and unsteady forces scale individually with the parameters χ^{tu}, χ^{pr} and χ^{un} respectively. These parameters are

defined as follows

$$\chi^{tu} = \left(\frac{R}{l_Z}\right)^2 \cos\gamma_r = \frac{1}{(AR)_{br}^2} \cos\gamma_r \tag{2.65}$$

$$\chi^{pr} = 2\left(\frac{R}{l_Z}\right)^2 \left(\frac{l}{h}\right) \cos^2\gamma_r = 2\,\frac{1}{(AR)_{br}^2}\,\frac{1}{(AR)_r} \cos^2\gamma_r \tag{2.66}$$

$$\chi^{un} = \left(\frac{R}{l_Z}\right) \cos\gamma_r \tan\gamma_r = \frac{1}{(AR)_{br}} \cos\gamma_r \tan\gamma_r \tag{2.67}$$

These parameters mainly depend on $(AR)_{br}$ and $(AR)_r$, the stage and blade aspect ratios, respectively. For instance, smaller values of $(AR)_{br}$ (i.e., smaller axial blade chord and/or larger mean rotor radius) increase the influence of all three forces, more so for the turning and pressure forces than the unsteady force. On the other hand, smaller values $(AR)_r$ (e.g., shorter blade height) increase only the pressure force, leaving the other two contributions unchanged.

Finally, the nondimensional rotordynamic model can be written in the following compact form

$$\frac{d^2\mathbf{r}}{d\xi^2} = \mathbf{F}^{da} + \mathbf{F}^{st} + \mathbf{F}^{gr} + \mathbf{F}^{ha} + \mathbf{F}^{im} + \mathbf{F}^{ae} \tag{2.68}$$

where the nondimensional forces are given by

$$\mathbf{F}^{da} = -2\zeta\nu\left(\dot{X}\ \mathbf{i} + \sigma^{da}\dot{Y}\ \mathbf{j}\right) \tag{2.69}$$

$$\mathbf{F}^{st} = -(\nu^2 X + \varpi X^3)\ \mathbf{i} - (\sigma^{st}\nu^2 Y + \sigma^{ns}\varpi Y^3)\ \mathbf{j} \tag{2.70}$$

$$\mathbf{F}^{gr} = -G_Y\ \mathbf{j} \tag{2.71}$$

$$\mathbf{F}^{ha} = \bar{f}\left[\cos(\nu^{ha}\xi)\ \mathbf{i} + \sigma^{ha}\ \sin(\nu^{ha}\xi)\ \mathbf{j}\right] \tag{2.72}$$

$$\mathbf{F}^{im} = e\ (\cos\xi\ \ \mathbf{i} + \sin\xi\ \ \mathbf{j}) \tag{2.73}$$

$$\mathbf{F}^{ae} = \mathbf{F}^{tu} + \mathbf{F}^{pr} + \mathbf{F}^{un} \tag{2.74}$$

and,

$$\mathbf{F}^{tu} = \chi\ (\mathbf{F}^{tu})_i = \chi\ \left[-\chi^{tu} \int_{\text{CS}} \mathbf{v}_{xyz}\ \mathbf{v}_{xyz} \cdot \frac{d\boldsymbol{\mathcal{A}}}{\mathcal{A}^{tu}} \right] \tag{2.75}$$

$$\mathbf{F}^{pr} = \chi\ (\mathbf{F}^{pr})_i = \chi\ \left[-\chi^{pr} \int_{\text{CS}} \frac{p}{\rho\Omega^2 R^2}\ \frac{d\boldsymbol{\mathcal{A}}}{\mathcal{A}^{pr}} \right] \tag{2.76}$$

$$\mathbf{F}^{un} = \chi\ (\mathbf{F}^{un})_i = \chi\ \left[-\chi^{un} \frac{\partial}{\partial\xi} \int_{\text{CV}} \mathbf{v}_{xyz}\ \frac{d\mathcal{V}}{\mathcal{V}^{un}} \right] \tag{2.77}$$

In general, the quantities $(\mathbf{F}^{tu})_i$, $(\mathbf{F}^{pr})_i$ and $(\mathbf{F}^{un})_i$, appearing above may be viewed as the *average* aerodynamic force per stage of the compressor. For similar stages, however, these quantities are the nondimensional force per stage. In addition, any of these forces, $(F)_i$, can be viewed as a rescaled version of aerodynamic force, i.e., $(F)_i = F/\chi$.

Quantities appearing above which have not already been defined are given below

$$\zeta = \frac{c_X}{2M\omega} \qquad \nu = \frac{\omega}{\Omega} \qquad \omega = \sqrt{\frac{k_X}{M}}$$

$$\sigma^{da} = \frac{c_X}{c_Y} \qquad \sigma^{st} = \frac{k_X}{k_Y} \qquad \sigma^{ns} = \frac{k_X^{ns}}{k_Y^{ns}}$$

$$\varpi = \left(\frac{l}{\Omega}\right)^2 \frac{k_X^{ns}}{M} \qquad e = \frac{\tilde{e}}{l} \qquad G_Y = \frac{g_Y}{l\Omega^2}$$

$$\bar{f} = \frac{\tilde{f}}{Ml\Omega^2} \qquad \sigma^{ha} = \frac{\bar{f}_X}{\bar{f}_Y} \qquad \nu^{ha} = \frac{\Omega^{ha}}{\Omega}$$

The rotor's undamped natural frequency, ν, is worthy of special attention. It largely determines the response of the Jeffcott rotor model to imbalance which has its maximum rotor deflection at the critical value $\nu = 1.0$. Rotors normally operating at values of $\nu < 1$ are called supecritical rotors, reflecting the fact that the spin frequency Ω is larger the the rotor's natural frequency. A subcritical rotor would naturally have $\nu > 1$. In general, most modern, high speed turbomachines are in the range $0.1 < \nu < 0.5$ and are therefore supercritical at their typical running speeds.

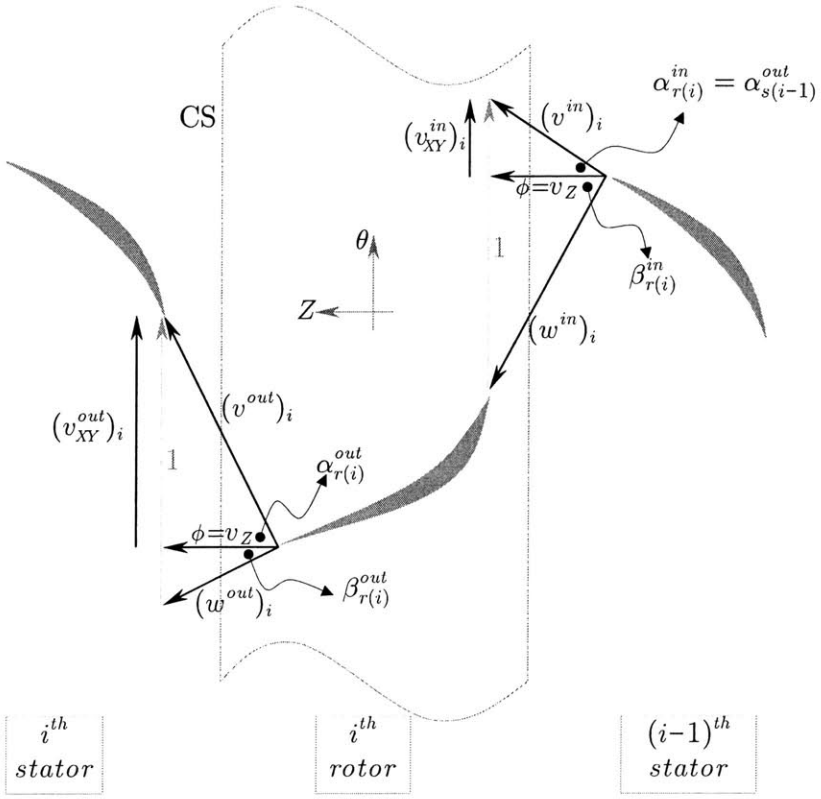

Figure 2-4: Velocity triangles and terminology used in evaluating force expressions.

2.2.5 General Expressions of Aerodynamic Forces

In order to go any further with the evaluation of the integrals appearing in the aerodynamic force expressions, Eqs. (2.57), (2.58) and (2.59), we need to determine the flowfield $\mathbf{v}_{xyz}$. In particular, the velocity entering and leaving each rotor blade row must be determined. In addition, the static pressure distribution around the CV, as well as some form of flow velocity average to be used in evaluating the unsteady momentum terms, needs to be determined. For that we consider the velocity triangles of one stage as shown in Figure 2-4, which depicts the plane containing a segment of the two-dimensional flowfield (i.e., a plane parallel to Z and tangent to the rotor at some circumferential location θ). In Figure 2-5 we show a three-dimensional view of one of the velocity triangles indicating the X and Y components, the angles involved and other relevant dimensions.

We may now write the following relation between the relative and absolute ve-

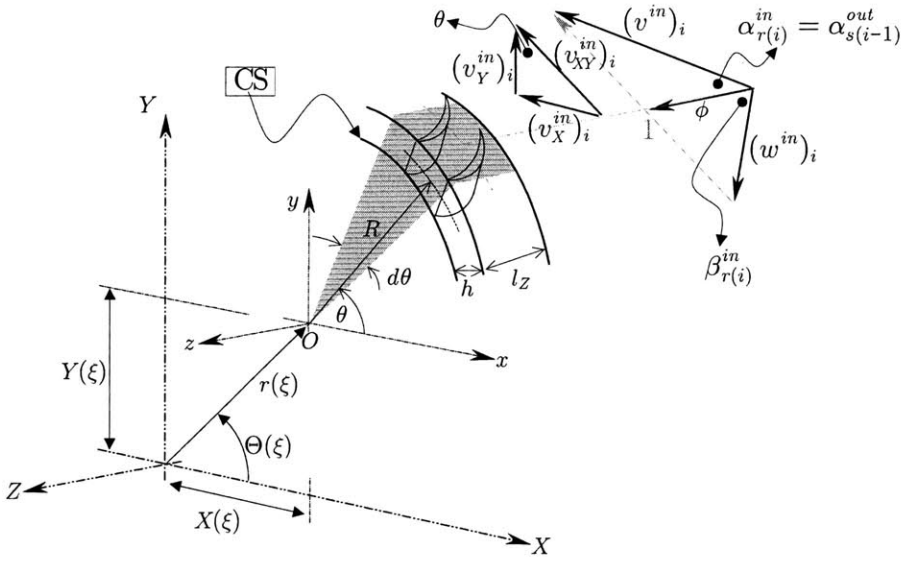

Figure 2-5: Three dimensional Components of velocity triangle.

locities

$$\mathbf{v}_{xyz} = \mathbf{v}_{XYZ} - \frac{l}{R}\frac{d\mathbf{r}}{d\xi} \tag{2.78}$$

Using order-of-magnitude estimates, it can be shown that the second term on the right hand side is very small compared to the flow velocities and may thus be neglected. The required velocity vectors entering and leaving the i^{th} rotor blade row can then be written as

$$\begin{aligned}(\mathbf{v}^{in}_{XYZ})_i &= -v^{in}_X\ \mathbf{i} + v^{in}_Y\ \mathbf{j} + \phi\ \mathbf{k} \\ &= \phi \tan\alpha^{in}_{r(i)}\,[-\sin\theta\ \mathbf{i} + \cos\theta\ \mathbf{j}] + \phi\ \mathbf{k} \qquad (2.79)\\ (\mathbf{v}^{out}_{XYZ})_i &= -v^{out}_X\ \mathbf{i} + v^{out}_Y\ \mathbf{j} + \phi\ \mathbf{k} \\ &= \phi \tan\alpha^{out}_{r(i)}\,[-\sin\theta\ \mathbf{i} + \cos\theta\ \mathbf{j}] + \phi\ \mathbf{k} \qquad (2.80)\end{aligned}$$

and,

$$(\mathbf{v}^{out}_{XYZ})_i - (\mathbf{v}^{in}_{XYZ})_i = \phi(\tan\alpha^{out}_{r(i)} - \tan\alpha^{in}_{r(i)})\,[-\sin\theta\ \mathbf{i} + \cos\theta\ \mathbf{j}] \tag{2.81}$$

We note here that the angles appearing in the above expressions are those of the fluid velocity vectors and not of the blade; the difference being the incidence for entering flow and the deviation for exiting flow. These angles are mainly variations about the blade metal angles $\bar{\alpha}$ and $\bar{\beta}$ dictated by the flowfield and the behavior of the blade row from which the flow is *exiting*. In other words, the angle of the flow entering the ith rotor is set by the performance of the $(i-1)$th stator upstream of that rotor at the given flow coefficient, while the angle of the flow exiting the ith rotor is set by the performance of the same rotor at the corresponding flow coefficient. To reflect this causality argument, we rewrite the above expressions in terms of the angles $\alpha^{out}_{s(i-1)}$ and $\beta^{out}_{r(i)}$, both of which are some function of ϕ specific to the blade row at hand. Further, when operating near the design point these angles are in general close to the metal (blade) angles. It may however be necessary to account for the difference when operating in the remainder of the operating range. For our baseline model discussed in the next section, we will employ simple relations to account for this behavior in as wide of an operating range as possible while avoiding task-defeating complexity. For now, however, we carry on with the derivation of the force expressions in terms of the unknown angle functions $\alpha^{out}_{s(i-1)}(\phi)$ and $\beta^{out}_{r(i)}(\phi)$.

From the velocity triangles we may write the following relations

$$\alpha^{out}_{s(i-1)} = \alpha^{in}_{r(i)} \tag{2.82}$$

$$\tan\beta^{out}_{r(i)} = \frac{1}{\phi} - \tan\alpha^{out}_{r(i)} \tag{2.83}$$

and,

$$\tan\beta^{in}_{r(i)} = \frac{1}{\phi} - \tan\alpha^{out}_{s(i-1)} \tag{2.84}$$

The flow velocity expressions can then be written in terms of these angles as

$$(\mathbf{v}^{in}_{XYZ})_i = \phi\tan\alpha^{out}_{s(i-1)}\left[-\sin\theta\ \mathbf{i} + \cos\theta\ \mathbf{j}\right] + \phi\ \mathbf{k} \tag{2.85}$$

$$(\mathbf{v}^{out}_{XYZ})_i = \left(1 - \phi\tan\beta^{out}_{r(i)}\right)\left[-\sin\theta\ \mathbf{i} + \cos\theta\ \mathbf{j}\right] + \phi\ \mathbf{k} \tag{2.86}$$

and,

$$(\mathbf{v}^{out}_{XYZ})_i - (\mathbf{v}^{in}_{XYZ})_i = \left(1 - \phi\left(\tan\alpha^{out}_{s(i-1)} + \tan\beta^{out}_{r(i)}\right)\right)[-\sin\theta\ \mathbf{i} + \cos\theta\ \mathbf{j}] \tag{2.87}$$

As for the pressure force, the static pressure distribution around the stage is required. We define the following average pressure distribution for the ith stage

$$\bar{p}_i = \frac{p^{in}_i + p^{out}_i}{2} \tag{2.88}$$

which is equivalent to assuming linear variation (increase for a compressor) of static pressure with the axial direction Z. This is a reasonable assumption that is supported by data such as that presented by Lavrich [48].

Finally, to evaluate the unsteady momentum term we consider an average velocity within the stage as follows

$$(\bar{\mathbf{v}}_{XYZ})_i = \frac{(\mathbf{v}^{in}_{XYZ})_i + (\mathbf{v}^{out}_{XYZ})_i}{2} \tag{2.89}$$

$$= \left[1 - \phi\left(\frac{\tan\beta^{in}_{r(i)} + \tan\beta^{out}_{r(i)}}{2}\right)\right][-\sin\theta\ \mathbf{i} + \cos\theta\ \mathbf{j}] + \phi\ \mathbf{k} \tag{2.90}$$

Incorporating the above definitions, and considering a compressor of N_{st} (not necessarily similar) stages, the average aerodynamic forces per stage (see note after Eq. (2.77)) can be written as

$$(\mathbf{F}^{tu})_i = -\chi^{tu}\sum_{i=1}^{N_{st}}\frac{R_i h_i}{\mathcal{A}^{tu}}\int_0^{2\pi}\phi\left[(\mathbf{v}^{out}_{XYZ})_i - (\mathbf{v}^{in}_{XYZ})_i\right]d\theta \tag{2.91}$$

$$(\mathbf{F}^{pr})_i = -\chi^{pr}\sum_{i=1}^{N_{st}}\frac{R_i l_{Zi}}{\mathcal{A}^{pr}}\int_0^{2\pi}\frac{1}{2}\frac{p^{in}_i + p^{out}_i}{\rho\Omega^2 R^2}\ [\cos\theta\ \mathbf{i} + \sin\theta\ \mathbf{j}]\ d\theta \tag{2.92}$$

and,

$$(\mathbf{F}^{un})_i = -\chi^{un} \sum_{i=1}^{N_{st}} \frac{R_i h_i l_{Zi}}{\mathcal{V}^{un}} \frac{\partial}{\partial \xi} \int_0^{2\pi} \bar{\mathbf{v}}_{XYZ} \, d\theta \tag{2.93}$$

We note here that for identical N_{st} stages the factors appearing right before the integrals would sum to 1 after carrying out the integration, which is what we intended when we previously defined $\mathcal{A}^{tu}$, $\mathcal{A}^{pr}$ and $\mathcal{V}^{un}$.

The description of the generalized aerodynamic-rotordynamic coupled model is now complete. It is mainly represented by Eqs. (2.22), (2.23), and the Cartesian equations (2.31) and (2.32) (or their polar counterparts (2.37) and (2.38)) for the flowfield, together with the X and Y components of the rotordynamic equation, Eq. (2.68), along with the associated definitions.

2.3 The Baseline Model

We proceed now to reduce the above generalized model into a lower order form that is more suited for analysis purposes. To achieve that we start by choosing mathematical forms for the pressure-flow characteristics of the compressor and throttle. That allows for the evaluation of the integrals in the flowfield equations, (2.22), (2.31) and (2.32) (or (2.37) and (2.38)). We then truncate the Fourier series at the first harmonic yielding a fourth-order approximation of the Moore-Greitzer model. Finally we simplify and integrate the expressions derived above for the aerodynamic forces and collect the equations, thus completing the derivation of an eighth-order baseline model of the coupled system.

2.3.1 Choice of Compressor and Throttle Characteristics

Choice of Compressor Characteristic

The pressure-rise compressor characteristic, $\psi_c'(\phi, \varepsilon)$, is a simplified representation of the relationship between the compressor's pressure-rise and flow coefficient when a hypothetical steady and axisymmetric flowfield is imagined throughout the range of flow coefficient. However, for certain values of flow coefficient such a flowfield is known to be unstable and thus can not exist. One of the accomplishments of the Moore-Greitzer model is that it provides an approximated correction to this relationship in the case of unsteady, nonaxisymmetric flow conditions, including the conditions of rotating stall and surge.

In the current model we start with the same form of ψ_c' adopted by Moore and Greitzer as the nominal (axisymmetric) characteristic, and modify it with the dependency on tip clearance to generate a family of characteristics as follows

$$\psi_c'(\phi, \varepsilon) = \psi_{c0} H + H\left[1 + \frac{3}{2}\left(\frac{\phi}{W} - 1\right) - \frac{1}{2}\left(\frac{\phi}{W} - 1\right)^3\right] + H\frac{\partial \psi_c}{\partial \varepsilon}(\varepsilon - \bar{\varepsilon}) \qquad (2.94)$$

where we assume linear dependency on local tip clearance $(\varepsilon - \bar{\varepsilon})$. The sensitivity factor $\frac{\partial \psi_c}{\partial \varepsilon}$ is in general a function of ϕ and $\bar{\varepsilon}$ but, in many cases, may reasonably be assumed constant for added simplicity, Graf [29]. This constant is expected to be negative to give the local effect of lower pressure rise for higher tip clearance. We thus acknowledge this fact by defining a "positive" sensitivity constant $\psi_{c\varepsilon} = -\frac{\partial \psi_c}{\partial \varepsilon}$. For further convenience, we rescale the main variables as follows

$$\begin{aligned} q &= \frac{\phi}{2W} & Q &= \frac{\Phi}{2W} \\ \psi_c &= \frac{\psi_c'}{H} & P &= \frac{\Psi}{H} \\ a_n, b_n &= \frac{a_n'}{2W}, \frac{b_n'}{2W} & A_n &= \frac{A_n'}{2W} \end{aligned} \qquad (2.95)$$

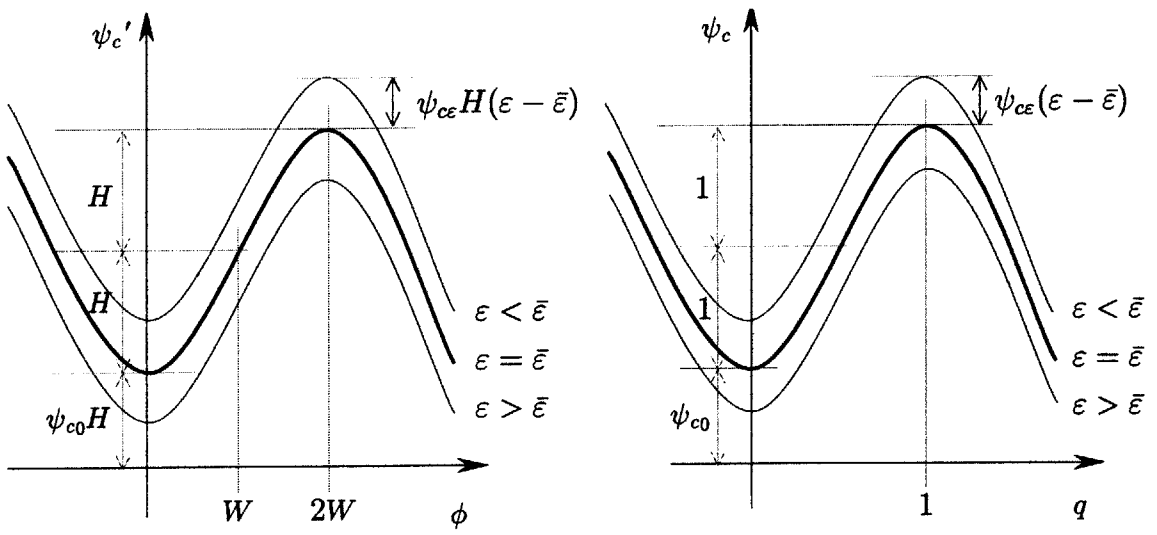

Figure 2-6: General features of the compressor pressure-rise characteristic.

The rescaled flow coefficient may then be expressed as

$$q = Q + \sum_{n=1}^{N} a_n \cos n\theta + b_n \sin n\theta \tag{2.96}$$

$$= Q + \sum_{n=1}^{N} A_n \cos n(\theta - \eta_n) \tag{2.97}$$

The above rescaling scheme is similar, but not identical, to that used by McCaughan [54, 55] in which nondimensional time was also rescaled by the factor $\mathcal{L}/S$ and the flow coefficient was shifted by 1. While the rescaling adopted by McCaughan simplifies the flowfield equations, its benefit is compromised once the rotordynamic model is added into the picture. The rescaling adopted in this study and defined by Eq. (2.95) is more appropriate for the coupled model at hand.

We may now write the compressor characteristic ψ_c as

$$\psi_c(q, r, \Theta) = \psi_{c0} + 1 + 3\,(q - 0.5) - 4\,(q - 0.5)^3 + \psi_{c\varepsilon} r \cos(\theta - \Theta) \tag{2.98}$$

where the relation $\varepsilon - \bar{\varepsilon} = -r\cos(\theta - \Theta)$ from Eq. (2.39) is used. Figure 2-6 shows the main features of this cubic characteristic. We note that the assumption of constant

sensitivity, $\psi_{c\varepsilon}$, has the effect of vertically aligning the peaks of curves corresponding to different tip clearance values. Also, we note that the rescaled compressor characteristic is described only by two parameters, S and ψ_{c0}, and that its peak will always be at $(q, \psi_c) = (1, 2+\psi_{c0})$ regardless of the value of S. Finally, we designate the point at $q = 1.2$ as the design operating point, allowing a reasonable 20% stall margin.

Choice of Throttle Characteristic

The characteristic of the throttle is a simpler function relating the pressure drop and the flow coefficient. A quadratic relationship that is usually used for this purpose and is deemed quite sufficient may be written as

$$\Psi = \psi_T'(\Phi_T) = \frac{H}{\gamma^2}\Phi_T^2 \qquad \text{or} \qquad \Phi_T = {\psi_T'}^{-1}(\Psi) = \frac{2W}{\sqrt{H}}\,\gamma\sqrt{\Psi_T} \tag{2.99}$$

and in rescaled form as,

$$P = \psi_T(Q_T) = \frac{(2W)^2}{\gamma^2}Q_T^2 \qquad \text{or} \qquad Q_T = \psi_T^{-1}(P) = \gamma\sqrt{P} \tag{2.100}$$

For steady, stable and axisymmetric flow conditions, the operating point of the compression system is set by the two characteristics, ψ_c and ψ_T, and is located at their intersection. However, in the presence of a flow asymmetry, such as rotating stall, the operating point is influenced by the nonaxisymmetric part of the flow as described by the full model.

Integrated Forms of the Compressor Characteristic, $N = 1$

Having obtained the form of the compressor characteristic, we may now return to the flowfield model, Eqs. (2.22), (2.31) and (2.32) (or (2.37) and (2.38)), and carry out the integrals appearing therein. Setting $N = 1$ and dropping the corresponding subscript for brevity (i.e., letting $a = a_1$, $A = A_1$ and so on) we find

Cartesian version

$$
\begin{aligned}
\bar{\psi}_c^C &= \frac{1}{2\pi}\int_0^{2\pi} \psi_c \, d\theta \\
&= \underbrace{\psi_{c0} + 1 + 3\,(Q-0.5) - 4\,(Q-0.5)^3}_{\psi_c(Q)} \quad - \underbrace{6(a^2+b^2)\,(Q-0.5)}_{\text{contribution of nonuniformity}} \\
\bar{\psi}_c^{Cc} &= \frac{1}{\pi}\int_0^{2\pi} \psi_c \, \cos\theta \, d\theta \\
&= -3a\left[4Q(Q-1) + (a^2+b^2)\right] + \psi_{c\varepsilon} X \\
\bar{\psi}_c^{Cs} &= \frac{1}{\pi}\int_0^{2\pi} \psi_c \, \sin\theta \, d\theta \\
&= -3b\left[4Q(Q-1) + (a^2+b^2)\right] + \psi_{c\varepsilon} Y
\end{aligned}
\tag{2.101}
$$

Polar version

$$
\begin{aligned}
\bar{\psi}_c^p &= \frac{1}{2\pi}\int_0^{2\pi} \psi_c \, d\theta \\
&= \psi_{c0} + 1 + 3\,(Q-0.5) - 4\,(Q-0.5)^3 - 6A^2\,(Q-0.5) \\
\bar{\psi}_c^{pc} &= \frac{1}{\pi}\int_0^{2\pi} \psi_c \, \cos(\theta-\eta) \, d\theta \\
&= -3A\left[4Q(Q-1) + A^2\right] + \psi_{c\varepsilon} r\cos(\Theta-\eta) \\
\bar{\psi}_c^{ps} &= \frac{1}{\pi}\int_0^{2\pi} \psi_c \, \sin(\theta-\eta) \, d\theta \\
&= \psi_{c\varepsilon} r\sin(\Theta-\eta)
\end{aligned}
\tag{2.102}
$$

Higher order flowfield models can be constrcted in a similar fashion by selecting $N > 1$ as described in Appendix A.

2.3.2 Simplified Expressions of the Aerodynamic Forces

In order to reduce the complexity of the aerodynamic force expressions, Eqs. (2.91)–(2.93), for the baseline model, we assume that the compressor has N_{st} repeated stages of similar dimensions. Further, as discussed earlier, we need to approximate the

behavior of different blade rows in regard to the two main flow angles: that of the flow leaving the stator (in the absolute frame), $\alpha^{out}_{s(i-1)}$, and that of the flow leaving the rotor (in the relative frame), $\beta^{out}_{s(i)}$. All other angles can then be deduced in terms of these two from the velocity triangles shown in Figures 2-4 and 2-5. However, the force expressions for the turning and unsteady contributions do not require explicit knowledge of these angles, but instead only the following combinations are needed

$$\left[\tan\alpha^{out}_{s(i-1)} + \tan\beta^{out}_{r(i)}\right] \qquad \text{and} \qquad \frac{1}{2}\left[\tan\beta^{in}_{r(i)} + \tan\beta^{out}_{r(i)}\right] \tag{2.103}$$

Turning Force

The turning force involves only the first of the above two expressions for which we utilize the Euler turbine equation as applied to a steady, axisymmetric flowfield, and written in nondimensional form as

$$\begin{aligned}\frac{1}{2}(\tau_c)_i &= \phi\left[(v^{out}_{XY})_i - (v^{in}_{XY})_i\right] \\ &= \phi\left[1 - \phi\left(\tan\alpha^{out}_{s(i-1)} + \tan\beta^{out}_{r(i)}\right)\right]\end{aligned} \tag{2.104}$$

This directly gives a relation for the needed angle expression. Further, comparing the above Euler equation to Eq. (2.87), and considering similar stages, one finds that the average (i.e., per stage) turning force is exactly given by

$$(\mathbf{F}^{tu})_i = -\chi^{tu}\,\frac{1}{2\pi}\int_0^{2\pi}\frac{1}{2}(\tau_c)_i\left[-\sin\theta\;\mathbf{i} + \cos\theta\;\mathbf{j}\right]d\theta \tag{2.105}$$

where the stage torque is a quantity that is reasonably measurable or, at least, is of known general qualitative features. For this purpose the following *stage* torque characteristic may be adopted

$$\begin{aligned}(\tau_c)_i &= \frac{(\tilde{\tau}_c)_i}{\frac{1}{2}\rho\Omega^2 R^3 \mathcal{A}_c} \\ &= \tau_{c0} + \tau_{c1}\;q + \tau_{c2}\;q^2 + \tau_{c3}\;q^3 - \tau_{c\varepsilon}\;(\varepsilon - \bar{\varepsilon})\end{aligned} \tag{2.106}$$

where $\mathcal{A}_c$ is the compressor flow through area, $\mathcal{A}_c \approx 2\pi Rh$, and the total compressor torque is simply $N_{st}(\tau_c)_i$.

In order to determine the coefficients in the above equation, we try to match any torque data available for the compressor of consideration. Such data is either available only over a limited part of the operating range, or is reflective of the stalled (as opposed to the axisymmetric) performance over part of the operating range. Therefore we follow a rationale similar to that used in adopting an axisymmetric, hypothetical pressure-rise characteristic in the Moore-Greitzer model. To that end, the torque coefficients are chosen such that the resulting characteristic: has the usual S-shape, matches any available measurements over the stable and reversed-flow portions, and interpolated in between within the limits of a cubic polynomial. Measurements of axial compressor torque over a wide range of operating conditions are reported by Day [11], Gamash [26, 27] and Lavrich [48].

Carrying out the integration yields the final expression of the average turning force required for the baseline model

$$(\mathbf{F}^{tu})_i = \frac{1}{4}\chi^{tu}\left\{ \left[b\ \bar{F}_c^{tu}(Q,a,b) + \tau_{c\varepsilon}Y\right]\ \mathbf{i} + \left[-a\ \bar{F}_c^{tu}(Q,a,b) - \tau_{c\varepsilon}X\right]\ \mathbf{j}\right\} \qquad (2.107)$$

where the function $\bar{F}_c^{tu}(Q,a,b)$ is given by

$$\bar{F}_c^{tu}(Q,a,b) = \tau_{c1} + 2\tau_{c2}\ Q + 3\tau_{c3}\left[Q^2 + \frac{1}{4}(a^2+b^2)\right] \qquad (2.108)$$

It is worth noting here that the above expression differs from that introduced by Thomas [75], or Alford[7] [3], in that the force not only depends on the rotor eccentricity, but is also a function of flowfield *variable* quantities Q, a and b. Therefore, even if the torque characteristic is assumed independent of tip clearance (i.e., setting $\tau_{c\varepsilon}$ equal to zero), the main effect of eccentricity in producing the turning force would still be captured through the flowfield nonuniformity described by the Moore-Greitzer model.

[7] A brief derivation and description of these early works may be found in several rotordynamics books such as Ehrich [18] and Childs [6].

Furthermore, in cases where detailed flowfield information about flow velocities and inlet/exit angles is available (either from experiment or elaborate computations), the more general turning force expression given by Eq. (2.91) may still be used. Finally, this force contribution has traditionally been assumed to be only in the tangential (Θ) direction. However, the above expression suggests that this force may in fact have a radial component which can play a role in the overall stability picture.

Pressure Force

We recall here that the intermediate stage pressure averages, $\bar{p}_i$, which appear in Eqs. (2.88) and (2.92), are not directly available from the Moore-Greitzer model, which gives the pressure only at the compressor inlet and exit, p_I and p_E. To overcome this difficulty, we may estimate the intermediate pressures by starting from a point at which the pressure is available, say p_I. The exit pressure of the first blade row can now be related to p_I through the performance characteristic of that blade row. We may then march through the blade rows and repeat the process. To avoid requiring knowledge of the performance characteristic of individual blade rows, we may alternatively carry the summation in Eq. (2.92) into the integral such that the pressure averages of individual stages (assumed to be similar) can be combined into one pressure average over the whole compressor. This produces the convenient expression

$$(\mathbf{F}^{pr})_i = -\chi^{pr}\,\frac{1}{2\pi}\int_0^{2\pi}\frac{1}{2}\,\frac{p_I+p_E}{\rho\Omega^2R^2}\,\left[\cos\theta\;\mathbf{i}+\sin\theta\;\mathbf{j}\right]\,d\theta \tag{2.109}$$

The required pressure average can be formed using the equations of the inlet and exit ducts, Eqs. (2.10) and (2.18), yielding

$$\begin{aligned}\frac{\bar{p}_{IE}}{\rho\Omega^2R^2} &= \frac{1}{2}\,\frac{p_I+p_E}{\rho\Omega^2R^2}\\ &= \frac{p_{tA}}{\rho\Omega^2R^2}+\frac{1}{2}\Psi-\frac{1}{4}\phi^2-\frac{1}{2}(L_I-L_E)\frac{d\Phi}{d\xi}+\frac{1}{2}(m-2)\frac{\partial\delta\varphi}{\partial\xi}\end{aligned} \tag{2.110}$$

where the $(\delta\phi_\theta)^2$ term from Eq. (2.10) was neglected in comparison to ϕ^2 as discussed for the IGV's and OGV's in Moore [56, Part I]. In addition, since we chose $m = 2$ for the exit duct, the last term in the above expression is also eliminated. Finally, we note that quantities which are not functions of θ will not contribute to the integral in Eq. (2.109). The pressure force thus reduces to the following simple expression

$$(\mathbf{F}^{pr})_i = -\chi^{pr}\ \frac{1}{2\pi}\int_0^{2\pi} -\frac{1}{4}\phi^2\ \left[\cos\theta\ \mathbf{i} + \sin\theta\ \mathbf{j}\right]\ d\theta \tag{2.111}$$

$$= \chi^{pr}\ W^2\ Q\ \left[a\ \mathbf{i} + b\ \mathbf{j}\right] \tag{2.112}$$

We observe here that, just like the turning force contribution, the pressure force may have both tangential (whirl) and radial (restoring) components.

Unsteady Force

Evaluation of the unsteady force contribution involves the second angle combination mentioned in Eq. (2.103). In order to avoid excessive complexity, we note that this angle combination is commonly used to define the angle of the average velocity within a blade passage. We will assume that this averaged angle remains, more or less, constant and is approximated by the blade stagger angle, i.e.,

$$\frac{1}{2}\left[\tan\beta^{in}_{r(i)} + \tan\beta^{out}_{r(i)}\right] \approx \tan\gamma_r \tag{2.113}$$

Examination of detailed flow data, such as that given by Lavrich [48] suggests the adequacy of this representation, especially in unstalled flow conditions.

The unsteady force contribution is therefore given by

$$(\mathbf{F}^{un})_i = \frac{-\chi^{un}}{2\pi\tan\gamma_r}\frac{\partial}{\partial\xi}\int_0^{2\pi}\left\{1 - 2W\ q\ \tan\gamma_r\ \left[-\sin\theta\ \mathbf{i} + \cos\theta\ \mathbf{j}\right] + 2W\ q\ \mathbf{k}\right\}\ d\theta \tag{2.114}$$

from which the final expression can be obtained by carrying out the integration yield-

ing

$$(\mathbf{F}^{un})_i = \chi^{un}\, W \left[-\frac{db}{d\xi}\,\mathbf{i} \;+\; \frac{da}{d\xi}\,\mathbf{j} \;+\; \frac{1}{\tan\gamma_r}\frac{dQ}{d\xi}\,\mathbf{k} \right] \tag{2.115}$$

We may note here that the unsteady force has an axial component in the Z direction, in contrast to the turning and pressure forces which were constrained to the XY plane[8]. However, since we are only interested in rotor vibrations in the XY plane, the axial unsteady force identified above is not relevant in this study.

2.3.3 Summary of the Baseline Model Equations

In this section, we collect the equations developed so far which describe the dynamics of the baseline model. In this eighth order model, the states are Q and P which represent the global system (surge) states; a and b (or A and η) which represent the compressor flow nonuniformity (rotating-stall) states; and finally, $X, Y, \dot{X}, \dot{Y}$ (or $r, \Theta, \dot{r}, \dot{\Theta}$) which are the rotordynamic states. The model is given in terms of the following nonlinear ordinary differential equations.

Flowfield Model. The surge-like dynamics are described by

$$\dot{Q} = \frac{S}{2\mathcal{L}}\,\left[\bar{\psi}_c^C(Q,a,b) - P\right] \tag{2.116}$$

$$\dot{P} = \frac{1}{2SB^2\mathcal{L}}\,\left[Q - Q_T(P)\right] \tag{2.117}$$

whereas the dynamics of the flow nonuniformity are described by

$$\dot{a} = \frac{1}{(m+\mu)}\left[\frac{S}{2}\,\bar{\psi}_c^{Cc}(Q,a,b,X) \;-\; \lambda b\right] \tag{2.118}$$

$$\dot{b} = \frac{1}{(m+\mu)}\left[\frac{S}{2}\,\bar{\psi}_c^{Cs}(Q,a,b,Y) \;+\; \lambda a\right] \tag{2.119}$$

[8]This is so because the control surfaces through which momentum flux enters and exits each stage is in the XY plane; the axial flow coefficient is constant in Z; and, the control surface upon which the pressure acts is parallel to the Z-axis.

in Cartesian form, and

$$\dot{A} = \frac{1}{(m+\mu)}\left[\frac{S}{2}\,\bar{\psi}_c^{pc}(Q, A, \eta, r, \Theta)\right] \tag{2.120}$$

$$\dot{\eta} = \frac{1}{(m+\mu)}\left[\lambda + \frac{S}{2A}\,\bar{\psi}_c^{ps}(\eta, r, \Theta)\right] \tag{2.121}$$

in polar form. We note here that the surge-like dynamics are coupled to the rotordynamics only indirectly through the flow nonuniformity.

Integrated Characteristics. These expressions are given by Eqs. (2.101) and (2.102) and are listed here again for convenience. The Cartesian expressions are given by

$$\bar{\psi}_c^C = \psi_{c0} + 1 + 3\,(Q-0.5) - 4\,(Q-0.5)^3 - 6(a^2+b^2)\,(Q-0.5) \tag{2.122}$$

$$\bar{\psi}_c^{Cc} = -3a\left[4Q(Q-1) + (a^2+b^2)\right] + \psi_{c\varepsilon}X \tag{2.123}$$

$$\bar{\psi}_c^{Cs} = -3b\left[4Q(Q-1) + (a^2+b^2)\right] + \psi_{c\varepsilon}Y \tag{2.124}$$

whereas the polar expressions are given by

$$\bar{\psi}_c^{p} = \psi_{c0} + 1 + 3\,(Q-0.5) - 4\,(Q-0.5)^3 - 6A^2\,(Q-0.5) \tag{2.125}$$

$$\bar{\psi}_c^{pc} = -3A\left[4Q(Q-1) + A^2\right] + \psi_{c\varepsilon} r\cos(\Theta - \eta) \tag{2.126}$$

$$\bar{\psi}_c^{ps} = \psi_{c\varepsilon} r\sin(\Theta - \eta) \tag{2.127}$$

The throttle characteristic is given by

$$Q_T(P) = \gamma\sqrt{P} \tag{2.128}$$

Rotordynamic Model. For the baseline model, we assume any gravity force to be in the negative Y direction. The X and Y components of Eq. (2.68) can then be

written in Cartesian form as

$$\ddot{X} + 2\zeta\nu\dot{X} = -\nu^2 X - \varpi X^3 + e\cos\xi + \bar{f}\cos(\nu^{ha}\xi) + \chi(F_X^{ae})_i \tag{2.129}$$

$$\ddot{Y} + 2\sigma^{da}\zeta\nu\dot{Y} = -\sigma^{st}\nu^2 Y - \sigma^{ns}\varpi Y^3 + e\sin\xi - G_Y + \sigma^{ha}\bar{f}\sin(\nu^{ha}\xi) + \chi(F_Y^{ae})_i \tag{2.130}$$

In the case of symmetric damping, stiffness, and harmonic forces, the second equation can be easily rewritten after setting $\sigma^{da} = \sigma^{st} = \sigma^{ns} = \sigma^{ha} = 1$.

These can be expressed in polar form as

$$\begin{aligned}
\ddot{r} - r\dot{\Theta}^2 + \left[2\zeta\nu(\cos^2\Theta + \sigma^{da}\sin^2\Theta)\right]\dot{r} + (\sigma^{da} - 1)\left[2\zeta\nu\cos\Theta\sin\Theta\right]\dot{\Theta} = \\
- \left[\cos^2\Theta + \sigma^{st}\sin^2\Theta\right]\nu^2 r - \left[\cos^4\Theta + \sigma^{ns}\sin^4\Theta\right]\varpi r^3 + e\ \cos(\Theta - \xi) \\
+ \bar{f}\left[\cos\Theta\cos\nu^{ha}\xi + \sigma^{ha}\sin\Theta\sin\nu^{ha}\xi\right] - G_Y\sin\Theta + \chi(F_r^{ae})_i
\end{aligned} \tag{2.131}$$

$$\begin{aligned}
r\ddot{\Theta} + 2\dot{r}\dot{\Theta} + (\sigma^{da} - 1)\left[\cos\Theta\sin\Theta\right](2\zeta\nu)\dot{r} + \left[1 + (\sigma^{da} - 1)\cos^2\Theta\right](2\zeta\nu)r\dot{\Theta} = \\
- (\sigma^{st} - 1)[\cos\Theta\sin\Theta]\nu^2 r + \left[\cos^2\Theta - \sigma^{ns}\sin^2\Theta\right](\cos\Theta\sin\Theta)\varpi r^3 \\
- e\ \sin(\Theta - \xi) - \bar{f}\left[\sin\Theta\cos\nu^{ha}\xi - \sigma^{ha}\cos\Theta\sin\nu^{ha}\xi\right] \\
- G_Y\cos\Theta + \chi(F_\Theta^{ae})_i
\end{aligned} \tag{2.132}$$

It can be seen that the polar form is greatly simplified in the case of symmetric damping, stiffness, and harmonic forces. In such a case, these equations reduce to

$$\begin{aligned}
\ddot{r} - r\dot{\Theta}^2 + 2\zeta\nu\dot{r} = -\nu^2 r - \left[\cos^4\Theta + \sin^4\Theta\right]\varpi r^3 + e\ \cos(\Theta - \xi) \\
+ \bar{f}\cos(\Theta - \nu^{ha}\xi) - G_Y\sin\Theta + \chi(F_r^{ae})_i
\end{aligned} \tag{2.133}$$

$$\begin{aligned}
r\ddot{\Theta} + 2\dot{r}\dot{\Theta} + 2\zeta\nu r\dot{\Theta} = \left[2\cos^2\Theta - 1\right](\cos\Theta\sin\Theta)\varpi r^3 - e\ \sin(\Theta - \xi) \\
- \bar{f}\sin(\Theta - \nu^{ha}\xi) - G_Y\cos\Theta + \chi(F_\Theta^{ae})_i
\end{aligned} \tag{2.134}$$

Inspection of the two versions of the polar equations indicates that the presence of parameter asymmetry can introduce additional coupling between the tangential and radial motions of the rotor, and thus may alter the overall rotordynamic stability.

Aerodynamic Forces. The aerodynamic forces are given by the following expressions

$$(F^{ae})_i = (F^{tu})_i + (F^{pr})_i + (F^{un})_i \tag{2.135}$$

where the turning force contribution is given by

$$(F_X^{tu})_i = \frac{1}{4}\chi^{tu}\left\{b\left(\tau_{c1} + 2\tau_{c2}\,Q + 3\tau_{c3}\left[Q^2 + \frac{1}{4}(a^2+b^2)\right]\right) + \tau_{c\varepsilon}Y\right\} \tag{2.136}$$

$$(F_Y^{tu})_i = -\frac{1}{4}\chi^{tu}\left\{a\left(\tau_{c1} + 2\tau_{c2}\,Q + 3\tau_{c3}\left[Q^2 + \frac{1}{4}(a^2+b^2)\right]\right) + \tau_{c\varepsilon}X\right\} \tag{2.137}$$

while the pressure force contribution is given by

$$(F_X^{pr})_i = \chi^{pr}\,W^2\,Q\,a \tag{2.138}$$

$$(F_Y^{pr})_i = \chi^{pr}\,W^2\,Q\,b \tag{2.139}$$

and, finally, the unsteady force contribution is given as

$$(F_X^{un})_i = -\chi^{un}\,W\,\dot{b} \tag{2.140}$$

$$(F_Y^{un})_i = \chi^{un}\,W\,\dot{a} \tag{2.141}$$

We note that the force expressions can be written in terms of the polar variables of the flowfield, A and η, or in terms of the polar variables of the rotordynamic model, r and Θ, or a combination of these. That can be achieved using the following relations

$$a = A\cos(\eta) \qquad b = A\sin(\eta) \qquad A = \sqrt{a^2+b^2} \qquad \eta = \tan^{-1}\frac{b}{a}$$

$$\dot{a} = \dot{A}\cos\eta - A\dot{\eta}\sin\eta \qquad \dot{b} = \dot{A}\sin\eta + A\dot{\eta}\cos\eta$$

$$\dot{a}^2 + \dot{b}^2 = \dot{A}^2 + A^2\dot{\eta}^2$$

and,

$$F_r = \quad F_X \cos\Theta + F_Y \sin\Theta \qquad\qquad F_\Theta = -F_X \sin\Theta + F_Y \cos\Theta \qquad (2.142)$$

where, from here forward, the over-dot indicates differentiation with respect to nondimensional time ξ.

CHAPTER 3

ANALYSIS OF AERODYNAMIC FORCES

This chapter begins by introducing four prototype compression systems representative of different classes of compressors that can be adequately described by the baseline model. Using these compressors, we explore the nature of the aerodynamic forces by presenting their qualitative and quantitative features in two simplified special cases: fixed offset of the rotor and steady forced rotor whirl. In doing so, we aim to gain insight into the behavior of these forces as well as validate the model against recently published data. We also address the effect of compressor geometry and characteristics on these forces and give preliminary remarks about their role in inducing rotor whirl.

3.1 Prototype Compression Systems

We select four prototype compression systems which, in terms of the parameters of the current model, differ mainly in the compressor they contain, as described by the pressure-rise and torque characteristics (i.e., in terms of S, ψ_{c0}, $\psi_{c\varepsilon}$, $\tau_{c0}, \tau_{c1}, \tau_{c2}, \tau_{c3}$) on one hand, and the compressor geometry and inertia parameters (i.e., blade angles, N_{st}, λ and μ) on the other. Further, the difference in the rotordynamic classification (subcritical/supercritical) of these systems may also be linked to the compressor itself. For instance, although the rotors of system C1 and C2 (our first two prototype systems) are assumed to have the same spinning speed Ω, they are set up to be sub-

critical and supercritical, respectively. The reason is that system C2 has more stages, thus producing a higher pressure-rise and having a longer rotor span and therefore a smaller natural frequency, ω.

We now give a brief description of these compression systems, comment on the reason behind including each, and then list the nominal values of their main parameters in Table 3.1. Note that the values of some of the parameters given in the table (e.g., χ, ν and B) represent nominal choices or estimates that may be varied in the course of the parametric stability studies of the next chapter. Details of parameter selection and estimation are given in Appendix B.

3.1.1 Multistage Low Speed Axial Compressor, C1

System C1 represents a typical low-speed, *low* pressure-rise compression system with a *subcritical* rotor (i.e., $\nu > 1$). The compressor in this system is based on the heavily tested and well-documented MIT 3-Stage compressor.

Figure 3-1 depicts the pressure-rise and axisymmetric torque characteristics of this compressor in terms of the variables: (ϕ, ψ_c') and their rescaled counterparts (q, ψ_c) for the pressure rise, and $(q, (\tau_c)_i)$ for the torque. These characteristics are based mainly on detailed measurements which were originally reported by Eastland [17]. Other comprehensive description of such measurements, together with compressor geometry, parameters and configuration details, were given by Gamache [26] and more recently by Van Schalkwyk [76]. It may be helpful to refer to Figure 2-6 and relate the parameters describing the cubic pressure-rise characteristic (i.e., H, W, ψ_{c0} and $\psi_{c\varepsilon}$) to those shown here. Also shown in the figure is the exit flow angle of the rotor blade row, $\beta_{r(i)}^{out}$, corresponding to the chosen torque characteristic as calculated from Eq. (2.104). It can be seen that the deviation is only a few degrees at design point (which we choose to be at $Q = 1.2$, giving a 20% stall margin), but increases as we move away from the design point in either direction. Further, the exit flow angle is slightly more than 90 degrees in the reversed flow regime, which is qualitatively

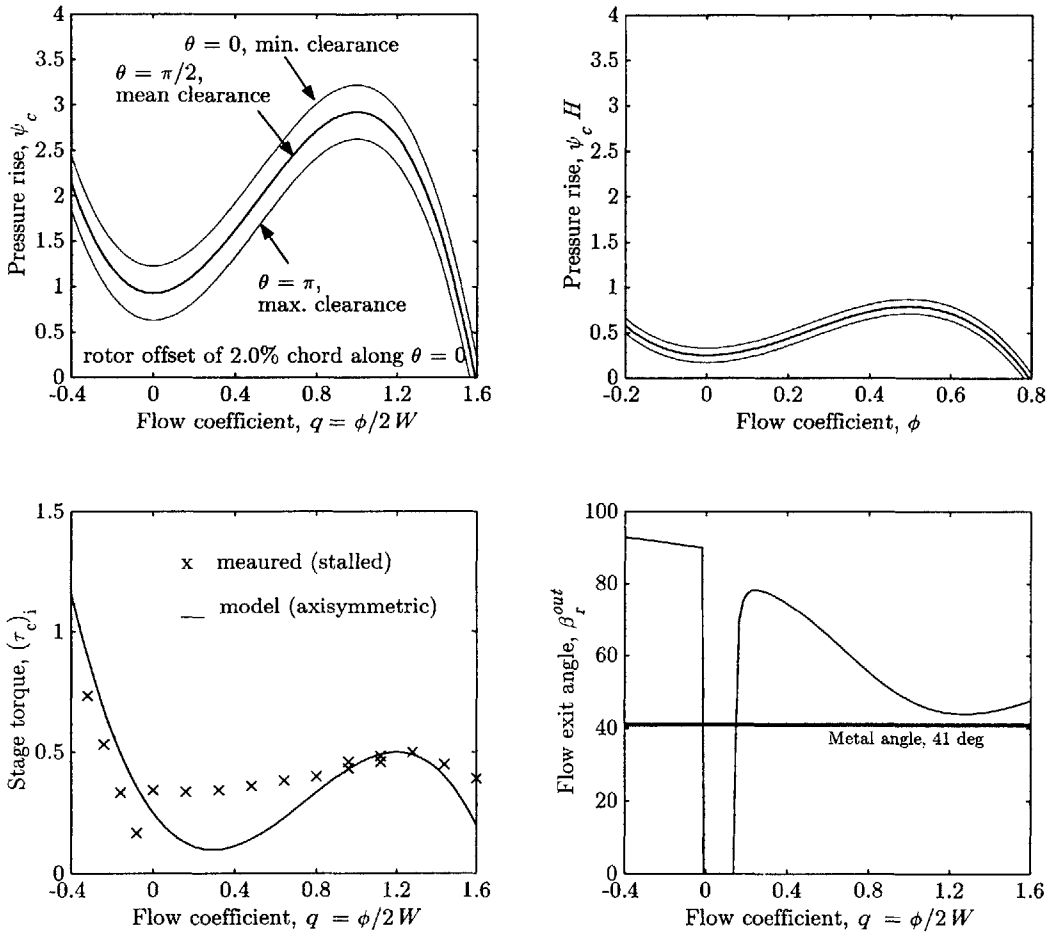

Figure 3-1: Pressure-rise and torque characteristics for C1.

consistent with measurements such as those given by Lavrich [48, e.g., Figure 5.18]. The range of flow coefficient ($0.0 < q < 0.2$) in which the angle prediction is not realistic is ignored on the basis of being very small and away from typical stable and even stalled operating points. In addition, this angle does not appear explicitly in the formulation of the model; only the torque characteristic does.

3.1.2 Multistage High Pressure Ratio Compressor, C2

System C2 represents a low-speed, *high* pressure-rise compression system with a *supercritical* rotor (i.e., $\nu < 1$). This hypothetical compressor is thought of as being the same as the MIT 3-stage compressor, C1, except with more stages stacked together.

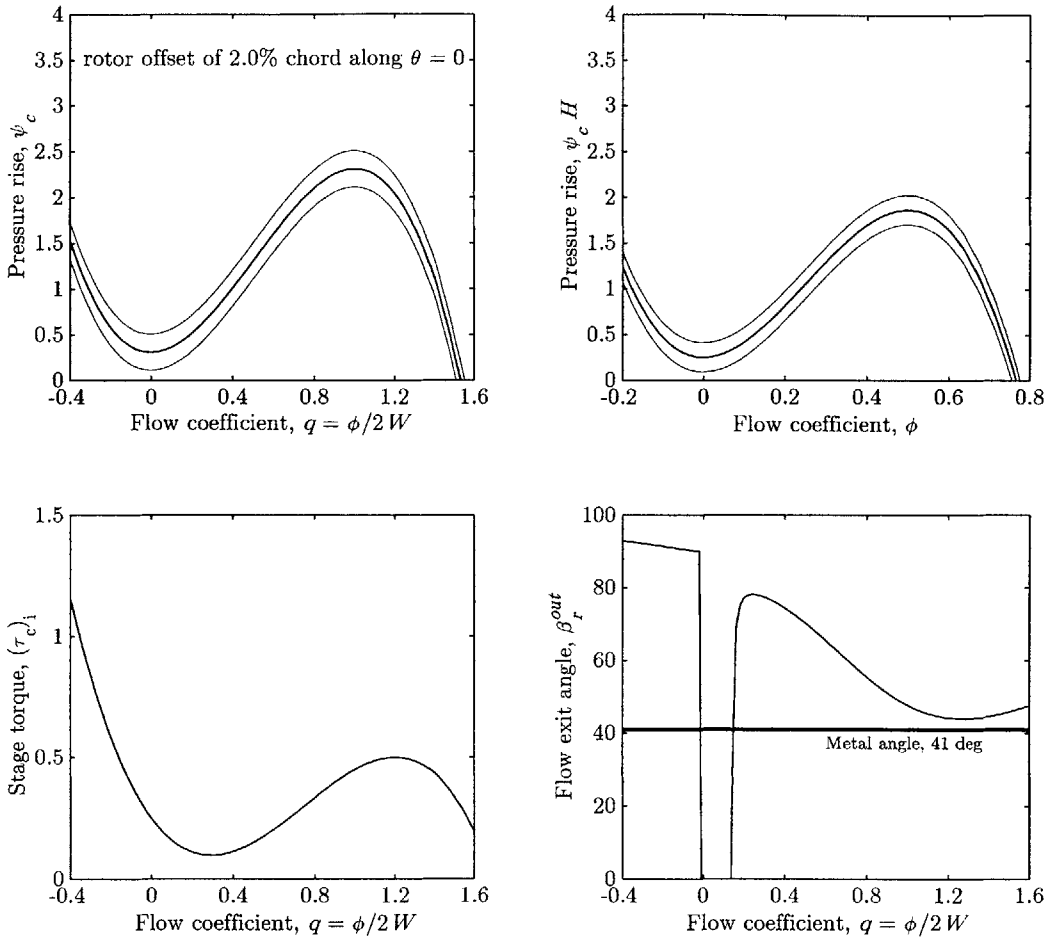

Figure 3-2: Pressure-rise and torque characteristics for C2.

We thus assume a 9-stage compressor for which S, λ and μ are three times those of C1. The effective total duct length, $\mathcal{L}$ also increases (as a result of the increase in μ) together with the rotor axial span which is now roughly three times as long (due to the additional stages). Everything else remains the same. The inclusion of this compressor is motivated by the findings of Graf et al. [30] who suggested that the higher curvature of the compressor pressure-rise characteristic can exacerbate the destabilizing effect of tip-clearance asymmetry. In addition, the high pressure-rise compressor and the supercritical rotor make this system a closer representation of a modern compressor. The pressure-rise and torque characteristics for this compressor are shown in Figure 3-2.

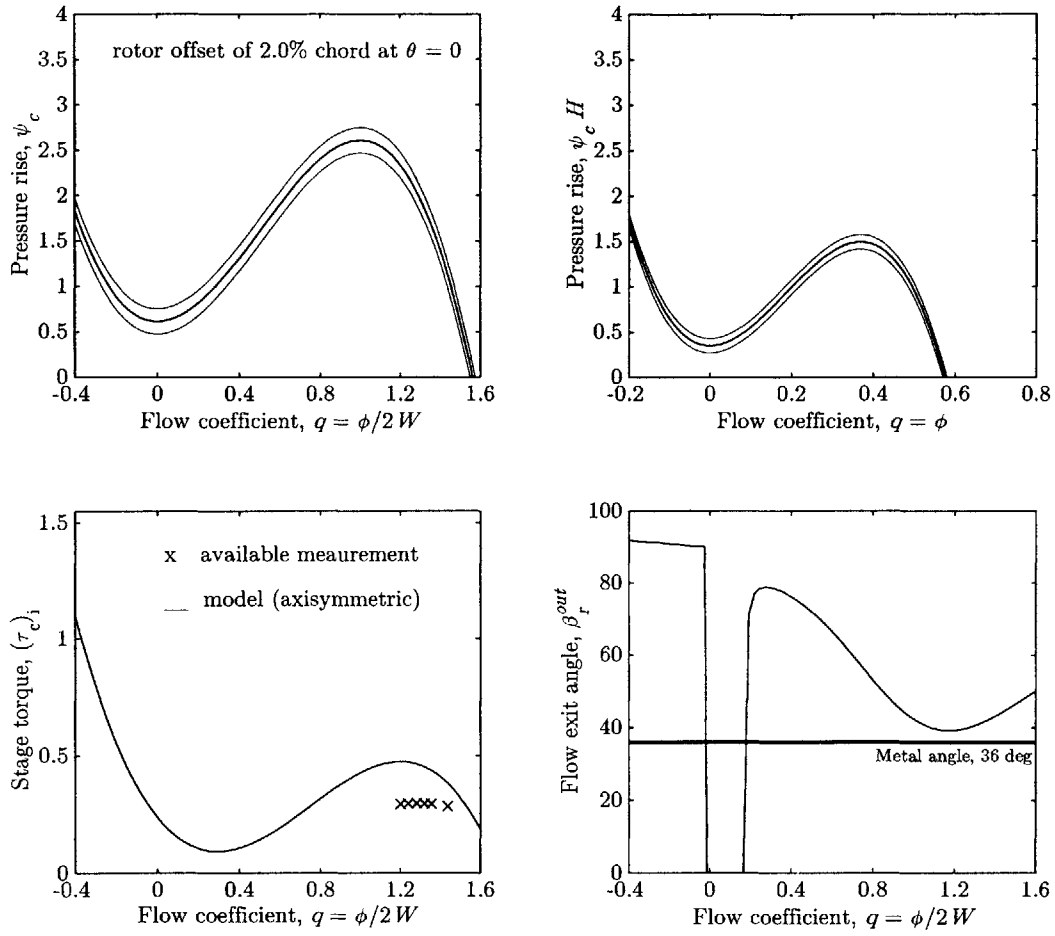

Figure 3-3: Pressure-rise and torque characteristics for C3.

3.1.3 GE 4-Stage Low Speed Research Compressor, C3

Although the compressor in system C3 does not represent a different category, it is introduced for the purpose of validating aerodynamic force calculations to be presented later in the chapter. The comparison is against experimental and numerical data taken in the GE Low Speed Research Compressor (LSRC). In these experiments, detailed measurements were taken of flow quantities within a blade passage under different values of fixed shaft offset, from which the aerodynamic forces were deduced (see Storace et al. [73] and Ehrich et al. [22]). A brief review of this work was given in Section 1.2.2.

The pressure-rise and torque characteristics for this compressor are shown in

Figure 3-3, while other available and assumed parameters are given in Tables 3.1. Note that the available torque measurement shown in the figure is clearly different from the model characteristic. Attempting to match the torque data produced an unrealistically large deviation in the flow exit angle. A more consistent value of torque was therefore used.

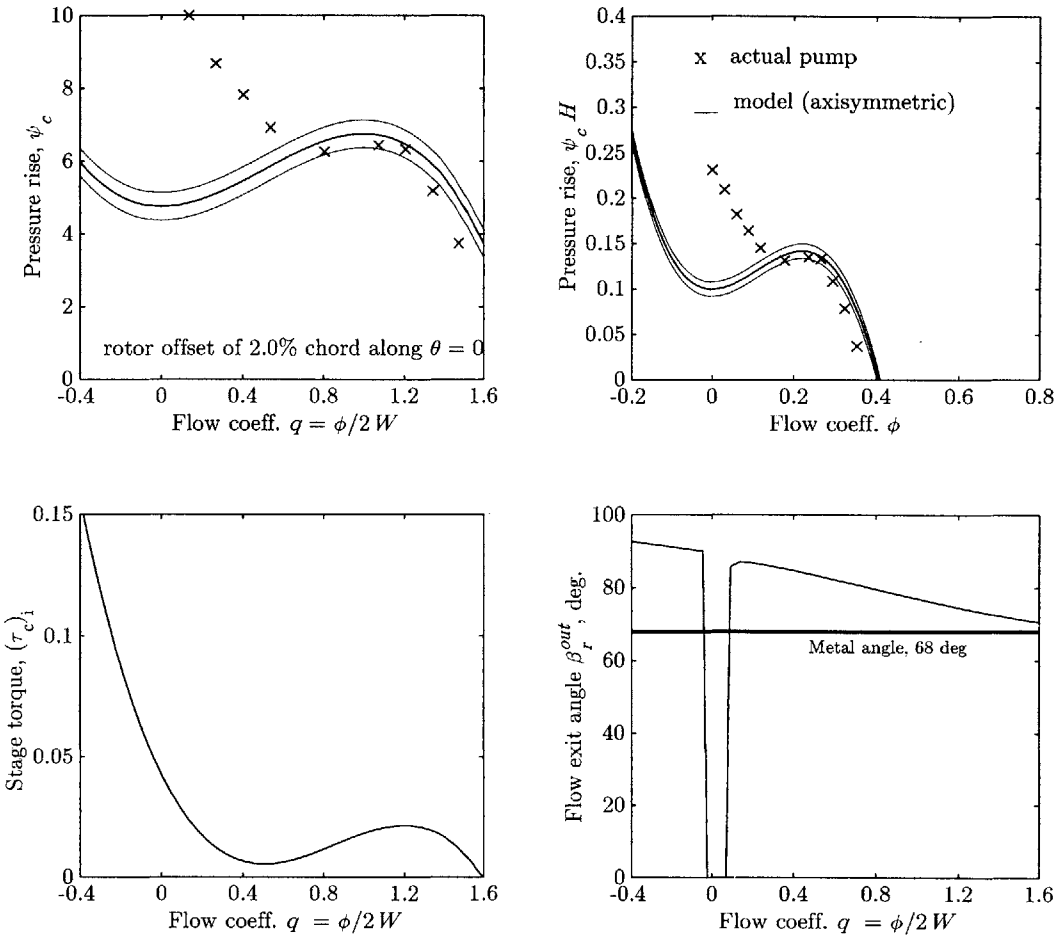

Figure 3-4: Pressure-rise and torque characteristics for C4 (Note the difference in scale).

3.1.4 Axial-Flow Liquid Pump, C4

As discussed in Section 2.2.4, the main aerodynamic-rotordynamic coupling parameter, χ, is essentially proportional to the ratio of two densities: that of the fluid being pumped and that of the rotor structural material (i.e., $\chi \sim \rho/\rho_s$). Therefore, χ is in general expected to be small for gas compressors, $\chi_{gas} \sim 10^{-5}$ to 10^{-4}. On the other

hand, in an axial liquid pump, χ is about three orders of magnitude higher and, as a result, the coupling may be more pronounced. Axial liquid pumps thus represent a typical application in which high values of χ are realistic.

We therefore consider a fourth compression system consisting of a hypothetical axial liquid pump, for which the Moore-Greitzer model may still provide a reasonable approximation. To that end, we recognize two important differences between a liquid pumping system and a gas compression system. The first difference lies in the pumping/compression device itself while the second difference has to do with the source of fluid compliance in the system.

Typical axial-flow liquid pumps are usually of low hub-to-tip ratio and have a single blade row that carries only a few large-sized blades, whereas axial compressors typically have more stages with a larger number of small-sized blades. These differences give rise to a few difficulties regarding the use of the Moore-Greitzer model and its assumptions to represent an axial liquid pump. First, an important assumption of the Moore-Greitzer model (which was essentially developed with gas compressors in mind) requires that the wavelength of circumferential disturbances be long enough compared to the blade pitch (see Longley [51] for a precise review of these assumptions). Second, the assumption of high hub-to-tip ratio allows three-dimensional effects to be neglected and a two-dimensional flow description to suffice. To overcome these modeling difficulties, we base our hypothetical system on a pump which has a relatively large number of blades and a high hub-to-tip ratio. Such a pump was used by Murai et al. [58, 59] to study cavitation and rotating stall-like instabilities[1]. This research axial pump is configured with 18 blades and has a hub-to-tip ratio of 0.7. Further, in contrast to gas compression systems which have have compressible gas in their plenums, the incompressibility of the liquid in this system results in a very small B-parameter.

We finally note that axial liquid pumps are generally characterized by relatively

[1]The performance characteristic and the main results of the Murai's studies are summarized in Brennen [5].

very large flow rates and very low heads. As can be seen in Figure 3-4, this is captured by the small value of the characteristic aspect ratio S and the large value of ψ_{c0} to account for most of the pressure-rise. As a result of the small pressure rise, most figures referring to this compression system will differ in scale as will be pointed out in the corresponding caption. A reasonable match between the model and typical measured pump characteristic is achieved over the flow range that matters the most, i.e., $0.8 < q < 1.3$, where $q < 0.8$ is not likely to be encountered because of the very small B).

Param.	C1	C2	C3	C4	Remarks
$\mathcal{L}$	5.53	7.55	5.38	33.54	fixed dimension
B	0.1	0.1	0.1	0.001	nominal
N_{st}	3	9	4	1	data match
H, W	0.27, 0.25	0.81, 0.25	0.57, 0.18	0.021, 0.11	data match
S	1.08	3.24	3.1	0.19	ratio of H/W
λ, μ	0.68, 1.01	2.04, 3.03	0.848, 1.56	1.38, 2.77	fixed dimension
ψ_{c0}	0.926	0.309	0.612	4.76	data match
m	2	2	2	2	see Eq. (2.18)
ν^{rs}	0.23	0.41	0.24	0.29	fixed ($\nu^{rs} = \frac{\lambda}{m+\mu}$)
ζ	0.05	0.05	0.05	0.05	nominal
ν	1.76	0.227	0.687	3.50	nominal
ϖ	$(7.6)10^{+3}$	$(1.267)10^{+2}$	$(1.655)10^{+3}$	$(9.24)10^{+3}$	nominal
G_Y	$(3.4)10^{-3}$	$(3.4)10^{-3}$	$(1.46)10^{-2}$	$(1.87)10^{-2}$	constant
all σ's	1	1	1	1	nominal
$\psi_{c\varepsilon}$	14.82	9.88	7.00	19.05	data match
$\tau_{c\varepsilon}$	0	0	0	0	assumption
χ	$(7.83)10^{-5}$	$(7.83)10^{-5}$	$(4.81)10^{-4}$	$(2.71)10^{-2}$	nominal estimate
χ^{tu}	54.74	54.74	85.39	13.04	fixed geometry
χ^{pr}	98.89	98.89	91.00	11.77	fixed geometry
χ^{un}	5.9	5.9	8.91	5.80	fixed geometry
ν/ν^{rs}	7.78	0.559	2.88	12.05	nominal ($\frac{\nu}{\nu^{rs}} = \frac{\omega}{\omega^{rs}}$)
$\psi_{c\varepsilon}\chi$	$(1.16)10^{-3}$	$(7.73)10^{-4}$	$(3.37)10^{-3}$	$(5.16)10^{-1}$	nominal

Table 3.1: Nominal and fixed values of nondimensional parameters for different prototype compression systems.

3.2 Qualitative Relationship Between Aerodynamic Forces and Flowfield Nonuniformity

The aerodynamic force expressions derived in the last chapter indicate that these forces are the direct result of the flowfield nonuniformity, and that they depend on the operating point and compressor characteristic. Further, the compact form of these expressions allow for the establishment of clear relations between the forces and the quantities describing the flow nonuniformity. In this section, we demonstrate these relations by giving numerical examples that are based on compressor C1. Comparison of forces in the other compressors will be given in the following section.

Turning Force

Recalling the expressions for the two components of the turning force, F_X^{tu} and F_Y^{tu}, given by Eqs. (2.136) and (2.137), and taking $\tau_{c\varepsilon} = 0$ from now on as the baseline case, we can write expressions for the amplitude and phase of the turning force as follows

$$F^{tu} = \sqrt{(F_X^{tu})^2 + (F_Y^{tu})^2} = \frac{1}{4}\chi^{tu} A \bar{F}_c^{tu} \tag{3.1}$$

$$= \frac{1}{4}\chi^{tu} A \left[\tau_{c1} + 2\tau_{c2}\, Q + 3\tau_{c3}\left(Q^2 + \frac{1}{4}A^2\right)\right] \tag{3.2}$$

and,

$$\eta^{tu} = -\tan^{-1}\frac{a}{b} = \eta \pm 90 \tag{3.3}$$

The phase relation above indicates that, to first harmonic approximation of the flowfield, the line of action of the turning force contribution is perpendicular to the peak of the flow nonuniformity, and not to the tip clearance asymmetry as it is traditionally assumed. The amplitude of the turning force is a somewhat complicated expression that is cubic in A and quadratic in Q.

To illustrate the features of the above relations, we consider compressor C1 as an example, and assume a flowfield nonuniformity of amplitude A and some fixed phase η, say 30 degrees. Figure 3-5 shows a plot of the X and Y components of the turning force, together with its amplitude F^{tu}, and phase difference, $\eta^{tu} - \eta$, as a function of mean flow coefficient Q and for different values of flow nonuniformity amplitude A. It can be seen that for small values of A, and as the mean flow coefficient Q is decreased, the turning force reverses direction twice along the line perpendicular to A. That is, the phase difference $\eta^{tu} - \eta$ changes from 90 to -90 and then to 90 degrees again. However, for a nonuniformity of large amplitude, e.g., $A = 1.0$, the turning force maintains the same direction at $\eta^{tu} - \eta = 90$ for all Q. Small values of A are representative of flow nonuniformities that are the result of a rotor offset, whereas the large value of $A = 1$ represents a nonuniformity such as rotating stall.

Pressure Force

Using the X and Y components of the pressure force as given in Eqs. (2.138) and (2.139), an expressions for the amplitude and phase of the pressure force contribution can be written as follows

$$F^{pr} = \chi^{pr} W^2 Q A \tag{3.4}$$

and,

$$\eta^{pr} = \tan^{-1} \frac{b}{a} = \eta \pm 0, 180 \tag{3.5}$$

This indicates that the pressure force is always aligned with the flow nonuniformity. This is consistent with the simple Bernoulli relation between flow pressure and velocity, which requires the point on the circumference passing the minimum flow to have the maximum pressure. It should also be noted that, unlike the turning force, the pressure force is a simple function which is linear in both A and Q. Figure 3-6 shows a plot of the amplitude and phase difference of the pressure force and it X and Y

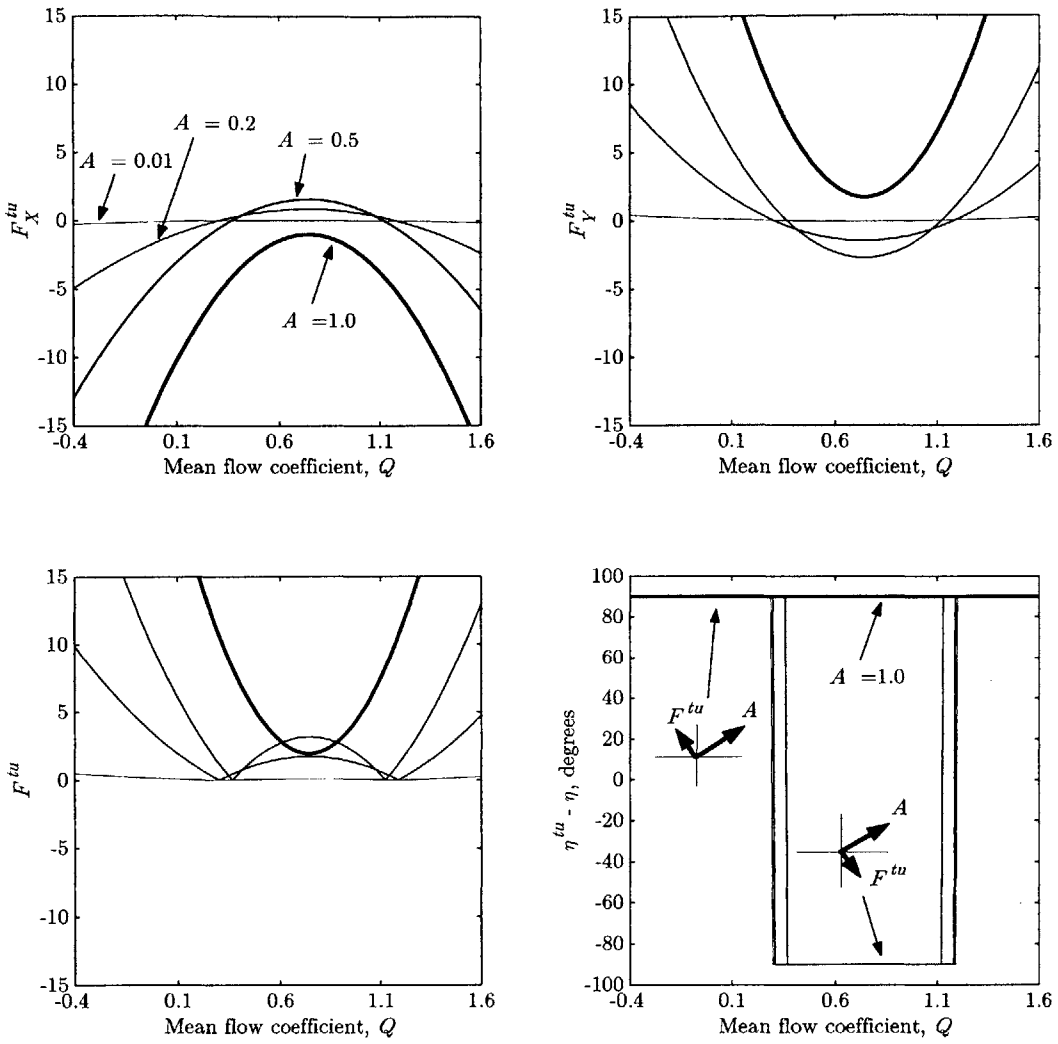

Figure 3-5: Amplitude of turning force F^{tu} for different values of flow nonuniformity amplitude, for system C1.

components, as a function of Q and for different values of A.

Unsteady Force

Similarly, using the X and Y components of the unsteady force as given in Eqs. (2.140) and (2.141), expressions for the amplitude and phase of this force contribution can be written as follows

$$F^{un} = \chi^{un} W \sqrt{\dot{A}^2 + A^2 \dot{\eta}^2} \tag{3.6}$$

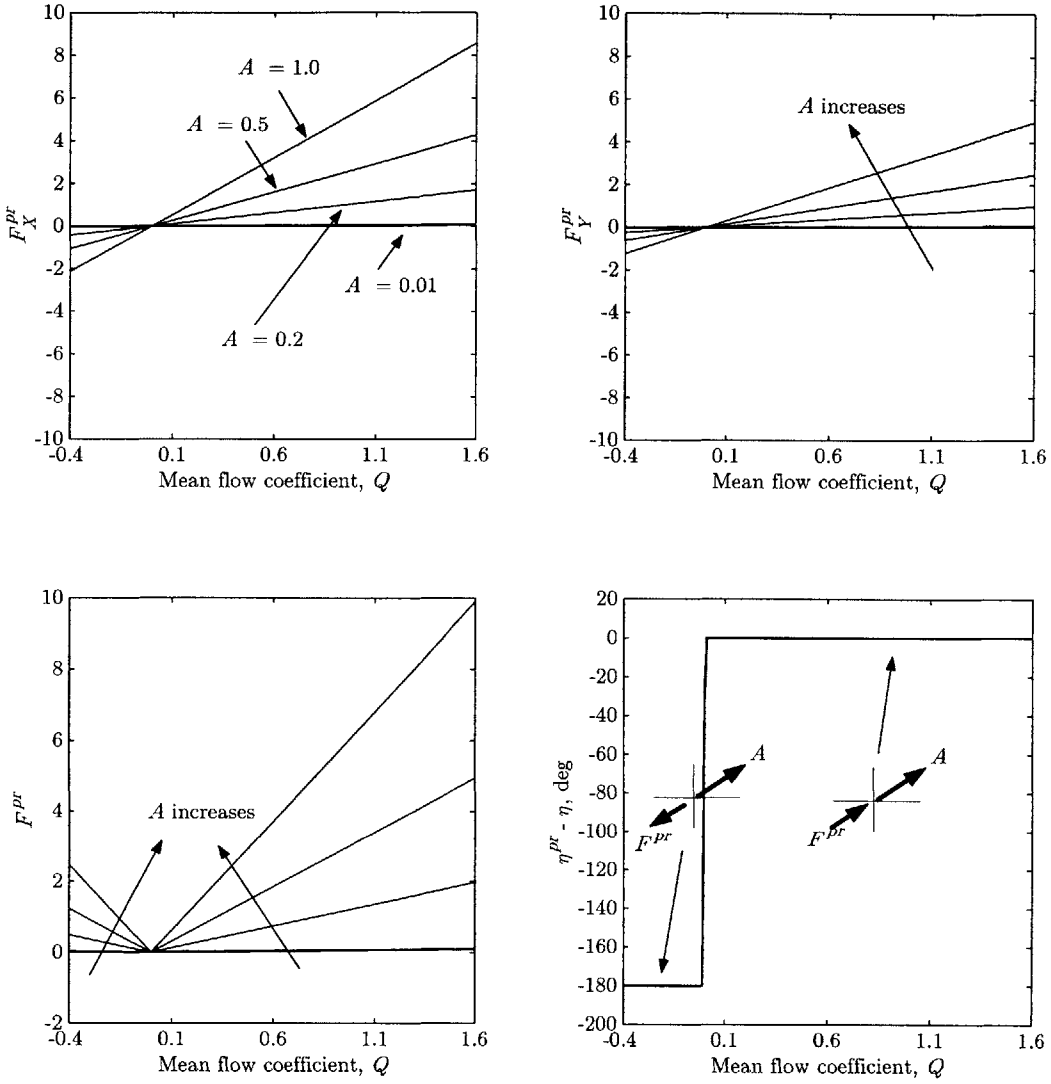

Figure 3-6: Amplitude of pressure force F^{pr} for different values of flow nonuniformity amplitude, for system C1.

and,

$$\eta^{un} = -\tan^{-1}\frac{\dot{a}}{\dot{b}} = -\tan^{-1}\frac{\dot{A}\cos\eta - A\dot{\eta}\sin\eta}{\dot{A}\sin\eta + A\dot{\eta}\cos\eta} \tag{3.7}$$

The relations of the unsteady force are more complicated than the other two. But some insight can be gained by considering the special case of pure rotating stall in which the flow nonuniformity has a constant amplitude, $A = A^{rs}$ (i.e., $\dot{A} = 0$), and a constant rate of rotation, $\dot{\eta} = \nu^{rs}$. In such a case, the amplitude and phase of the unsteady force reduce to

$$(F^{un})^{rs} = \chi^{un} W A^{rs} \nu^{rs} \qquad \text{and} \qquad (\eta^{un})^{rs} = \tan^{-1}\frac{\sin\eta}{\cos\eta} = \eta \pm 0, 180 \tag{3.8}$$

which indicates that the unsteady force during rotating stall is also aligned with the flow nonuniformity (and hence rotating at the same frequency) and that the amplitude is a simple function that is linear in both A and ν^{rs}, but is independent of Q.

Figure 3-7 is a plot of the above results showing the amplitude and phase difference of the unsteady force as a function of A and for different values of ν^{rs}. We note that the amplitude of the unsteady force during rotating stall (i.e., $A \sim 1$) is in general very small compared to the turning and pressure force contributions at similar value of A.

Figure 3-8 is a schematic which summarizes the phase relations between the three force contributions and flowfield nonuniformity described above.

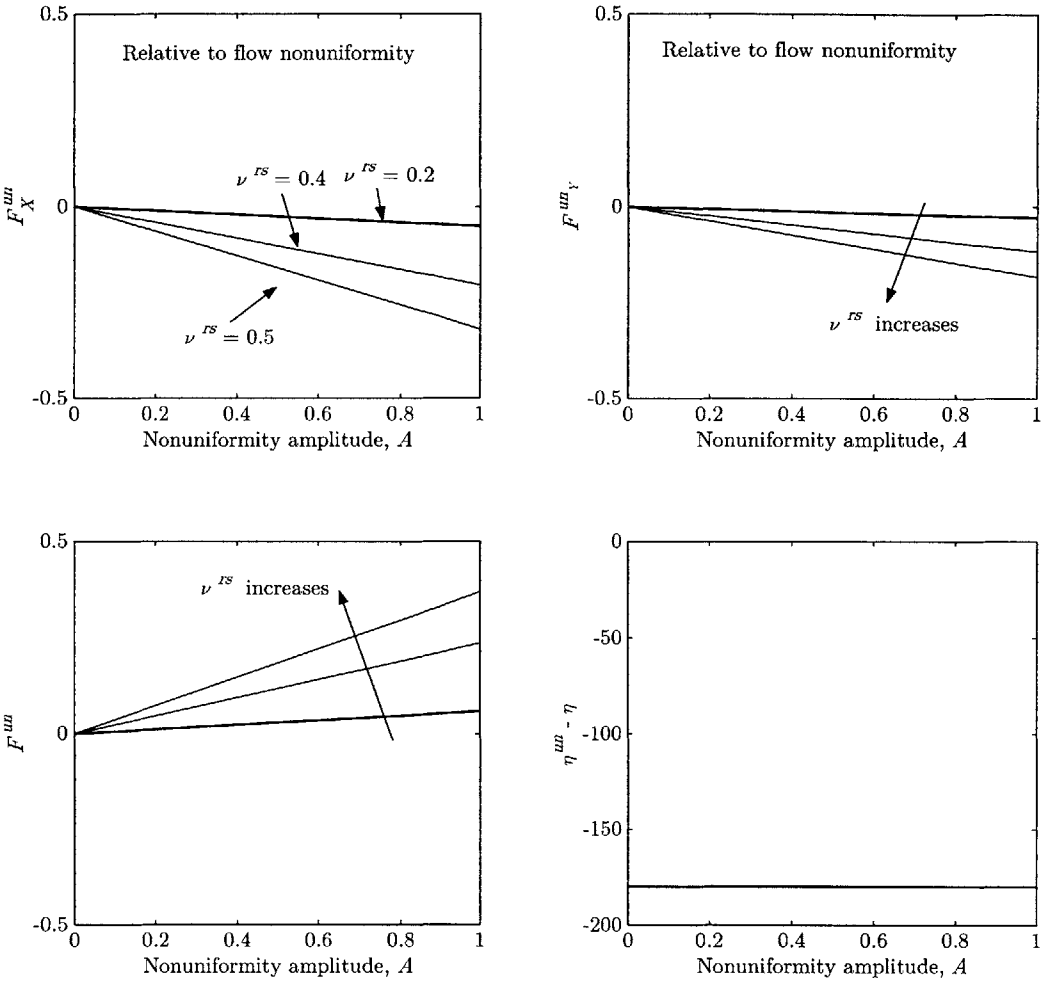

Figure 3-7: Amplitude of unsteady force F^{un} for different values of flow nonuniformity amplitude, for system C1.

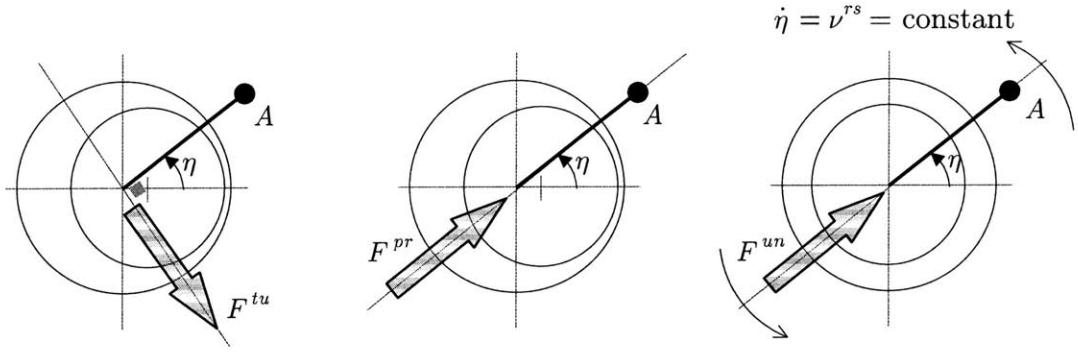

Figure 3-8: Schematic of the phase relationship between the three aerodynamic forces and flow nonuniformity.

3.3 Calculation of Aerodynamic Forces in Simplified Cases: Fixed Rotor Offset and Forced Rotor Whirl

The relations described in the previous section do not take into account the link between the tip-clearance asymmetry and the flowfield nonuniformity it generates. They simply give the aerodynamic forces resulting from a given, arbitrary flow nonuniformity without specifying how that nonuniformity is produced. As such, these relations represent an insightful view of the forces which should carry over to more complicated situations.

A more realistic picture can be obtained by realizing that the flow nonuniformity as represented by (A, η) is not arbitrary, but is rather the result of a tip-clearance asymmetry. We assume that this asymmetry is produced by an offset of the rotor within the casing. We therefore choose a static rotor offset, solve the flowfield equations for (A, η) resulting from the tip clearance asymmetry, and then calculate the resulting forces. In doing so, we quantify the relationship between the aerodynamic

forces and a given, somewhat arbitrary tip-clearance asymmetry (or steady rotor deflection). To further generalize the problem without adding much more complexity, we consider a rotor which is forced to whirl within the casing at some fractional frequency, $\nu^{wh} = \omega^{wh}/\Omega$, and a fixed radial displacement r^{wh}. The special case when $\nu^{wh} = 0$ corresponds to the fixed rotor offset configuration. Although the flowfield under forced whirl is unsteady in the fixed frame XY, it is steady in the asymmetry/whirl frame X^*Y^*, Figure 3-9, and can therefore be solved with relative ease. These calculations are carried out and presented in this section for all four prototype compressors introduced earlier.

Since the rotor motion is specified, the rotordynamics do not play a role in this exercise. Nevertheless, the goal remains to give a quantitative and qualitative description of the aerodynamic forces in relatively simplified cases before the fully coupled system is considered. In addition, this exercise allows for comparing the force model predictions against experimental data obtained for a similar, fixed rotor offset configuration.

3.3.1 Transformation of Coordinate System

The first step in the analysis is to transform the dynamic equations of the flowfield to a frame of reference which is rotating with tip clearance asymmetry. This requires the following transformation of variables, (see Figure 3-9)

$$\begin{aligned} \xi^* &= \xi \\ \theta^* &= \theta - \nu^{wh}\xi \\ r^* &= r \\ \Theta^* &= \Theta - \nu^{wh}\xi \end{aligned}$$

for independent variables, and

$$A^* = A$$

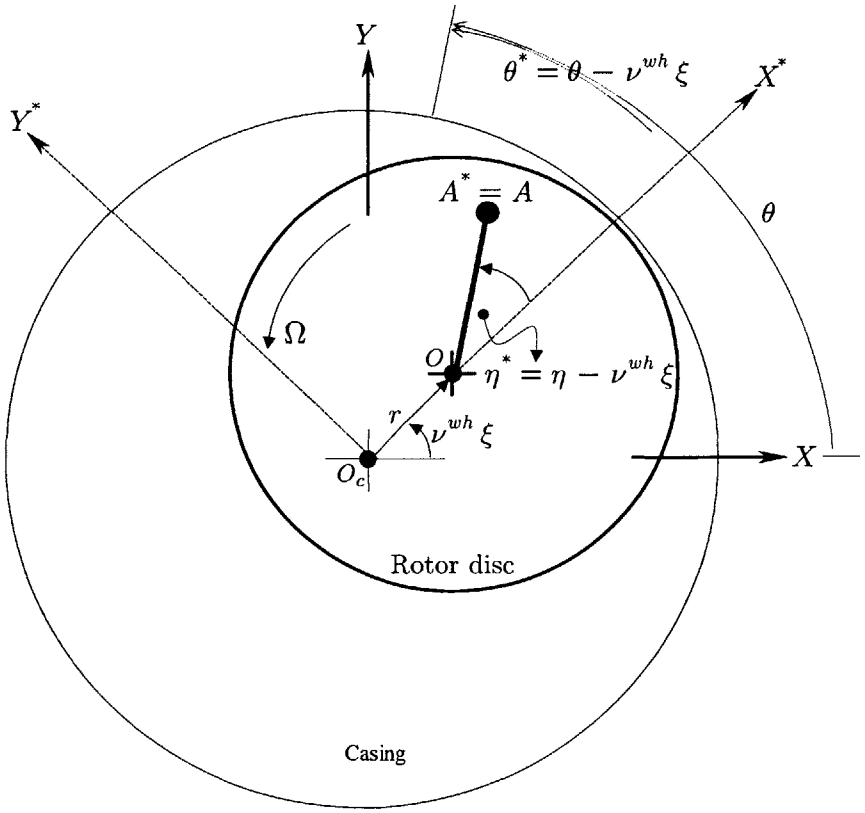

Figure 3-9: Schematic of main variables in the fixed and the whirling coordinate systems.

$$
\begin{aligned}
\eta^* &= \eta - \nu^{wh}\xi \\
q^*(\xi^*, \theta^*) &= q(\xi, \theta - \nu^{wh}\xi) \\
Q^* &= Q \\
P^* &= P - \frac{1}{2H}(\nu^{wh})^2
\end{aligned}
$$

for dependent variables, where the asterisk indicates variables in the whirling frame X^*Y^*. The spatial and temporal derivatives in the rotating frame are given by

$$
\frac{\partial}{\partial \theta^*} = \frac{\partial}{\partial \theta} \qquad \text{and} \qquad \frac{\partial}{\partial \xi^*} = \frac{\partial}{\partial \xi} + \nu^{wh}\frac{\partial}{\partial \theta} \tag{3.9}
$$

respectively. To simplify the notation, we drop the asterisk from the variables Q, A and r since they are the same in both fixed and rotating frames.

The flowfield equations in the rotating frame can now be derived using the same procedure outlined in Chapter 2. The resulting equations are as follows

$$
\dot{Q} = \frac{S}{2\mathcal{L}}\left[\bar{\psi}_c^p(Q, A, \eta^*) - (P^* + \frac{1}{2H}\nu^{wh})\right] \tag{3.10}
$$

$$
\dot{P^*} = \frac{1}{2SB^2\mathcal{L}}\left[Q - Q_T(P^*)\right] \tag{3.11}
$$

and

$$
\dot{A} = \frac{1}{(m+\mu)}\left[\frac{S}{2}\,\bar{\psi}_c^{pc}(Q, A, \eta^*, r, \Theta^*)\right] \tag{3.12}
$$

$$
\dot{\eta^*} = \frac{1}{(m+\mu)}\left[\lambda + \frac{S}{2A}\,\bar{\psi}_c^{ps}(\eta^*, r, \Theta^*)\right] - \nu^{wh} \tag{3.13}
$$

where the integrated characteristics $\bar{\psi}_c^p$, $\bar{\psi}_c^{pc}$ and $\bar{\psi}_c^{ps}$ remain the same as given before in Eqs. (2.125)–(2.127), except that they are now evaluated in terms of the new variables in the rotating frame.

3.3.2 Solution of the Steady State Equations

We now examine the steady state version of the above equations by setting their LHS to zero yielding

$$0 = \bar{\psi}_c^p(Q, A, \eta^*) - (P^* + \frac{1}{2H}\nu^{wh}) \tag{3.14}$$

$$0 = Q - \gamma\sqrt{P^* + \frac{1}{2H}\nu^{wh}} \tag{3.15}$$

$$0 = -3A\left[4Q(Q-1) + A^2\right] + \psi_{c\varepsilon} r \cos(\Theta^* - \eta^*) \tag{3.16}$$

$$0 = \frac{1}{(m+\mu)}\left[\lambda + \frac{S}{2A}\psi_{c\varepsilon} r \sin(\Theta^* - \eta^*)\right] - \nu^{wh} \tag{3.17}$$

which, in principle, must be solved simultaneously for Q, P^*, A, and η^* as a function of the parameters γ and ν^{wh}. We note however that the first two equations describing the axisymmetric flow need not be solved simultaneously with those describing the flow nonuniformity. The reason is that the latter two equations do not contain either γ or P^*. We can therefore choose the value of Q to be that of any desired operating point on the the compressor map. We may then proceed to solve the flow nonuniformity equations for A and η^*, thus obtaining all quantities needed to evaluate the expressions of the aerodynamic forces. Having solved for A and η^*, and having chosen Q, we can return to the first two equations and find the value of γ and P^* that correspond to that operating point. To further simplify the equations, we reduce the number of variables by choosing the X^*-axis to be exactly aligned with the point of minimum clearance which results in $\Theta^* = 0$, without loss of generality. In doing so, η^* is then the phase angle around the circumference between the flow nonuniformity and the rotor offset, or equivalently, the angle between the point of minimum tip-clearance and the point of maximum axial flow coefficient.

The result of the above procedure is the following equation

$$A^6 + [8Q(Q-1)]A^4 + \left[16Q^2(Q-1)^2 + \left(\frac{2}{3}\frac{[\lambda - (m+\mu)\nu^{wh}]}{S}\right)^2\right]A^2 - \left(\frac{1}{3}\psi_{c\varepsilon} r\right)^2 = 0 \tag{3.18}$$

which is sixth order in A, but only third order in A^2. After solving this cubic equation and picking the real positive root, we may obtain η^* by rewriting Eq. (3.17) as follows

$$\eta^* = \sin^{-1}\left(\frac{2A[\lambda - (m+\mu)\nu^{wh}]}{S\psi_{c\varepsilon}r}\right) \tag{3.19}$$

A few comments are in order regarding the above two equations. First, we note that r and $\psi_{c\varepsilon}$ play the same role in determining the flow nonuniformity amplitude A and the phase η^*. For instance, increasing the rotor offset r is equivalent to having higher compressor sensitivity to tip clearance $\psi_{c\varepsilon}$, either of which will increase the amplitude of the nonuniformity A. Second, there exists a critical whirling frequency, $\nu^{wh} = \lambda/(m+\mu) = \nu^{rs}$, at which the second part of the A^2 coefficient becomes zero, and at which A is maximized while the phase η^* becomes equal to zero (i.e., peak flow nonuniformity is aligned with the minimum tip clearance, see Figure 3-9). Finally, in the case of $\nu^{wh} = 0$, we note that reducing the parameter ratio λ/S has a similar (yet weaker) effect on the steady state solution. For instance, higher values of the pressure-rise characteristic parameter $S = H/W$—corresponding to steeper characteristic—would (for the same λ) increase A and reduce η^*. A look at Tabel 3.1, reveals that systems C1 and C2 have the same ratio λ/S which is smaller than that of system C3.

With A and η^* available from the equations above, the aerodynamic forces can now be evaluated at any given compressor operating point Q and any whirling frequency ν^{wh} using the expressions developed in Chapter 2 and listed in Section 2.3.3, keeping in mind that the resulting forces are now in the X^*Y^* frame instead of the XY frame. As such, the X^* component of the force will be along the line of the rotor offset and thus will represent the (positive or negative) restoring force, while the Y^* component of the force will be perpendicular to the rotor offset and thus will represent the (backward or forward) whirl-inducing force. Further, only the turning and pressure force contributions are evaluated since the unsteady force contribution is zero for the steady flow situation considered here. Finally, we note that although no stable equilibrium points are expected to exist at very low (and negative) values of

flow coefficient, Q, evaluating the above expressions in those regions may be thought of as a means of estimating the instantaneous magnitude and direction of turning and pressure force contributions that may be encountered during sever transients such as during surge.

3.3.3 Case of Fixed Rotor Offset

We now carry on to show the results of the calculations described above by first considering the simpler case of fixed rotor offset corresponding to $\nu^{wh} = 0$. The steady state flowfield equations given in Eqs. (3.18) and (3.19) reduce to

$$A^6 + [8Q(Q-1)]\,A^4 + \left[16Q^2(Q-1)^2 + \left(\frac{2}{3}\frac{\lambda}{S}\right)^2\right] A^2 - \left(\frac{1}{3}\psi_{c\varepsilon} r\right)^2 = 0 \qquad (3.20)$$

and,

$$\eta^* = \sin^{-1}\left(\frac{2A}{\psi_{c\varepsilon} r}\frac{\lambda}{S}\right) \qquad (3.21)$$

Figures 3-10 to 3-13 show the flowfield nonuniformity in terms of A and η^* and the corresponding aerodynamic forces generated as a result of a fixed rotor offset for the different compression systems. These four figures correspond to the compression systems C1, C2, C3 and C4 respectively. Further, each figure contains three rows of sub-plots: the amplitude and phase of flow nonuniformity are shown on the first row; the amplitude and phase of the aerodynamic forces on the second row; and, the X^* (restoring) and Y^* (whirl-inducing) force components on the third row. Upon examining these figures, we make the following several observations.

For a rotor offset of $r = 1.0\%$ chord (about 35% of maximum possible deflection), the flow nonuniformity amplitude A is of order 0.01 at very high mean flow coefficient Q; of order 0.05 at design flow of $Q = 1.2$; and, of order 0.1 at Q which corresponds to the peak pressure rise. The high amplitude of the nonuniformity close to the the peak of the characteristic is the result of the compressor's tendency to amplify distortions

as it operates closer to its neutral stability point. Furthermore, compressor C1 has roughly a 50% higher value of A as compared to compressor C2. This is due to the fact that the compressor's tip-clearance sensitivity parameter $\psi_{c\varepsilon}$ is also about 50% higher. Compressor C3 has the highest A at $Q = 1$ since its sensitivity parameter $\psi_{c\varepsilon}$ is very close to that of C1, but it has a higher value of the λ/S ratio, which corresponds to a larger fluid inertia in the rotor and/or a less steep compressor characteristic, both of which mean less amplification of flow nonuniformities.

The phase η^* varies with Q in approximately the same way as A. The point of maximum flow is about 10 degrees away from the minimum tip clearance point at very high Q. These two points move apart as the flow is reduced towards the peak, $Q = 1$, at which point the flow nonuniformity is 90 degrees out of phase with the tip-clearance asymmetry. Comparing the phase η^* in the three compressors C1, C2 and C3 shows that C1 and C2 have identical phase trends, while C3 has smaller η^* for all values of Q except at the peaks. The reason behind this can be seen by examining Eq. (3.21) and recalling that C1 and C2 have the same λ/S ratio, while the effect of the smaller $\psi_{c\varepsilon}$ of C2 (in the denominator) is cancelled by the smaller amplitude A (in the numerator). The physical interpretation of the phase can be linked to the fluid inertia in the rotor blade rows represented by λ. The larger this inertia is, the more the flow nonuniformity lags behind the tip-clearance asymmetry. On the other hand, a steeper characteristic (larger S) tends to counter that effect.

On the second row of sub-plots in Figures 3-10 to 3-13, we show the amplitude and phase difference $[(\eta^*)^{(F)} - \eta^*]$, where $(\eta^*)^{(F)}$ denotes $(\eta^*)^{tu}$, $(\eta^*)^{pr}$ or $(\eta^*)^{ae}$. We observe that for all three compressors C1, C2 and C3, and over a wide range of Q (the exception being $0.8 < Q < 1.2$), the turning force is the dominant contribution to the total aerodynamic force. However, within the range of $0.8 < Q < 1.2$, the two contributions are of comparable size. As for the phase of the aerodynamic forces, we note that the turning force again has the dominant effect on the phase of the total force. For all three compressors, the phase difference $(\eta^*)^{ae} - \eta^*$, is roughly 90 degrees out of phase with the flow nonuniformity over the range $-0.4 < Q < 0.4$; between

-60 and -90 degrees within $0.4 < Q < 1.2$; and, switches back to approach 90 degrees for $Q > 1.2$. The phase behavior described above indicates a strong link to the compressor torque characteristic in that the two phase jumps occur approximately at values of Q that correspond to $\frac{\partial(\tau_c)_i}{\partial Q} = 0$. This is not always the case, however, since for larger flow nonuniformities (i.e., larger A), there could be no phase jumps over the whole range of Q as shown in Figure 3-5 ($A = 1$ case).

On the third row of sub-plots we show the X^* and Y^* components of the aerodynamic forces. For the given rotor deflection, the X^* component represents the restoring force while the Y^* component represents the whirl-inducing force. As Q is varied over the operating range, both these forces are seen to change sign. In particular, for $Q < 0.4$, the X^* force component is shown to provide a restoring force that tends to oppose the rotor deflection, while for $Q \gtrsim 0.4$ it becomes in the same direction as the deflection. On the other hand, the Y^* component is shown to change sign more than once over the whole range of Q, hence providing both forward and backward whirl *tendencies* depending on the operating point. It is worth noting that the pressure contribution, which has traditionally been neglected in studying compressor and turbine whirl phenomena, may have a strong influence on the net whirl tendency of the compressor. For example, the Y^* force component sub-plot in Figure 3-10 shows that, around $Q = 1$, the pressure contribution is large enough to completely reverse the net effect from backward whirl (due to turning alone) to positive whirl.

Finally, we note that the liquid pump, C4, differs from the other three compression systems in that it exhibits smaller flow nonuniformit—owing to its very low pressure rise (i.e., very small S)—which, together with the low χ^{tu} and χ^{pr}, result in much smaller aerodynamic force, $(F^{ae})_i$), about two orders of magnitude lower than the those of the other three compressors. Nevertheless, the total aerodynamic force which appears in the dynamic equations, $F^a e = \chi(F^{ae})_i$, is still about an order of magnitude higher for C4 than for the other three because of the much larger value of the coupling parameter χ.

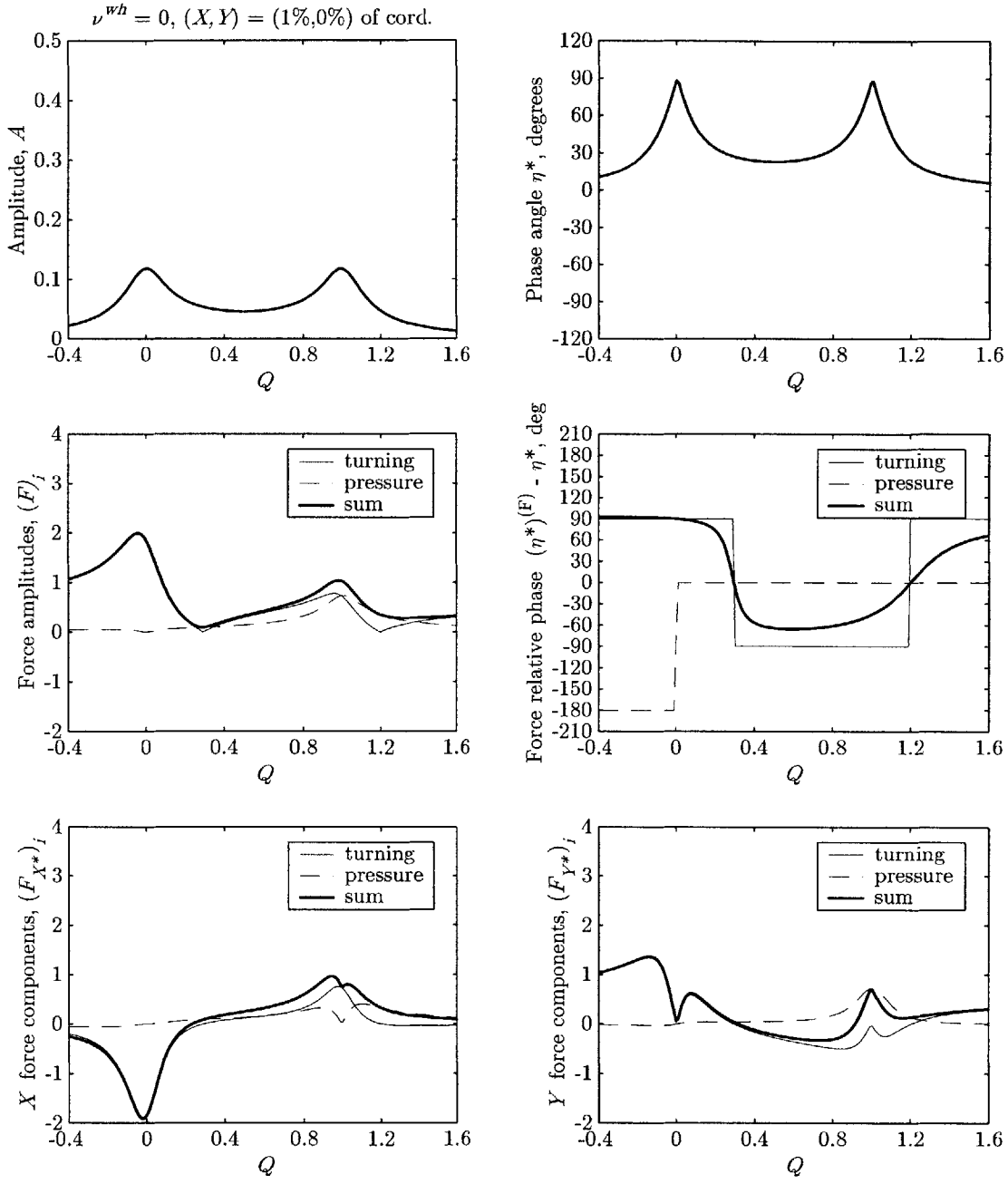

Figure 3-10: Flow nonuniformity and aerodynamic forces for fixed rotor offset as a function of operating point mean flow Q: Compressor C1, $\nu^{wh} = 0, r = 1.0\%$ chord.

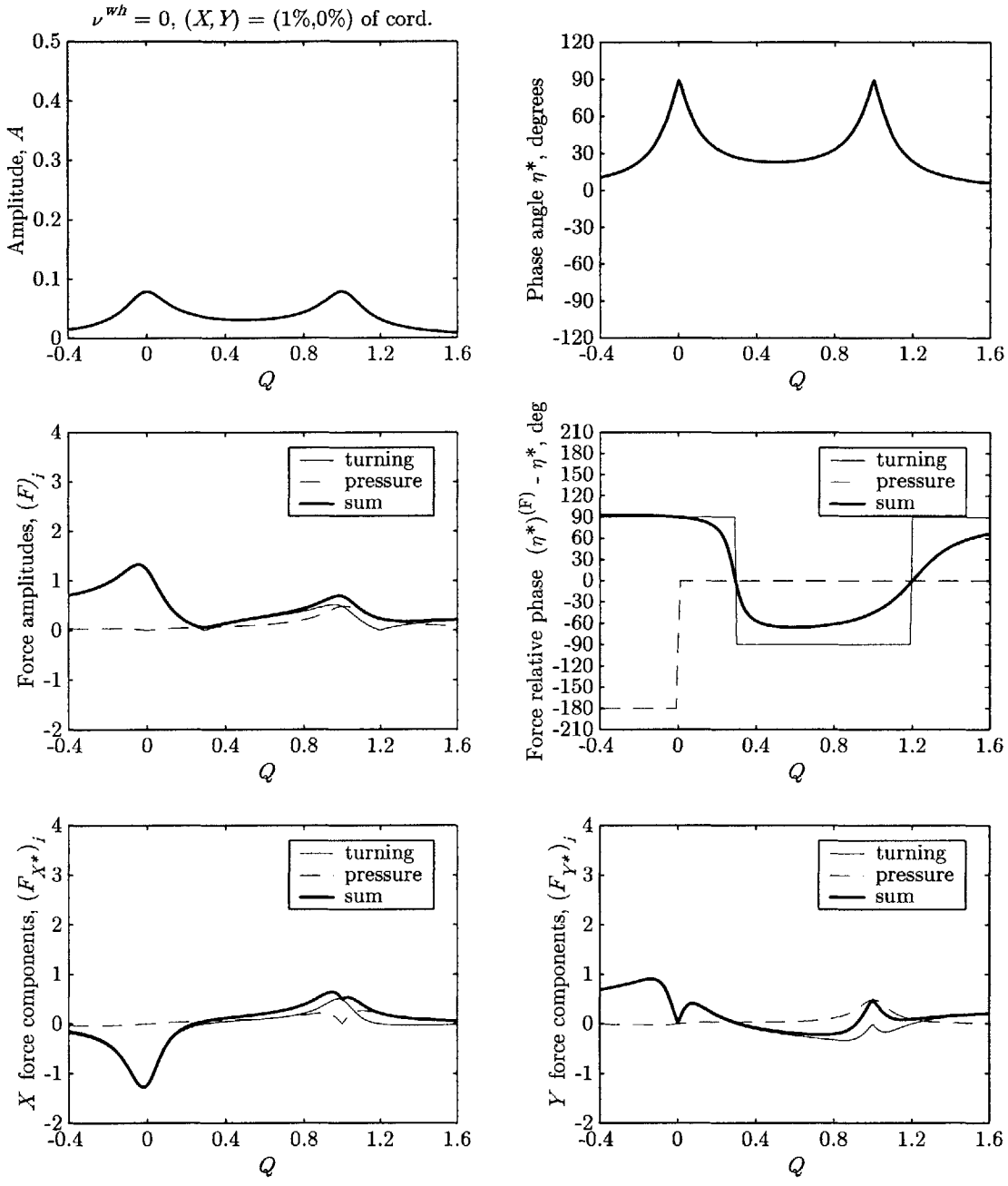

Figure 3-11: Flow nonuniformity and aerodynamic forces for fixed rotor offset as a function of operating point mean flow Q: Compressor C2, $\nu^{wh} = 0, r = 1.0\%$ chord.

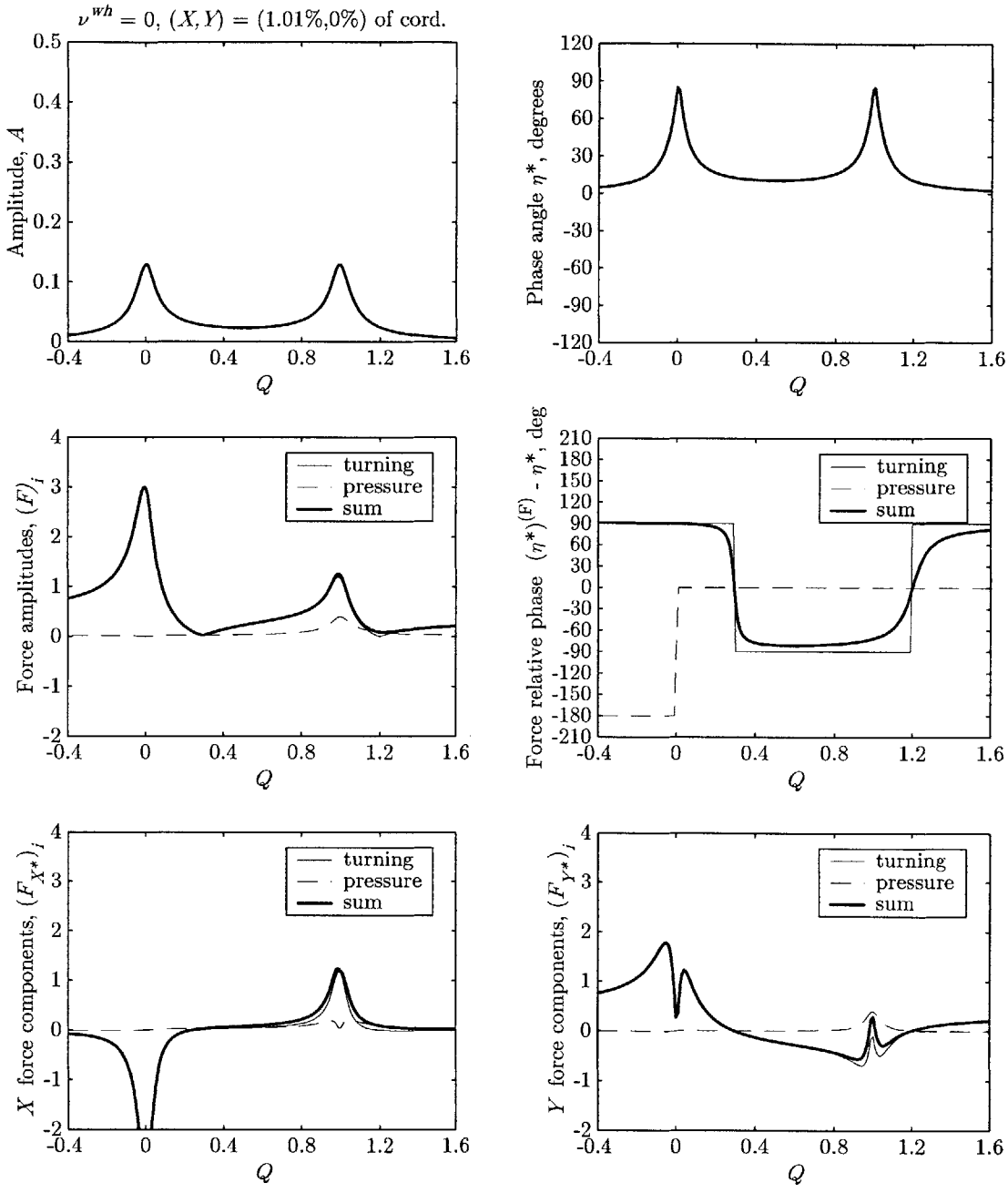

Figure 3-12: Flow nonuniformity and aerodynamic forces for fixed rotor offset as a function of operating point mean flow Q: Compressor C3, $\nu^{wh} = 0, r = 1.0\%$ chord.

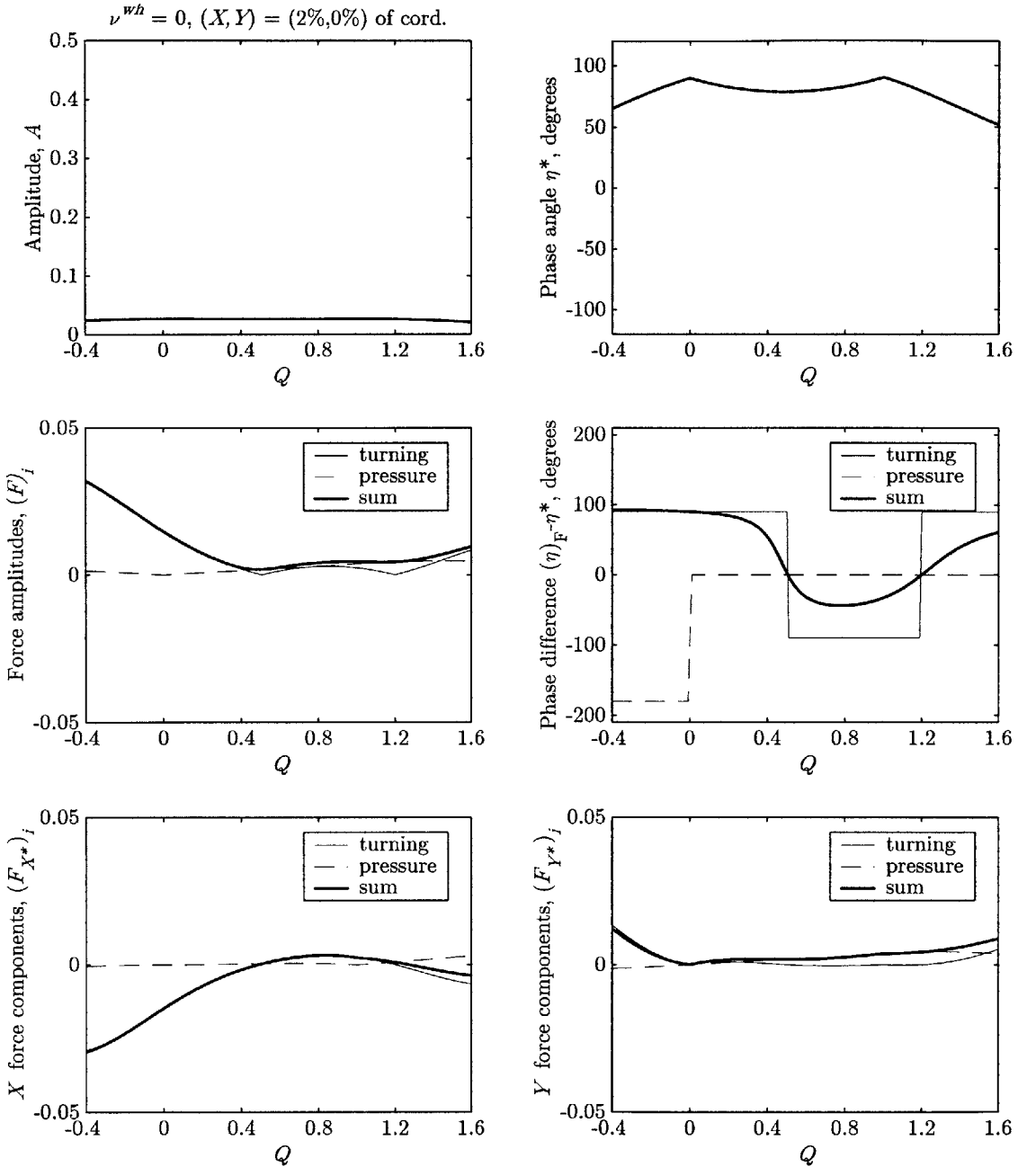

Figure 3-13: Flow nonuniformity and aerodynamic forces for fixed rotor offset as a function of operating point mean flow Q: Compressor C4, $\nu^{wh} = 0, r = 2.0\%$ chord. (Note the change in the abscissa scale).

3.3.4 Validation Against Experimental Data for Compressor C3

Here, we present the results of the previous calculation as applied to the compression system C3 and compare them to the data available from Storace et al. [73] and the numerical results reported by Ehrich et al. [22]. The results in these two references, and many others, are reported in terms of a parameter known as the Alford β-parameter, which we need to introduce first. The Alford β-parameter, or β^{Al}, emerged from Alford's original analysis as a nondimensional "correction factor" which multiplies the cross-coupled stiffness relating the aerodynamic force, say $(\tilde{F}_Y)_i$, to the rotor displacement $\tilde{X}$. As such, the β^{Al} parameter can also be viewed as the change of local thermodynamic efficiency per unit of rotor displacement. The value of β^{Al} is usually given an approximate number for a given machine. However, it later became apparent that β^{Al} is not constant, but rather is dependent on machine performance and operating point. Ehrich [19] calculated this parameter for three different compressors over a range of operating points using a parallel compressor model and torque measurements at different tip-clearance levels. He showed that β^{Al} depends on the operating point and that its operating-point dependency varies from one compressor to another.

Mathematically, β^{Al} is expressed as follows

$$(\tilde{F}_Y)_i = \underbrace{\beta_Y^{Al}\left(\frac{(\tilde{\tau}_c)_i}{2Rh}\right)}_{\substack{\text{cross-coupled}\\ \text{stiffness}}} \tilde{X} \quad \Rightarrow \quad \beta^{Al} = 2Rh\frac{(\tilde{F}_Y)_i}{(\tilde{\tau}_c)_i\ \tilde{X}}$$

or, in terms of the current nondimensional quantities

$$\beta_Y^{Al} = \frac{4}{\cos\gamma_r}\left(\frac{l_Z}{R}\right)^2\left(\frac{h}{l}\right)\frac{(F_Y)_i}{(\tau_c)_i\ X} \tag{3.22}$$

where the aerodynamic force $(F_Y)_i$ can be either that due to turning, $(F_Y^{tu})_i$, which gives $(\beta_Y^{Al})^{tu}$, or that due to pressure, $(F_Y^{pr})_i$, which gives $(\beta_Y^{Al})^{pr}$. As mentioned

earlier, until recently only the turning contribution was addressed in the literature, and most mention of the Alford β-parameter refers to that contribution.

The next step is to compare the pressure-rise characteristic used in the model to that obtained from measurements. Figure 3-14 shows two sets of characteristics. The first set consists of two pressure-rise measurements that correspond to two different mean tip-clearance settings of the compressor. The other set consists of three curves representing the modeled pressure-rise characteristic, using a rotor offset that results in a tip clearance distribution whose maximum and minimum match the two experimental clearance settings. It can be seen from the figure that the measured characteristics are more sensitive to tip-clearance around the peak than they are within the high flow coefficient part of the operating range. In addition, the peak of the characteristic shifts to the right for the larger tip-clearance. Such variation in sensitivity and shift in the peak can not be captured using the simple linear dependency of the characteristic on tip-clearance adopted in this thesis. To work around this limitation, we tune the parameters $S = H/W$ and $\psi_{c\varepsilon}$ such that the best match between the modeled and measured loss in pressure rise is achieved in the neighborhood of the design point, while being underestimated at the peak and overestimated in the high flow region.

Figure 3-15 shows the whirl-inducing component (i.e., the Y^* component) of the turning and pressure force contributions in terms of $(\beta_{Y^*}^{Al})^{tu}$ and $(\beta_{Y^*}^{Al})^{pr}$ over the full range of mean flow coefficient Q. The shaded area in both of these plots indicates the approximate range for which the experimental data is available and to which other numerical approaches are typically limited. Finally, Figure 3-16 zooms on that shaded region and shows the calculation results of the current model against the data and computational results in Storace et al. [73] and Ehrich et al. [22]. The predictions of the current model are shown to compare well against the measurements especially near the design point (i.e., $Q = 1.2$ to 1.3), where the characteristics matched the best. The error in predicted values $(\beta_{Y^*}^{Al})^{tu}$ becomes larger as we move closer to the characteristic peak at $Q = 1$. This is to be expected, however, because of the limitations in capturing

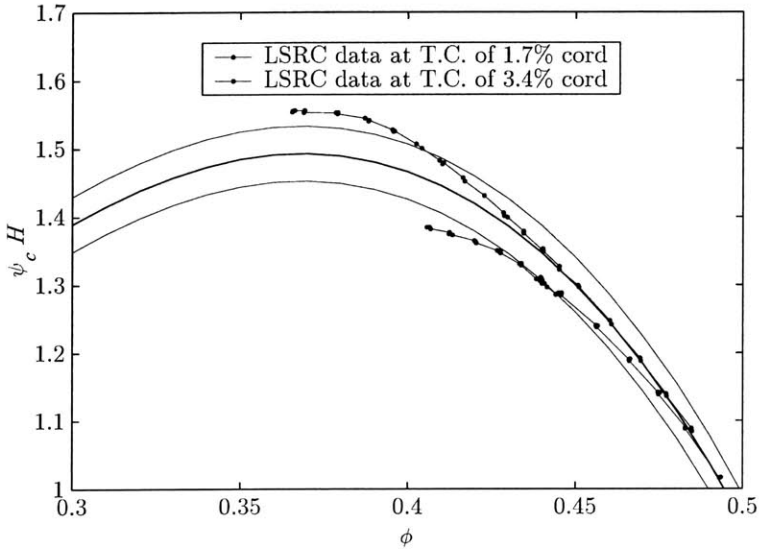

Figure 3-14: Measured and assumed pressure-rise characteristics for the GE LSRC, system C3.

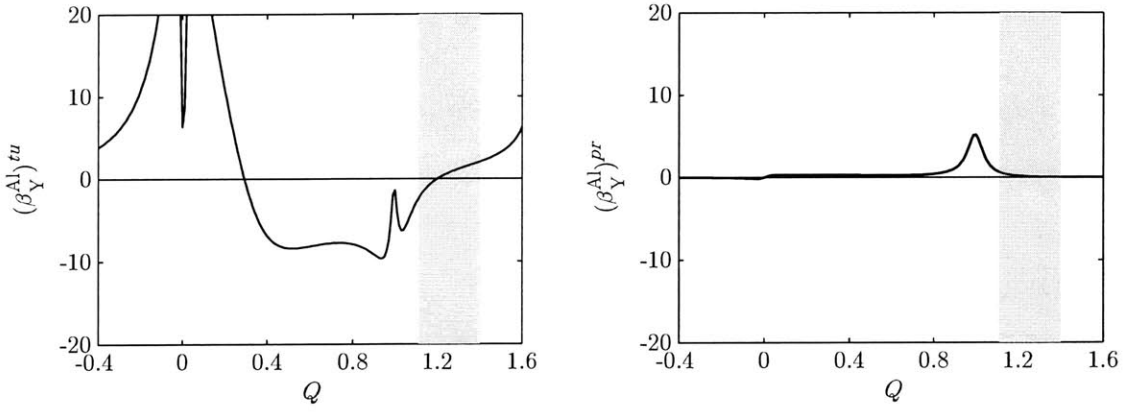

Figure 3-15: Alford's parameters $(\beta_{Y^*}^{Al})^{tu}$ and $(\beta_{Y^*}^{Al})^{pr}$, for fixed rotor offset of Compressor C3, $\nu^{wh} = 0, r = 1.0\%$ chord.

the compressor sensitivity to tip-clearance. Tuning the characteristic parameters such that the modeled characteristic in Figure 3-14 makes a better match around the peak brings the $(\beta_{Y*}^{Al})^{tu}$ prediction into closer agreement with the measurements in that region but causes it to deviate further in the high flow region (not shown).

The pressure contribution, as expressed in terms of $(\beta_{Y*}^{Al})^{pr}$ compares well against the numerical results by Spakovszky [71], while the match against measurement data is only good within the range $1.1 < Q < 1.25$, but deviates for larger values of Q.

3.3.5 Case of Forced Rotor Whirl

Let us now examine the case of nonzero whirling frequency ν^{wh}. We choose three values of ν^{wh}. In the backward whirl range, we consider one case at $\nu^{wh} = -0.5$. In the forward whirl range, on the other hand, we consider two cases. The first is at $\nu^{wh} = \nu^{rs}$ where we expect the flow nonuniformity, and hence the forces, to be maximized, Figure 3-17. The second is a higher value of $\nu^{wh} = 0.75$ representative of the rest of the forward whirl range. Based on examining additional values of ν^{wh}, it is deemed that these three choices sufficiently represent the whole region.

To show the effects of forced whirl on flow nonuniformity and aerodynamic forces, we consider the compression system C2. Figure 3-18 shows flow nonuniformity amplitude and phase for compressor C2 as a function of flow coefficient for 3 different values of whirl frequency, while Figures 3-19, 3-20 and 3-21 show the associated aerodynamic forces for the same compressor with the same rotor offset, corresponding to $\nu^{wh} = -0.5$, ν^{rs} and 0.75 respectively. The trends are in general similar to the fixed rotor case, except for the case when the whirl frequency is equal to the rotating stall frequency, Figure 3-20.

In the special case of $\nu^{wh} = \nu^{rs}$, Figure 3-20, we first note that the peak amplitude of the forces is roughly twice that of the fixed rotor offset. This is mainly the result of the larger flow nonuniformity amplitude A which was found to be maximized at this whirl frequency in Eq. (3.18). Next we note that the flow nonuniformity is exactly

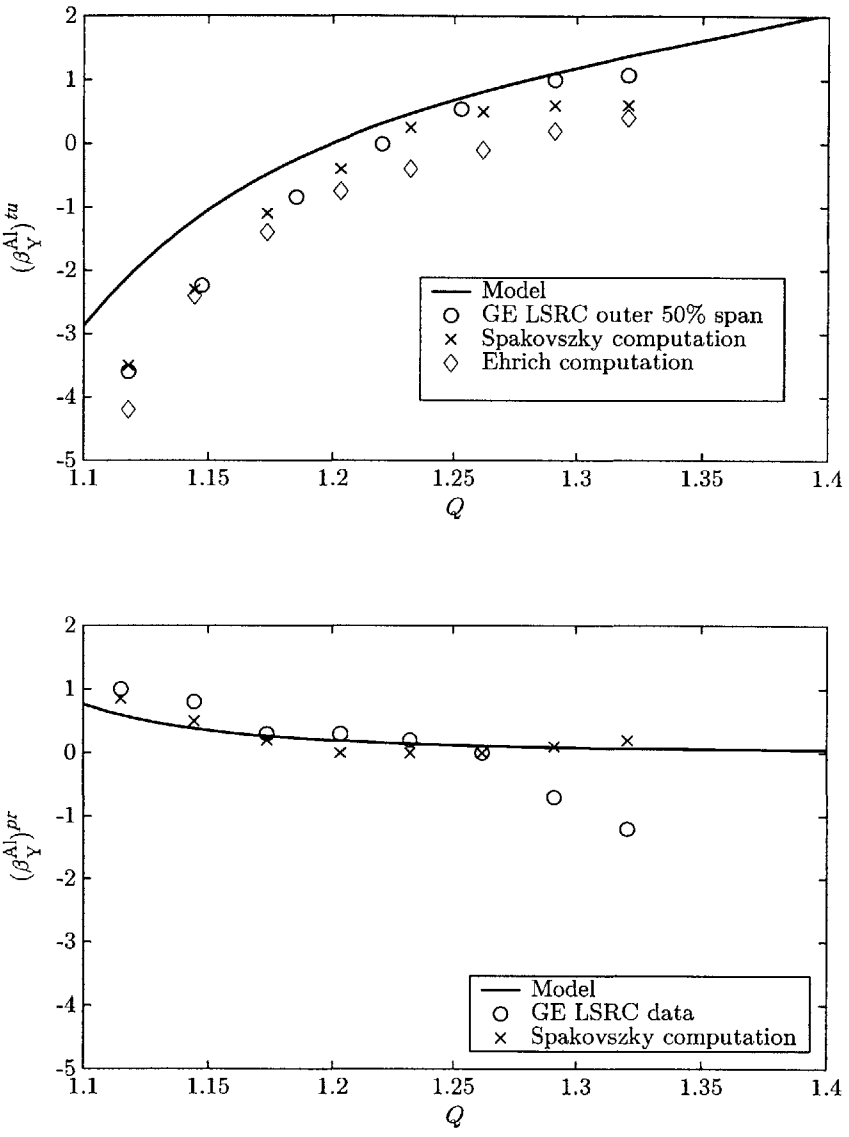

Figure 3-16: Comparison between experiment, numerical results, and this model. Results for $(\beta_{Y_*}^{Al})^{tu}$ and $(\beta_{Y_*}^{Al})^{pr}$, Compressor C3, $\nu^{wh} = 0, r = 1.0\%$ chord.

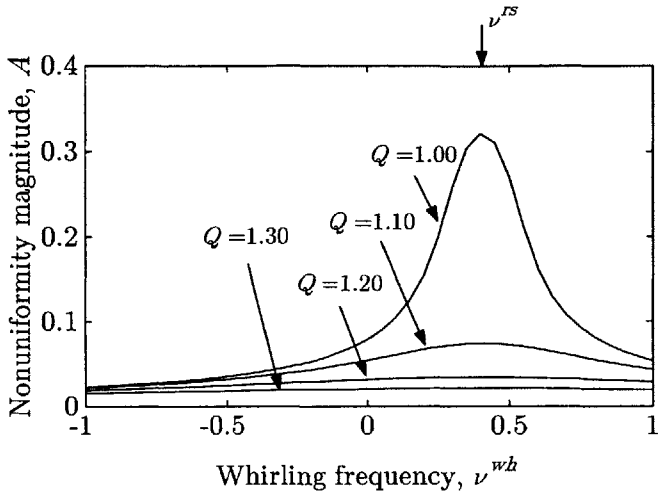

Figure 3-17: Flow nonuniformity amplitude as a function of whirl frequency ν^{wh}, for compressor C2 with $r = 1.0\%$ chord and different values of Q.

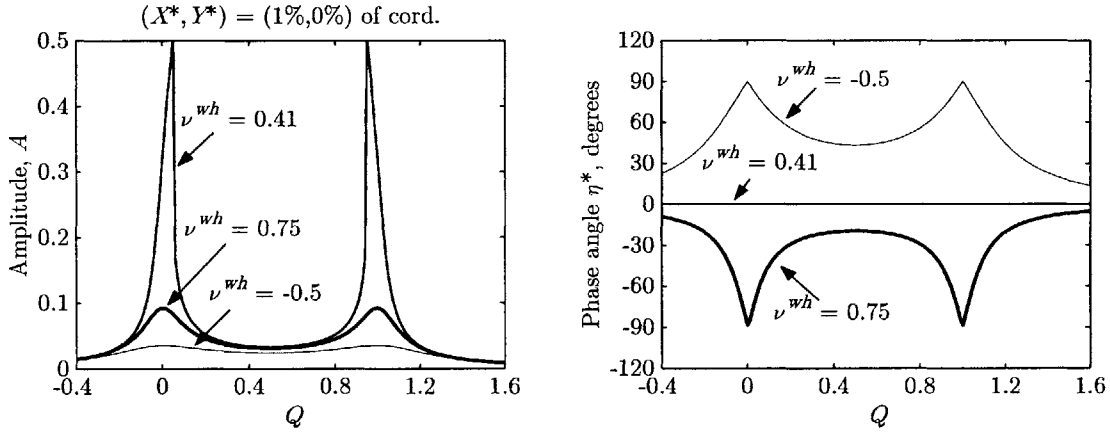

Figure 3-18: Flow nonuniformity under steady, forced rotor whirl, for compressor C2 at $\nu^{wh} = -0.5$ (backward), 0.4 (forward at ν^{rs}) and 0.75 (also forward), with $r = 1.0\%$ chord.

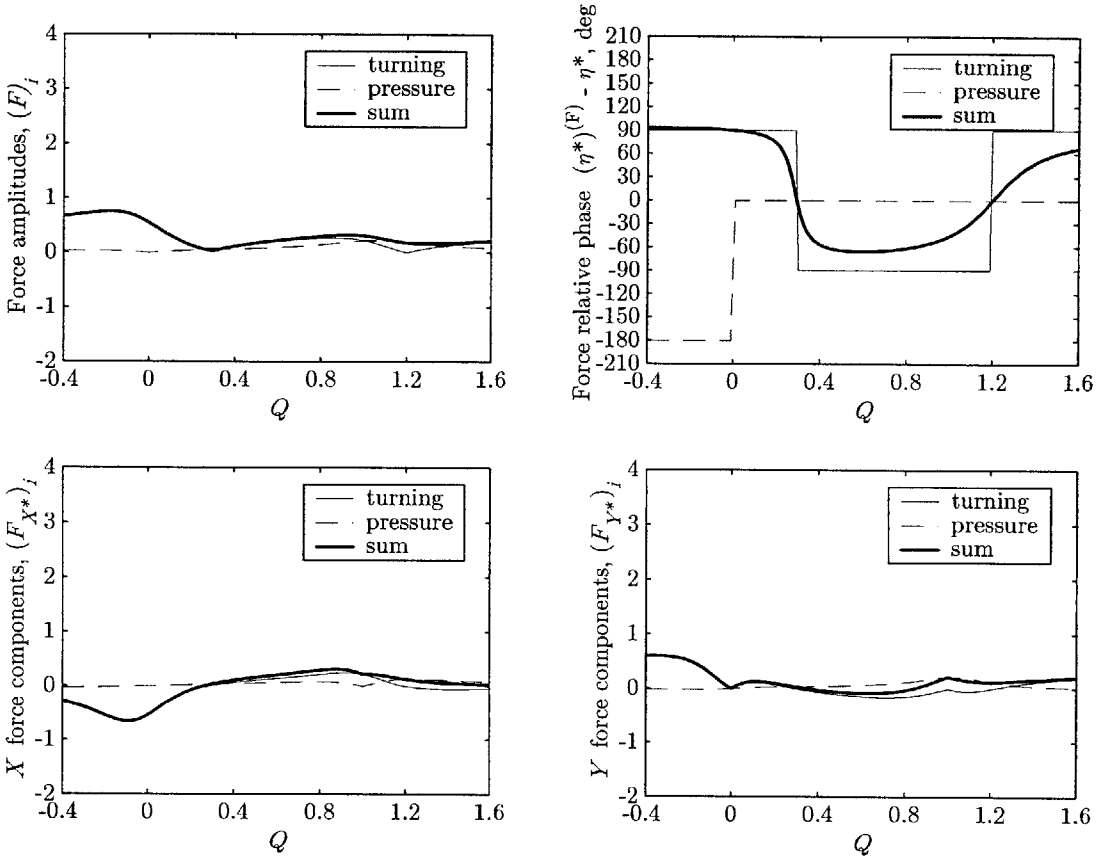

Figure 3-19: Aerodynamic forces for compressor C2 under forced backward whirl at $\nu^{wh} = -0.5$, with $r = 1.0\%$ chord.

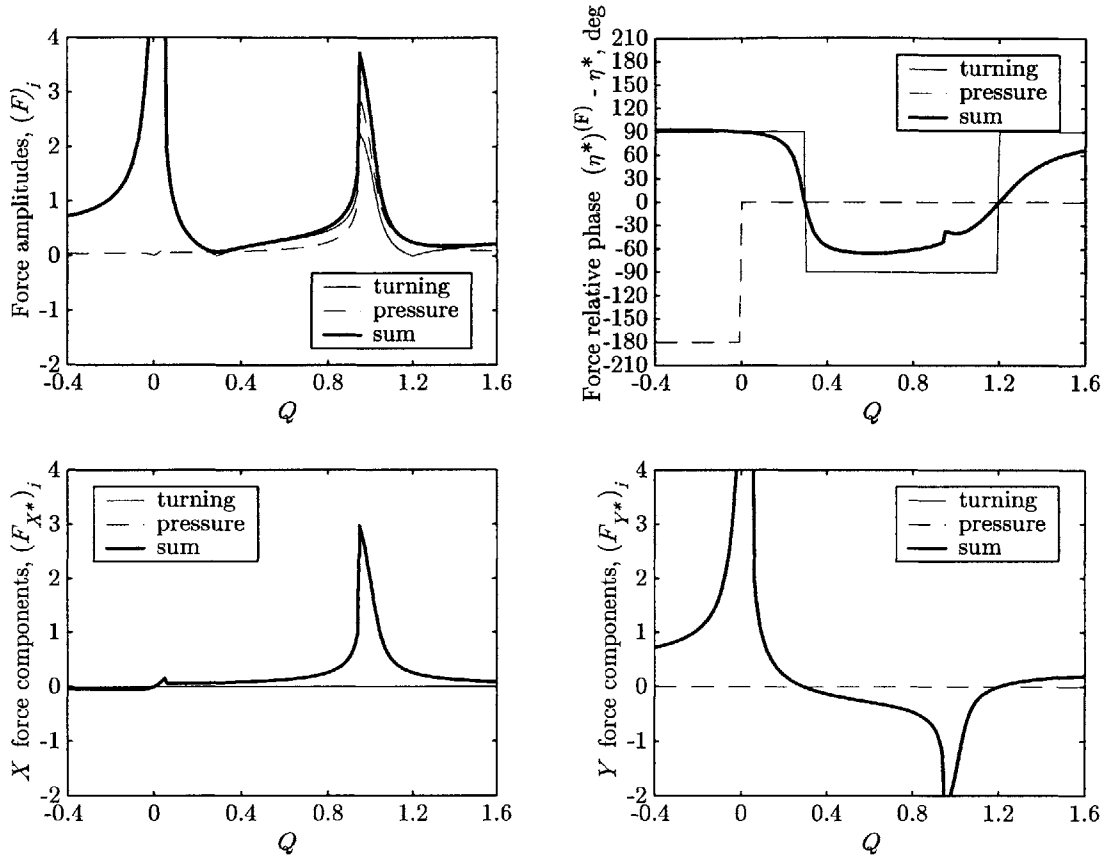

Figure 3-20: Aerodynamic forces for compressor C2 under forced forward whirl at $\nu^{wh} = 0.41 = \nu^{rs}$, with $r = 1.0\%$ chord.

aligned with the asymmetry, Figure 3-18. This causes the X^* force component (which is aligned with the rotor deflection) to be comprised only of pressure contribution, while the Y^* component to be comprised only of the turning contribution. In other words, the pressure force is exclusively providing the restoring force (mainly a negative spring effect) while the turning force is exclusively providing the whirl-inducing force. These observations are consistent with the general phase relations described in Section 3.2.

3.4 Summary and Discussion

In this chapter, the aerodynamic forces acting on the rotor have been examined. The model is shown to reasonably predict these forces for a given compressor geometry

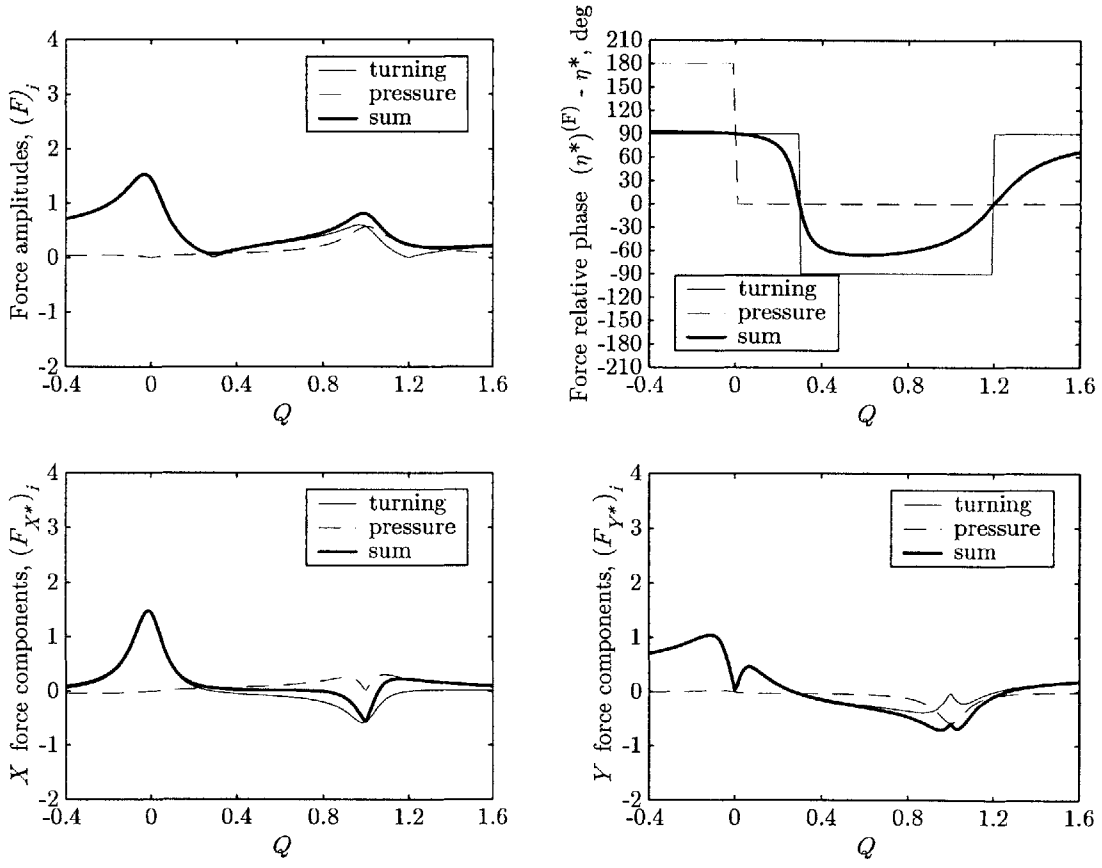

Figure 3-21: Aerodynamic forces for compressor C2 under forced forward whirl at $\nu^{wh} = 0.75$, with $r = 1.0\%$ chord.

and operating point. The following is a summary of the main conclusions of this chapter.

- Causality: an offset in rotor position introduces a tip-clearance asymmetry which interacts with the compression system and sets up a flow nonuniformity in flow velocity and pressure. This nonuniformity is typically out of phase with the asymmetry, mainly due to fluid inertia in the compressor. The momentum balance around the rotor gives rise to three force contributions, the amplitude and phase of which are closely linked to those of the flow nonuniformity.
- The dominant contribution to the aerodynamic forces is that due to turning, except for operating points between the peak and design points within which most of normal operation takes place. In this region, both pressure and turning contributions are of comparable importance.
- Whether the compressor whirls backward or forward due to these forces can not be established at this point (as the rest of the forces and the dynamic nature of the problem must be taken into account). Nevertheless, it is shown that, for a fixed rotor offset, the net aerodynamic forces *tend* to induce forward whirl for all operating points except in the region to the left of the design point, where backward whirl may or may not be possible depending on compressor parameters.
- The use of the β-parameter has no special advantage except for its traditional popularity. We have confirmed that this parameter is not a simple function of the operating point, and that a second β parameter corresponding to the pressure force contribution should be defined and considered in any such analysis.
- Many system parameters were shown to influence the aerodynamic forces either directly (e.g., χ^{tu}, χ^{pr} and χ^{un}) or indirectly by affecting the flow nonuniformity that produces the forces (e.g., λ/S and $\psi_{c\varepsilon}$).

Chapter 4

Coupling Impact on Stability: Linearized Analysis

In this chapter, we examine the linearized stability of the coupled baseline model, in the context of the four prototype compression systems introduced in the previous chapter. We first consider the case where the rotor is in equilibrium at the center of the compressor casing with no tip-clearance asymmetry. The linearized system equations about such an equilibrium (fixed point) are obtained by means of a Taylor series expansion of the baseline model equations. The stability of the system is then examined for various values of coupling parameters (i.e., $\psi_{c\varepsilon}, \chi$) and other system parameters (e.g., γ, B, and ν). The stability of a second class of equilibrium points, in which the rotor has a fixed offset within the casing, is then considered. We finally conclude the chapter by discussing the different trends observed from the analysis and attempting to link them to the design of axial compressors.

4.1 Linearized Baseline Model

4.1.1 Linearization of System Equations

The linearization of the system equations follows the standard Taylor series expansion about an equilibrium point, see for example Nayfeh [60]. In such a procedure, the

system equations are usually expressed as

$$\dot{\mathbf{x}} = \mathbf{f}(\mathbf{x}, \mathbf{k}) \tag{4.1}$$

where $\mathbf{x}$ is the state vector, $\mathbf{f}$ is the vector field, and $\mathbf{k}$ is a vector of control parameters. In the neighborhood of an equilibrium point[1] $\mathbf{x}_e$ corresponding to a set of control parameters $\mathbf{k}_e$, the solution $\mathbf{x}$ is expressed as $\mathbf{x} = \mathbf{x}_e + \mathbf{x}'$, where $\mathbf{x}'$ is a small disturbance. The linearized system equations are then obtained by substituting this solution into the original nonlinear equations, expanding in a Taylor series, and keeping only first order terms, yielding

$$\begin{aligned} \dot{\mathbf{x}} = \dot{\mathbf{x}}' &= \left.\frac{\partial \mathbf{f}}{\partial \mathbf{x}}\right|_{\mathbf{x}_e} (\mathbf{x} - \mathbf{x}_e) \\ &= \mathbb{A}\, \mathbf{x}' \end{aligned} \tag{4.2}$$

where $\mathbb{A} = \left.\frac{\partial \mathbf{f}}{\partial \mathbf{x}}\right|_{\mathbf{x}_e}$ is the Jacobian matrix, which is comprised of the first partial derivatives of the vector field $\mathbf{f}$ with respect to the states $\mathbf{x}$ and evaluated at the equilibrium point $\mathbf{x}_e$. The eigenvalues of the Jacobian matrix $\mathbb{A}$ determine the local stability of the system in the neighborhood of the equilibrium point $\mathbf{x}_e$.

For our baseline model, the state vector is $\mathbf{x} = [Q \quad P \quad a \quad b \quad X \quad V_X \quad Y \quad V_Y]$, the vector field $\mathbf{f}$ contains the RHS of the baseline system equations given in Section 2.3.3, and the control parameter vector contains one element; namely the throttling coefficient γ. The equilibrium point is defined by the vector $\mathbf{x}_e = [Q_e \quad P_e \quad a_e \quad b_e \quad X_e \quad (V_X)_e \quad Y_e \quad (V_Y)_e]$ and the control parameter γ_e, at which the LHS of Eq. (4.1) vanishes. Expressions for the elements of the Jacobian matrix $\mathbb{A}$ of the baseline model are given in Appendix C. Finally, within this chapter of linearized analysis and for brevity in notation, we drop the prime in $\mathbf{x}'$ and use $\mathbf{x}$ to indicate the disturbance state vector.

[1] Equilibrium points are also called fixed points or operating points. In this thesis we use these names interchangeably but settle for the subscript $_e$ to reference them.

4.1.2 Equilibrium Solutions

The equilibrium points, $\mathbf{x}_e$, encountered in this chapter are two types. The first corresponds to the simpler case of a centered rotor where the steady state solution $\mathbf{x}_e$ to the equations $\mathbf{f} = 0$ is almost trivial in that only (Q_e, P_e) are non-zero at equilibrium. Determining (Q_e, P_e) that correspond to some throttling coefficient γ_e requires the solution of two simultaneous algebraic equations; namely

$$\begin{aligned} 0 &= \bar{\psi}_c^C(Q_e, a_e = 0, b_e = 0) - P_e \\ &= \psi_{c0} + 1 + 3\,(Q_e - 0.5) - 4\,(Q_e - 0.5)^3 - P_e \end{aligned} \tag{4.3}$$

and,

$$0 = Q_e - \gamma_e \sqrt{P_e} \tag{4.4}$$

The second type of fixed points corresponds to the case where the rotor is deflected under the effect of gravity. Finding the fixed points in this case is more involved as it requires the solution of the following eight simultaneous algebraic equations

$$\begin{aligned} 0 &= \bar{\psi}_c^C(Q_e, a_e, b_e) - P_e \\ &= \psi_{c0} + 1 + 3\,(Q - 0.5) - 4\,(Q - 0.5)^3 - 6(a^2 + b^2) - P_e \end{aligned} \tag{4.5}$$

$$0 = Q_e - \gamma_e \sqrt{P_e} \tag{4.6}$$

$$\begin{aligned} 0 &= \frac{S}{2}\,\bar{\psi}_c^{Cc}(Q_e, a_e, b_e, X_e) \; - \; \lambda b_e \\ &= -3a_e\left[4Q_e(Q_e - 1) + (a_e^2 + b_e^2)\right] + \psi_{c\varepsilon} X_e - \; \lambda b_e \end{aligned} \tag{4.7}$$

$$\begin{aligned} 0 &= \frac{S}{2}\,\bar{\psi}_c^{Cs}(Q_e, a_e, b_e, Y_e) \; + \; \lambda a_e \\ &= -3b_e\left[4Q_e(Q_e - 1) + (a_e^2 + b_e^2)\right] + \psi_{c\varepsilon} Y_e + \; \lambda a_e \end{aligned} \tag{4.8}$$

$$0 = (V_X)_e \tag{4.9}$$

$$0 = -\nu^2 X_e - \varpi X_e^3 + \chi\left[(F_X^{tu})_i + (F_X^{pr})_i\right] \tag{4.10}$$

$$0 = (V_Y)_e \tag{4.11}$$

$$0 = -\nu^2 Y_e - \varpi Y_e^3 + \chi\left[(F_Y^{tu})_i + (F_Y^{pr})_i\right] - G_Y \tag{4.12}$$

which usually calls for the implementation of a numerical technique such as the Newton-Raphson method.

In both cases, however, we recognize that a change in our choice of control parameter can greatly reduce the computational cost of finding these equilibrium points. In fact, specifying the mean flow coefficient Q_e at the desired operating point as the control parameter instead of γ_e achieves just that. This is so because the complexity of these equations comes from the fact that Q_e appears mostly in the nonlinear terms such as the integrated characteristics and the aerodynamic force expressions. By choosing Q_e as a known control parameter, the equations become less coupled and easier to solve. Further, choosing values for Q_e is more intuitive since they can be read directly from the compressor map (e.g., $Q_e = 1.2$ is the design operating point and $Q_e = 1.0$ is the point of peak pressure rise on the compressor characteristic).

Therefore, in the case of the centered rotor, the equilibrium points are determined as follows. The compressor operating point at equilibrium is chosen by selecting a value of Q_e. Then Eq. (4.3) gives P_e by direct substitution. Equation (4.4) is then easily solved for $\gamma_e = Q_e/\sqrt{P_e}$.

In the off-centered rotor case, solving for the equilibrium points proceeds as follows. The compressor operating point at equilibrium is again chosen by selecting a value of Q_e. Now, only four (instead of eight) equations need to be solved simultaneously. Namely, Eqs. (4.7), (4.8), (4.10) and (4.12) are solved numerically for (a_e, b_e, X_e, Y_e). Finally, direct substitution gives P_e and γ_e from Eq. (4.5) and

Eq. (4.6) respectively.

4.2 Stability Bounds of the Coupled System: Parametric Studies

We now examine the stability of the coupled system by computing the eigenvalues and eigenvectors of the linearized baseline model in order to determine the stable and unstable regions in its multi-dimensional parameter space defined by the nondimensional parameters Q_e, χ, $\psi_{c\varepsilon}$ and ν. In addition, various prototype compressors are examined to capture the effects of compressor geometry ($\nu^{rs}, \chi^{tu}, \chi^{pr}, \chi^{un}, \ldots$) and pressure rise characteristic (ψ_{c0}, S). Given the relatively large number of relevant parameters, we follow a strategy in which we choose three parameters at a time, compute the stability boundaries as these parameters are varied, and observe the resulting trends. We also attempt to deduce parameter combinations that would reduce the total number of parameters needed to describe the impact of coupling.

In this section we choose the parameter set (Q_e, χ, ν) and examine all four prototype compression systems: C1, C2, C3 and C4.

4.2.1 Case of Centered Rotor

General features of the stability boundary

We start with the simpler case of centered rotor (i.e., no gravity). As described above, the equilibrium point in this case depends only on the compressor characteristic and throttle setting (represented by Q_e), and is therefore not altered as we change χ or ν. These equilibrium points are characterized by symmetric tip clearance and uniform steady flow (i.e., $a_e = b_e = X_e = Y_e = 0$ or $A_e = r_e = 0$).

In order to demonstrate the main features of aerodynamic-rotordynamic coupling effects on the stability of the overall system, we first present one set of results per-

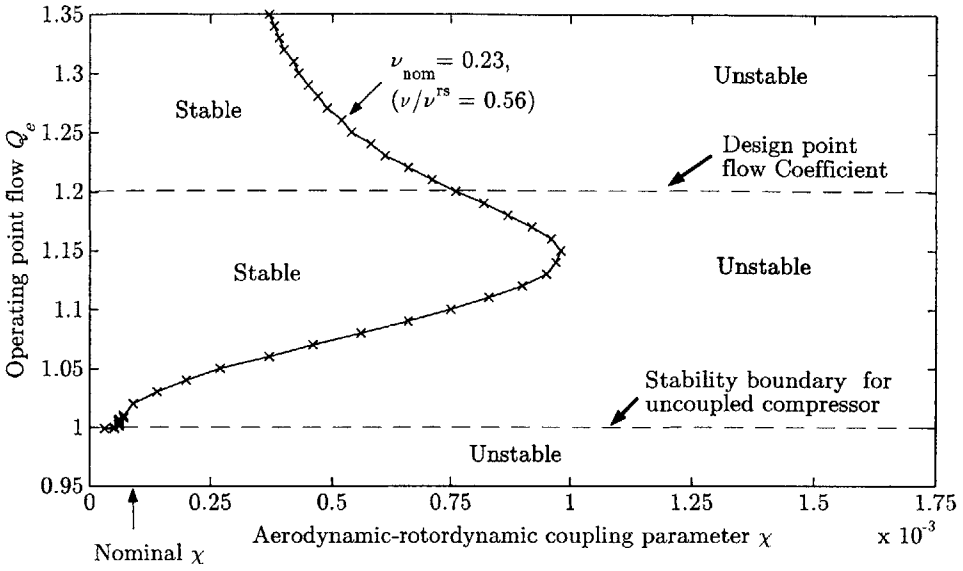

Figure 4-1: Coupled system linear stability boundary in the Q_e - χ parameter space: case of compressor C2, centered rotor, all parameters are at nominal values.(ν = 0.23 and $B = 0.1$).

taining to compressor C2 in which several important features are captured with the nominal set of system parameters. We recall that system C2 is a high pressure-rise compressor with a supercritical rotor, see Table 3.1. This set of results is then used as a benchmark case to compare the results that follow as we consider other prototype compressors and vary other parameters.

Figure 4-1 depicts the stability boundary for compressor C2 in the (Q_e, χ) space for the nominal value of ν, where the unstable region is that below and to the right of the solid line. In contrast to the uncoupled compressor which, according to the Moore-Greitzer model, loses stability (typically in the form of rotating stall) at the peak of the characteristic ($Q_e \leqslant 1$), the stability of the coupled system is shown to be degraded in that the onset of instability is encountered at operating points with a higher flow coefficient Q_e. (On a compressor map, the stability boundary of the coupled system would lie to the right of the peak of the characteristic). For instance, for values of $\chi = (2.5)10^{-4}$ and $(5)10^{-4}$, a reduction of the flow coefficient by throttling, say from the design point at $Q_e = 1.2$, takes the system into instability at $Q_e = 1.05$ and 1.08, respectively—a reduction of 5% and 8% in the stability margin predicted for the uncoupled compressor. For higher values of χ, the stability margin is further

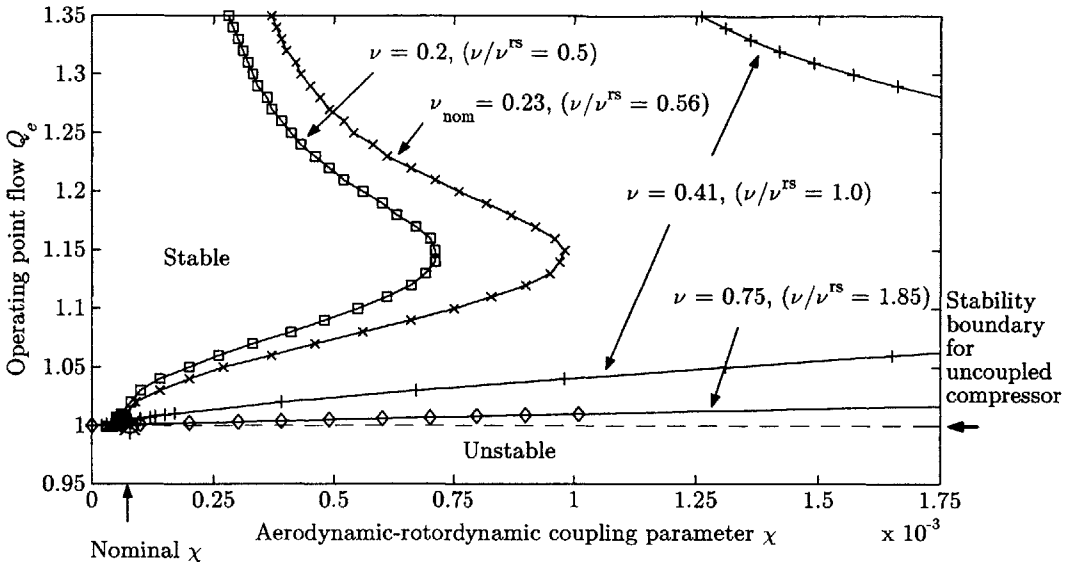

Figure 4-2: Effect of rotor's natural frequency (ν) on the coupled system linear stability boundary: compressor C2, centered rotor, all other parameters are kept at nominal values, ($B = 0.1$).

reduced until a critical value is reached around $\chi = (1)10^{-3}$, at which the system becomes unstable for all operating points Q_e. Furthermore, we observe that there exists a range of values of χ below the critical (in the range $(3)10^{-4} < \chi < (1)10^{-3}$), for which instability may be encountered at flow coefficients *higher* than the design point. For example, at a value of $\chi = (5)10^{-4}$, instability is encountered at $Q_e = 1.27$, giving a stability margin of only 7% in flow coefficient to the right of the design point.

Effect of Rotor's Natural Frequency, ν

The effect of the the rotor's natural frequency ν on this stability boundary is depicted in Figure 4-2 which, in addition to the stability boundary in the previous figure, shows the boundaries corresponding to three other values of ν selected as follows: $\nu = 0.2$ represents the highly supercritical rotor; $\nu = \nu^{rs}$ represents the case where the aerodynamic and rotordynamic uncoupled and undamped natural frequencies match; $\nu = 0.75$ represents the case of moderately supercritical rotor; and, finally, $\nu = \nu_{nom}$ is the nominal case. Note that the cases with $\nu = \nu^{rs}$ and $\nu = \nu_{nom}$ will be different

when we consider different prototype compressors, as those two special frequencies are properties of the system. In all these cases, the unstable region remains below and to the right of any of the solid lines. It can be seen from the figure that higher values of ν (e.g., corresponding to a stiffer rotor) have a larger stable region. For the cases with high enough ν (usually in subcritical range), the adverse effect of coupling is greatly reduced and the stability is closer to the uncoupled system. The stability boundary in such a case has only one branch that can be observed within this realistic range of flow coefficients. Also shown in the figure are the relative values of ν to ν^{rs} from which the closeness of these two frequencies can be inferred. As we will see later, this ratio determines some aspects of the stability of this coupled system.

Effect of Compressor Sensitivity to Tip-Clearance, $\psi_{c\varepsilon}$

We now examine the effect of the second coupling parameter, namely, the compressor sensitivity to tip clearance $\psi_{c\varepsilon}$. Figure 4-3 shows the stability boundary of compressor C2 for three different values of $\psi_{c\varepsilon}$. The less sensitive the compressor is to tip clearance the larger the stability margin for any given χ. This points towards the similar effect that the two coupling parameters have. We later make use of this observation and combine the two coupling parameters into one.

Comparison Between Prototype Compressors

To assess the effect of compressor geometry and characteristics on the overall system stability, we construct figures similar to Figure 4-2 for the other three compression system; namely C1, C3 and C4. The results are Figures 4-4, 4-5 and 4-6 respectively

The stability boundary of compression system C1 has similar features to that of C2, except that for the same value of ν system C1 has a lower critical value of χ (8.75e-3 and 1e-4 for C1 and C2 respectively) indicating a smaller stability margin for a given χ. As was shown above, this can be linked to the fact the C1 has a higher compressor tip-clearance sensitivity $\psi_{c\varepsilon}$, see Table 3.1.

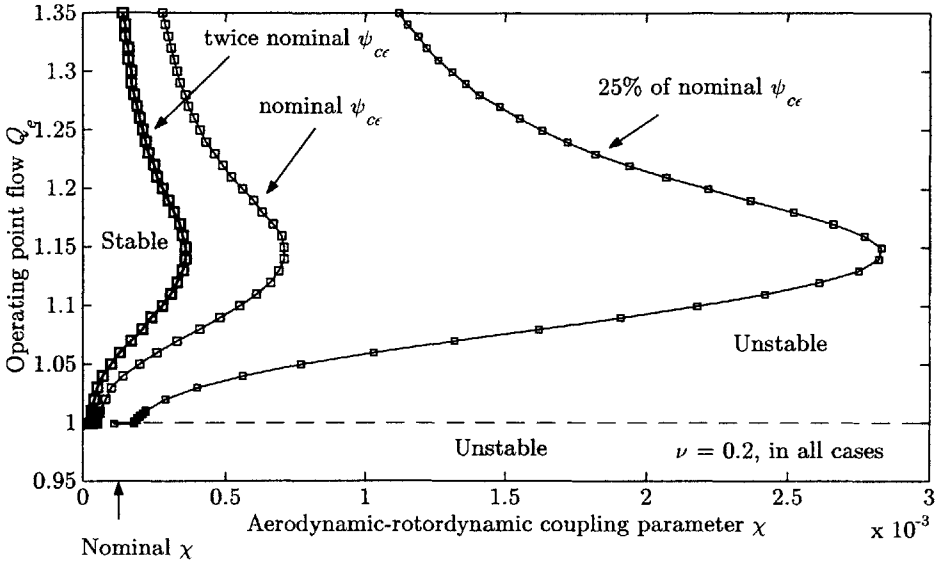

Figure 4-3: Effect of compressor tip clearance sensitivity on linear stability boundary of the coupled system: compressor C2, centered rotor, three values of $\psi_{c\varepsilon}$, $\nu = 0.2$ all other parameters are kept at nominal values, ($B = 0.1$).

In contrast to systems C1 and C2, system C3 shows different qualitative and quantitative features that are mainly the result of it having the lowest value of $\psi_{c\varepsilon}$ and λ/S. The region in the neighborhood of the design point of system C3 maintains its stability for much higher values of χ than systems C1 and C2.

Just like C3, the axial liquid pump, system C4, shows qualitative an quantitative differences in terms of its stability, as shown in Figure 4-6. These differences are mainly the result of the high coupling parameter χ, the high value of the pump sensitivity to tip-clearance[2], $\psi_{c\varepsilon}$, and the very small value of S (or more precisely larger value of λ/S). Several remarks are in order regarding to the stability of the axial liquid pump. To accomodate the same set of ν values as the previous systems, it was necessary to change to a logarithmic scale in this case. Having said that, we observe that for the case of highly supercritical rotor, $\nu = 0.2$, the stability boundary displays similar features to those of the other systems in the neighborhood of their respective nominal values of χ. For higher rotor natural frequencies, there emerges a

[2]Note that this is the rescaled sensitivity parameter, $\psi_{c\varepsilon} = \psi'_{c\varepsilon}/H$. For system C4, $\psi'_{c\varepsilon}$ is much smaller than that of any of the other (gas) compressors but H is even smaller, producing the net effect of higher $\psi_{c\varepsilon}$.

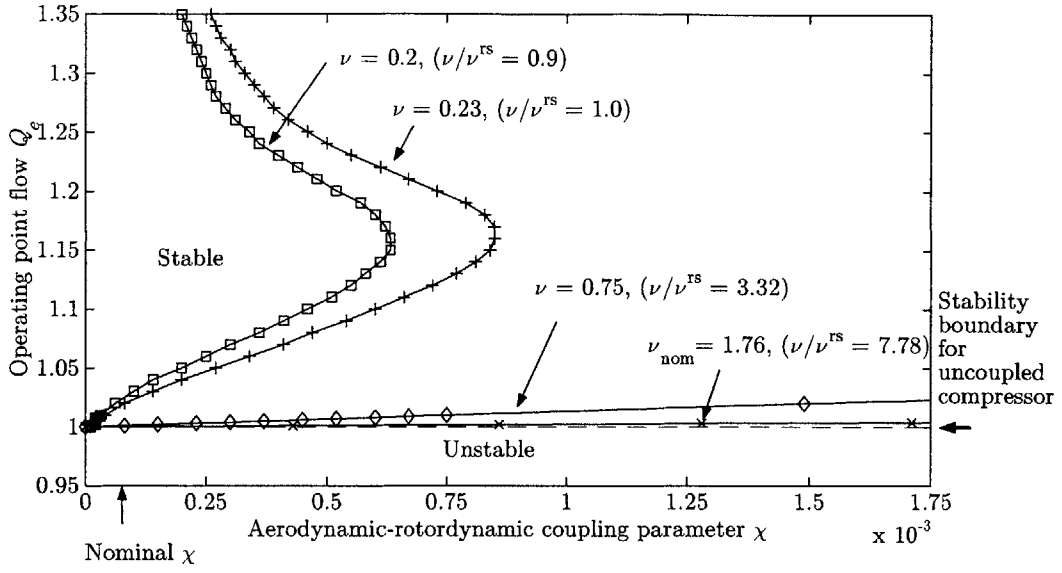

Figure 4-4: Linear stability boundary of the coupled system: compressor C1, centered rotor, four values of ν, all other parameters are kept at nominal values, (B = 0.1).

finite stabilizing influence of the coupling that persists over a wide range of ν, reaching a maximum of about 5% in stability margin extension at a value of $\nu = 0.35$ (not shown in the figure). Finally, for values of $\nu \gtrsim 0.75$, the complete loss of stability at high coupling occurs abruptly (even on a linear scale) as χ is increased, and does so right after the stability margin reaches a maximum. Comparing the nature of this transition in all four cases reveals that high values of $\psi_{c\varepsilon}$ and λ/S (which are highest in C4) correspond to abrupt loss of stability at high χ, while small values of $\psi_{c\varepsilon}$ and λ/S (which are smallest in C3) correspond to a gradual loss of stability at high χ, especially in the neighborhood of the design point (note the elongation to the right of the stable region of C3 in Figure 4-5).

Effect of the B-parameter

Similar calculations for various values of the B-parameter indicate that it has no effect on the stability boundary of the coupled system. This is expected since the B-parameter is known to be mostly influential in determining the post-instability behavior of the system. In particular, large values of the B-parameter ($B \sim 1$)

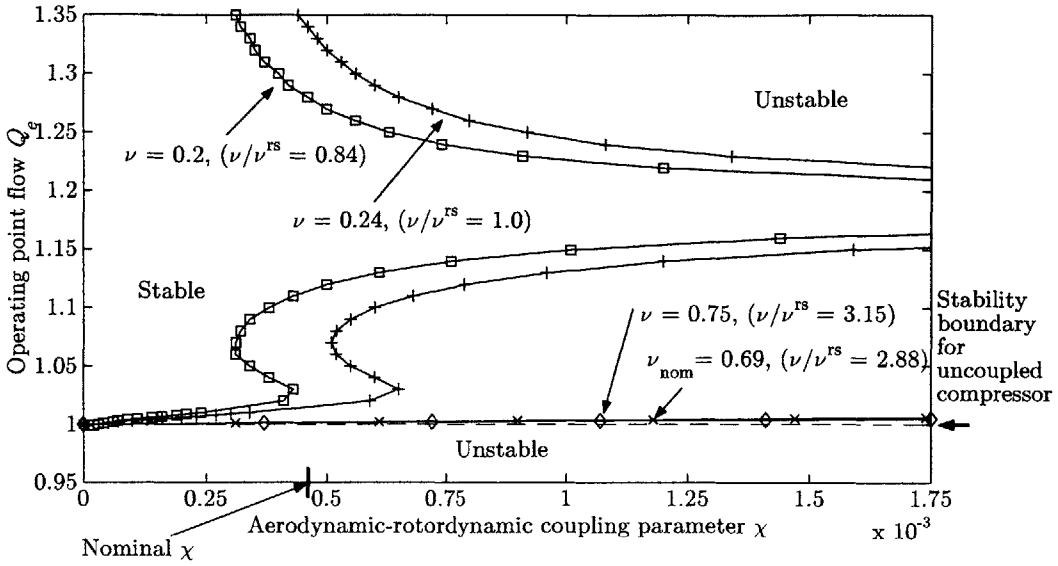

Figure 4-5: Linear stability boundary of the coupled system: compressor C3, centered rotor, four values of ν, all other parameters are kept at nominal values, ($B = 0.1$).

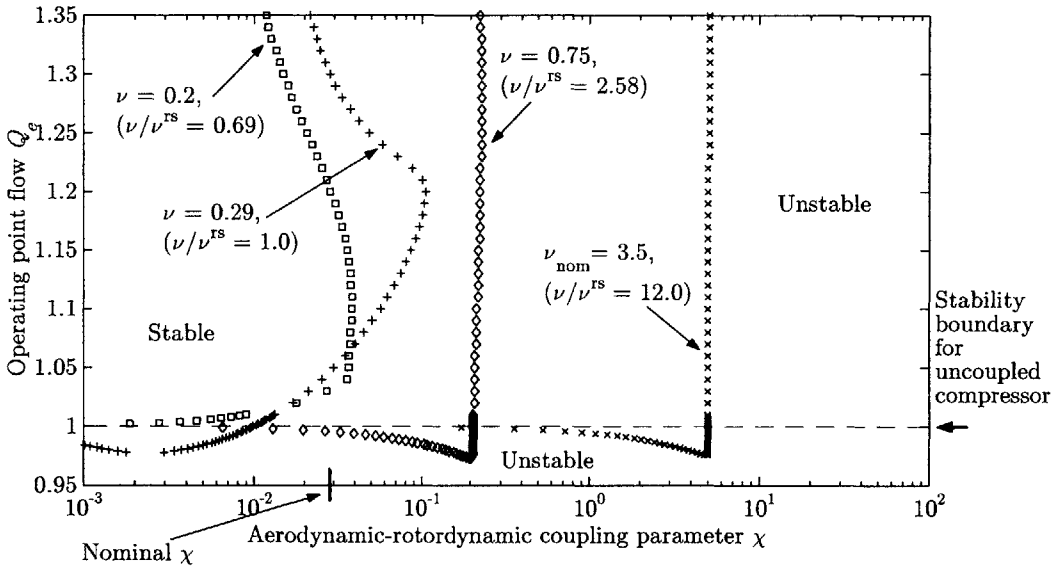

Figure 4-6: Linear stability boundary of the coupled system: compressor C3, centered rotor, four values of ν, all other parameters are kept at nominal values, ($B = 0.1$). (Note the change in the abscissa scale).

are typically associated with surge while small values ($B \sim 0.1$) are associated with rotating stall. In the class of lumped parameter models of pumping systems that do not account for any spatial flow nonuniformity (e.g., Greitzer [31] and Abed et al. [1]), the B-parameter is the main system parameter and the only mode of instability captured by such models is, in fact, surge. Rotating stall, on the other hand, appears as a stable operating point on the stalled compressor characteristic used as the main input to these models.

In the current model, however, the effect of the B-parameter is addressed when we discuss the post-instability behavior in the next chapter.

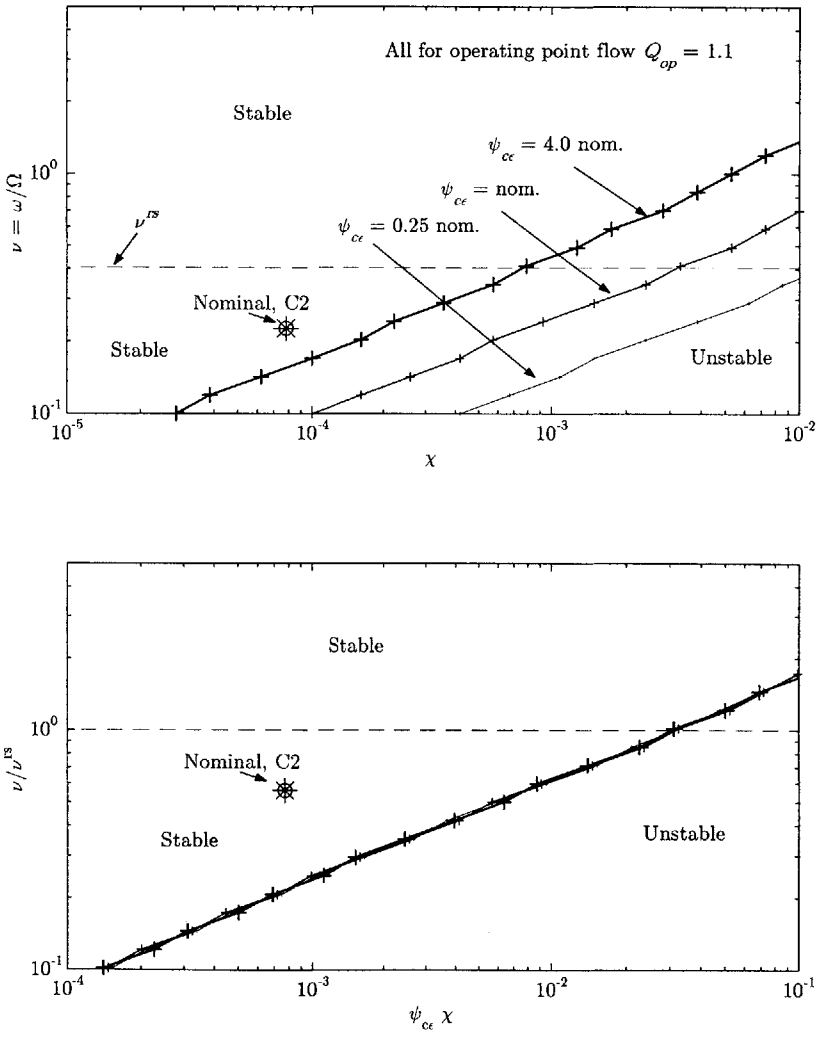

Figure 4-7: Linear stability in the design parameter space: combining the two coupling parameters as $\psi_{c\epsilon}\chi$, for compressor C2, all other parameters are at nominal values.

4.2.2 Stability Bounds in the Design Parameter Space: Reduction of Coupling Parameters

An alternative way to view the stability results is to consider the parameter space χ vs. ν. In such a space, we construct a stability boundary, corresponding to some operating point flow coefficient Q_e, which splits the space into a stable and unstable parameter combinations (χ,ν). This view serves to elucidate how the stability of the system is affected as these two design parameters are changed. Further, the effect

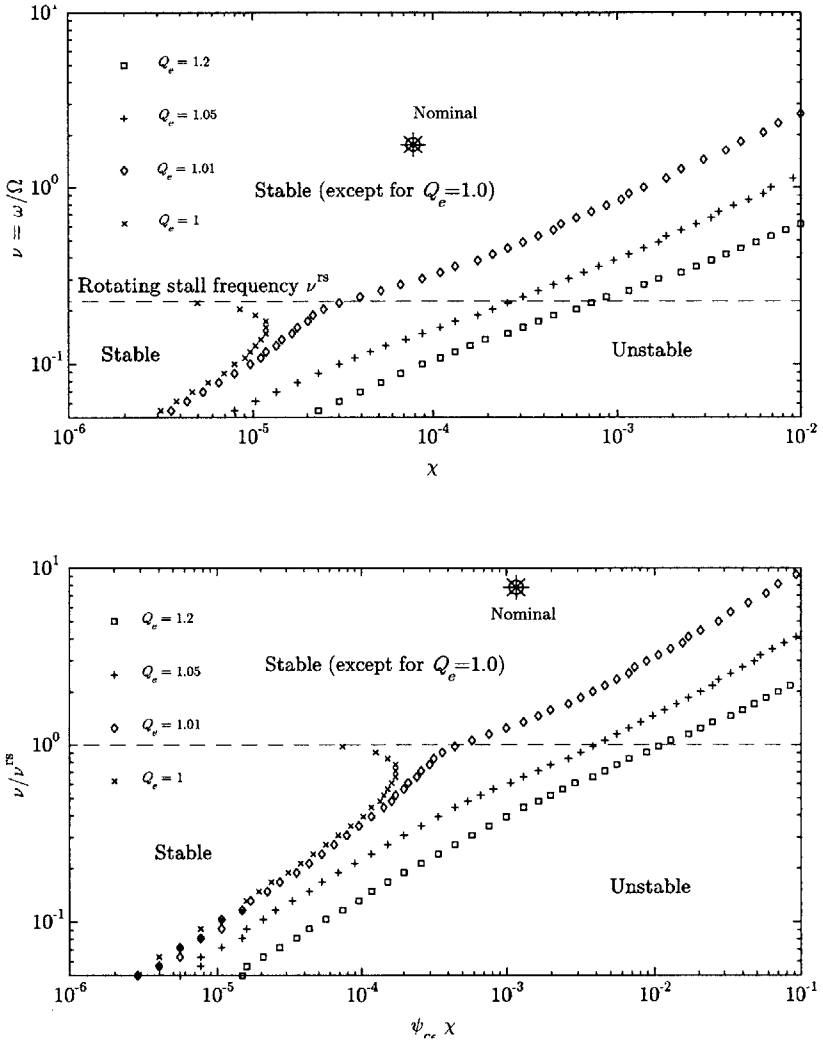

Figure 4-8: Linear stability in the design parameter space: compressor C1, for four different operating flow coefficients. All other parameters are at their nominal values.

of compressor sensitivity to tip clearance on stability, shown in Figure 4-3, suggests

that the two coupling parameters $\psi_{c\varepsilon}$ and χ influence the stability of the coupled system in a similar manner. In fact, looking back at the system equations given in Section 2.3.3, we note that a rescaling can be adopted such that only the product of these two parameters appear. In particular, rescaling the rotor displacement variables X and Y with χ causes the latter to disappear from the rotordynamic equations and appear instead in the equations of $\dot{a}$ and $\dot{b}$ as the product $\psi_{c\varepsilon}\chi$. This reduction in coupling parameters is captured in Figure 4-7, where the stability boundaries due to different values of tip clearance sensitivity in the first sub-plot collapse onto one boundary in the reduced parameter space in the second sub-plot.

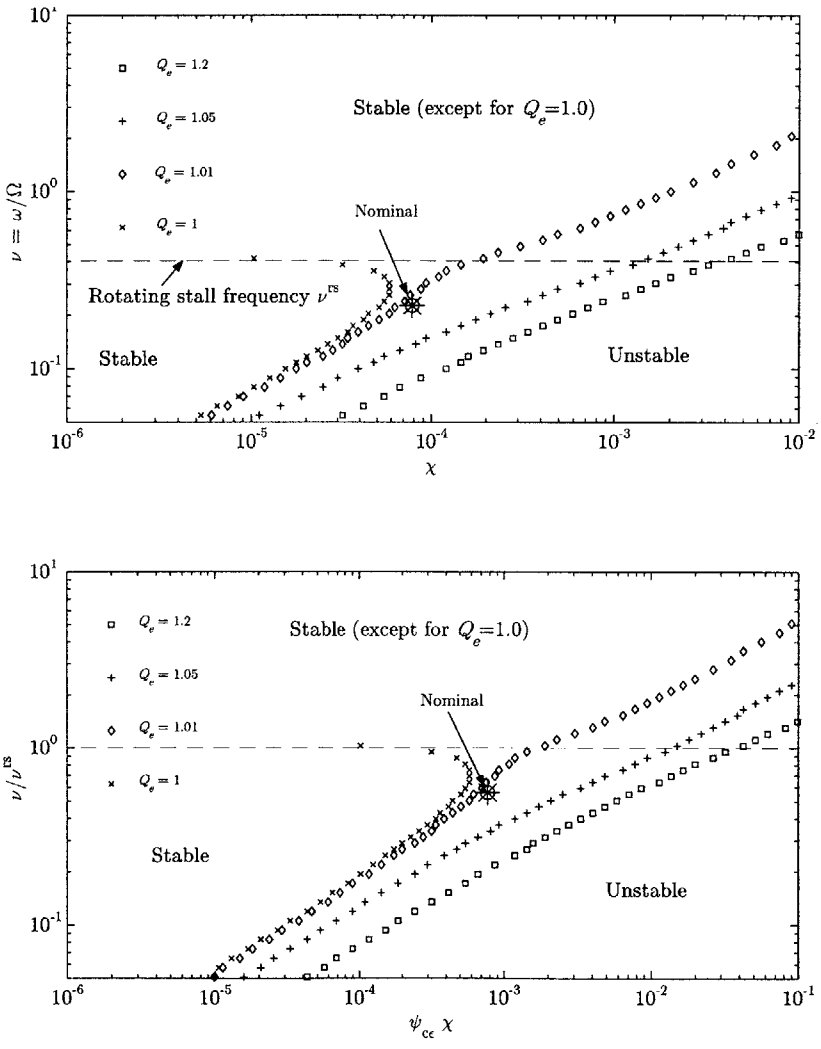

Figure 4-9: Linear stability in the design parameter space: compressor C2, for four different operating flow coefficients. All other parameters are at their nominal values.

In each of the following four figures, Figures 4-8 to 4-11, corresponding to the four prototype compression systems, we show two versions of this design parameter space: the first shows χ vs. ν while the second shows $\psi_{c\varepsilon}\chi$ vs. ν/ν^{rs}. Each line in these figures corresponds to an operating point flow coefficient Q_e and divides the plane into a stable and unstable regions—the unstable region being that below and to the right of these lines (except for $Q_e = 1.0$ where the stable region is confined to the lower left corner of the plane). The use of the ratio $\nu/\nu^{rs} = \omega/\omega^{rs}$ (which does not depend on the rotor spinning speed Ω) in the second sub-plots of these figures is motivated by the observation that for the first three prototype systems C1, C2 and C3, the stability boundary for flow coefficients to the right of the characteristic peak (i.e., $Q_e > 1$) changes monotonically with ν, while for $Q_e = 1$ rotors with natural frequencies ν *higher* than their compressor's rotating stall frequency ν^{rs} become unstable first for all values of χ. However, any further throttling (i.e., for $Q_e < 1$) renders the system unstable for all values of χ and ν. Although the difference between systems above and below this critical frequency ($\nu/\nu^{rs} = 1.0$) does not amount to a significant change in stability margin, it is shown later that this is linked to the different modes of instability that can take place in these systems. By inspecting the second of the two sub-plots in Figures 4-8, 4-9 and 4-10, we observe that the stability boundaries are roughly in the same range, suggesting that the parameter space ($\psi_{c\varepsilon}\chi$,ν/ν^{rs}) is somewhat universal for this class of compression systems.

The qualitative and quantitative differences observed previously in the case of the liquid axial pump are also reflected here and are shown in Figure 4-11. For the purpose of clarity, we split this figure into a series of four sub-plots, each corresponding to an operating point flow coefficient Q_e. We note that the effect of the ratio ν/ν^{rs} discussed above for C1, C2 and C3, is somewhat reversed in the case of C4 (third and forth sub-plots) in that rotors with natural frequencies, ν, that are *lower* than their compressor's (or pump, in this case) rotating stall frequency ν^{rs}, (i.e., $\nu/\nu^{rs} < 1.0$), become unstable first for all values of χ as the compressor is throttled to $Q_e < 1.0$. In addition, unlike the first three compression systems, this extension in stability margin in the case of C4 extends further (just as discussed previously) to include operating

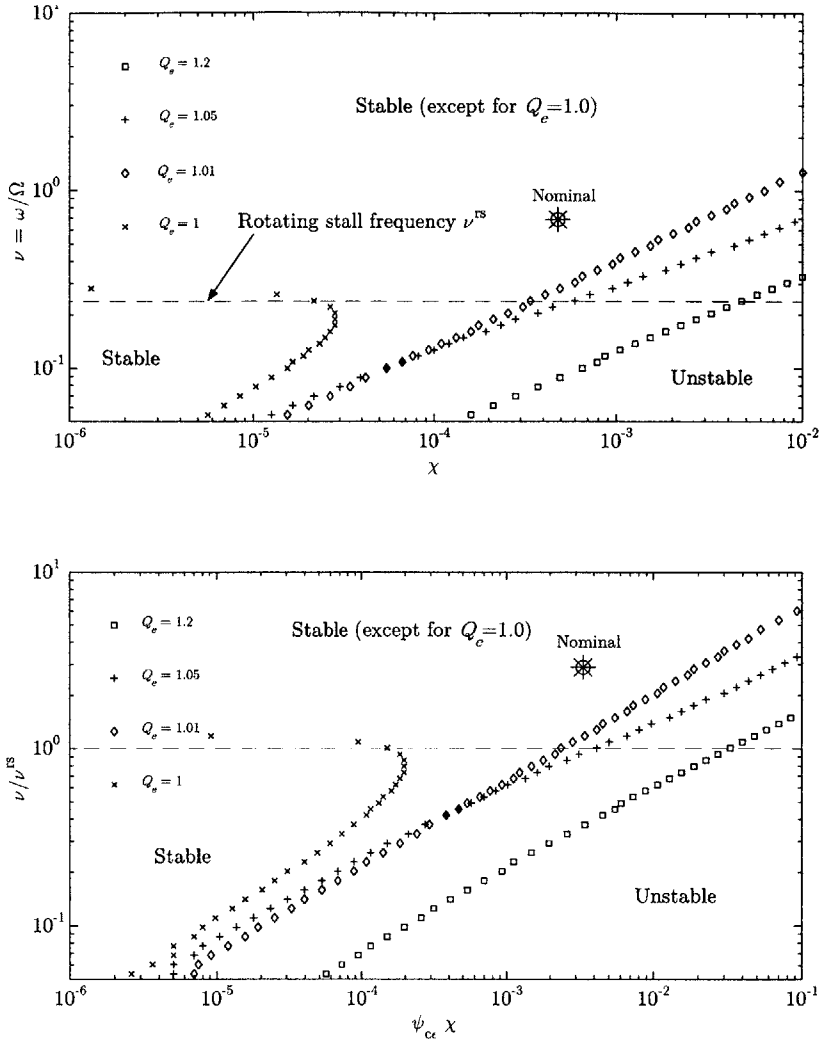

Figure 4-10: Linear stability in the design parameter space: compressor C3, for four different operating flow coefficients. All other parameters are at their nominal values.

points to the left of the characteristic peak. This is reflected in the fourth sub-plot where a band of parameters that corresponds to stable operation exists even at the low flow operating point of $Q_e = 0.98$.

4.2.3 Case of Off-Centered Rotor

We now turn our attention to the case where the rotor is displaced from the geometric center of the compressor casing and is kept in equilibrium by the action of an additional constant force, which we take as gravity. In such a steady state configuration,

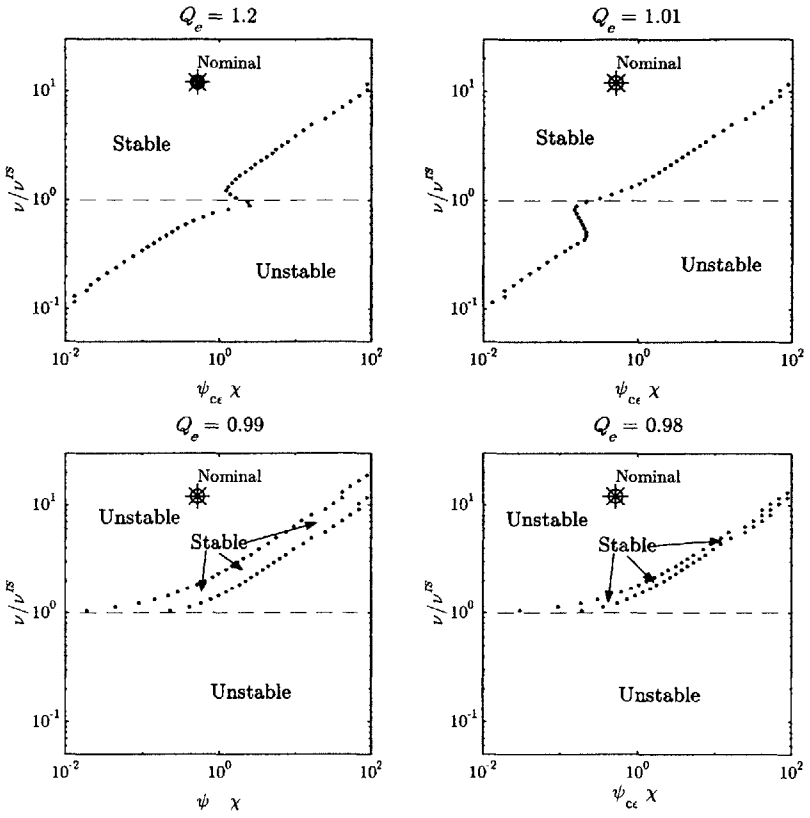

Figure 4-11: Linear stability in the design parameter space: compressor C4, for four different operating flow coefficients. All other parameters are at their nominal values.

a tip-clearance asymmetry is present, together with a flow nonuniformity. In order to examine the stability of this type of equilibrium point, the steady state equations need to be solved for the equilibrium point $\mathbf{x}_e$ as described in section 4.1.2. Consequently, as we vary any parameter (e.g., Q_e or χ), the equilibrium point will change accordingly.

The results of such an exercise are shown in Figure 4-12 for system C2. The figure shows the stability boundary in the (Q_e, χ) parameter space, just as before, in addition to four more sub-plots showing the migration of the equilibrium points that are neutrally stable (i.e., exactly on the stability boundary) as a function of the coupling parameter χ. Inspection of the stability boundary in this case shows that the deflection of the rotor has a stabilizing effect in that the loss in stability margin is limited to about 3 to 4% over the same range of coupling parameter values

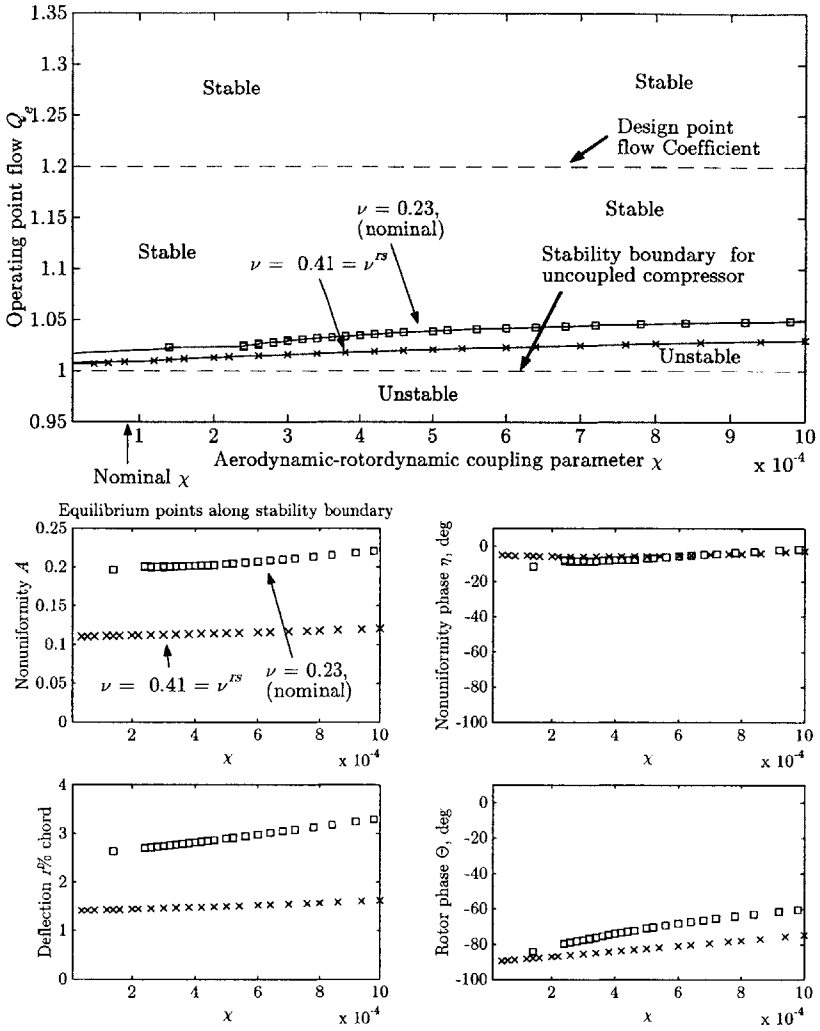

Figure 4-12: Linear stability boundary of the coupled system: compressor C2, off-centered rotor, two values of ν, all other parameters are kept at nominal values, ($B = 0.1$).

considered in the centered case. As we move along the stability boundary towards higher values of coupling parameter χ, it is seen that the rotor displacement due to gravity, r, increases while its orientation, Θ, becomes closer to the X axis. In order to compare this case to the centered rotor, the stability boundary of both cases are shown in Figure 4-13 for the same value of ν.

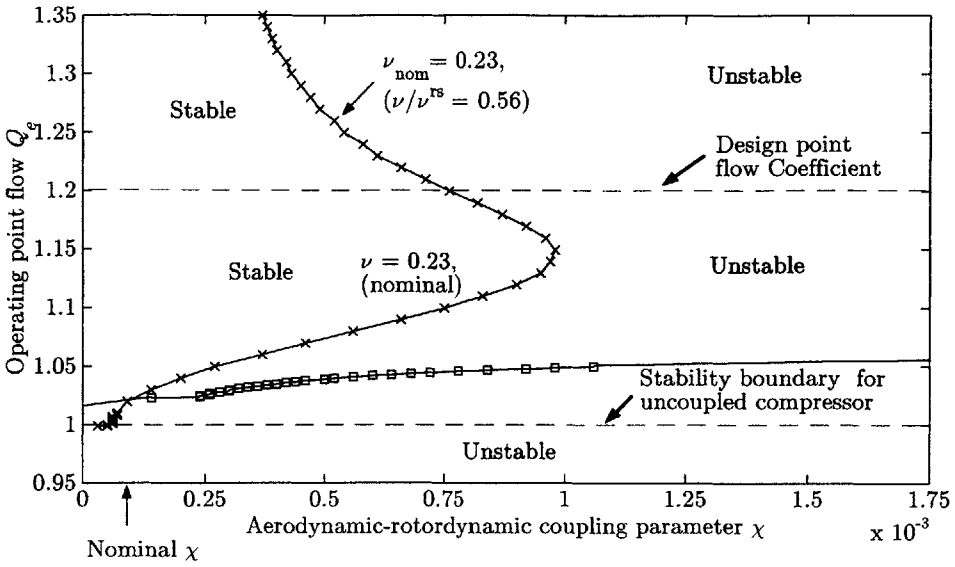

Figure 4-13: Linear stability boundary of the coupled system: Comparison between the centered and off-centered rotor, compressor C2, ν = nominal, all other parameters are kept at nominal values, ($B = 0.1$).

4.3 Modes of Instability: Aerodynamic vs. Rotordynamic Instabilities

We now set out to examine the nature of instability encountered as the stability boundaries discussed above are crossed. For an uncoupled compressor with a low B parameter, the dominant mode of instability encountered as the compressor is throttled to flow coefficients $Q_e < 1$ is known to be rotating stall. In what follows, we address the question of how the coupled system differs from the uncoupled system as it loses stability at either end of the stability margin. To that end, we identify the first pair of eigenvalues to cross the imaginary axis as the coupled system loses stability, and examine the modal structure of the corresponding eigenvector.

4.3.1 Case of Centered Rotor

In order to answer the above question for the case of the centered rotor, we present four scenarios in which one of the prototype compressors, say C2, loses stability. In particular, we consider two of the stability boundaries shown in Figure 4-2 correspond-

ing to two rotor frequencies that are far apart, say $\nu = 0.23$ which is the nominal value of C2, and $\nu = 0.75$. In terms of the ratio ν/ν^{rs}, these two correspond to 0.56 and 1.85 respectively (i.e., the rotor frequency is below the rotating stall frequency for the first and above for the second). Next, we choose a value of the coupling parameter for each case, say $\chi = (0.5)10^{-3}$ for the case of $\nu = 0.23$ and $\chi = (1.5)10^{-3}$ for $\nu = 0.75$. We note from Figure 4-2 that for the smaller ν, the stability margin is bound on both sides, while for the larger ν the system loses stability only as the flow coefficient is decreased. Table 4.1 summarizes these scenario as well as the main findings, which we describe next.

	$\nu = 0.23$ (nominal)	$\nu = 0.75$
ν/ν^{rs}	0.56	1.85
χ	$(0.5)10^{-3}$	$(1.5)10^{-3}$
Q_e at lower stability boundary	1.07	1.02
unstable mode frequency/ν^{rs}	0.35	0.83
unstable mode	rotordynamic	aerodynamic
Q_e at upper stability boundary	1.27	none
unstable mode frequency/ν^{rs}	0.51	–
unstable mode	rotordynamic	–

Table 4.1: Summary of scenarios of losing system stability for compressor C2, and identification of different modes of instability.

Figure 4-14 shows the eigenvalues and eigenvectors corresponding to the case of $\nu = 0.23$. We start with the first column of sub-plots which depicts the locus of eigenvalues (only positive frequencies are shown) as the operating point Q_e is reduced from design point $Q_e = 1.2$ to 0.9; the magnitude of the eigenvectors at crossing; and the locus of equilibrium points represented by the nonuniformity amplitude A (this is zero for all operating points in this case of centered rotor). The frequency of the crossing eigenvalue and the structure of the corresponding eigenvector suggest that the instability encountered here is of a rotordynamic nature. We note however, that the aerodynamic (rotating stall) eigenvalue also becomes unstable as the compressor is throttled further. On the other hand, the second column of sub-plots shows the

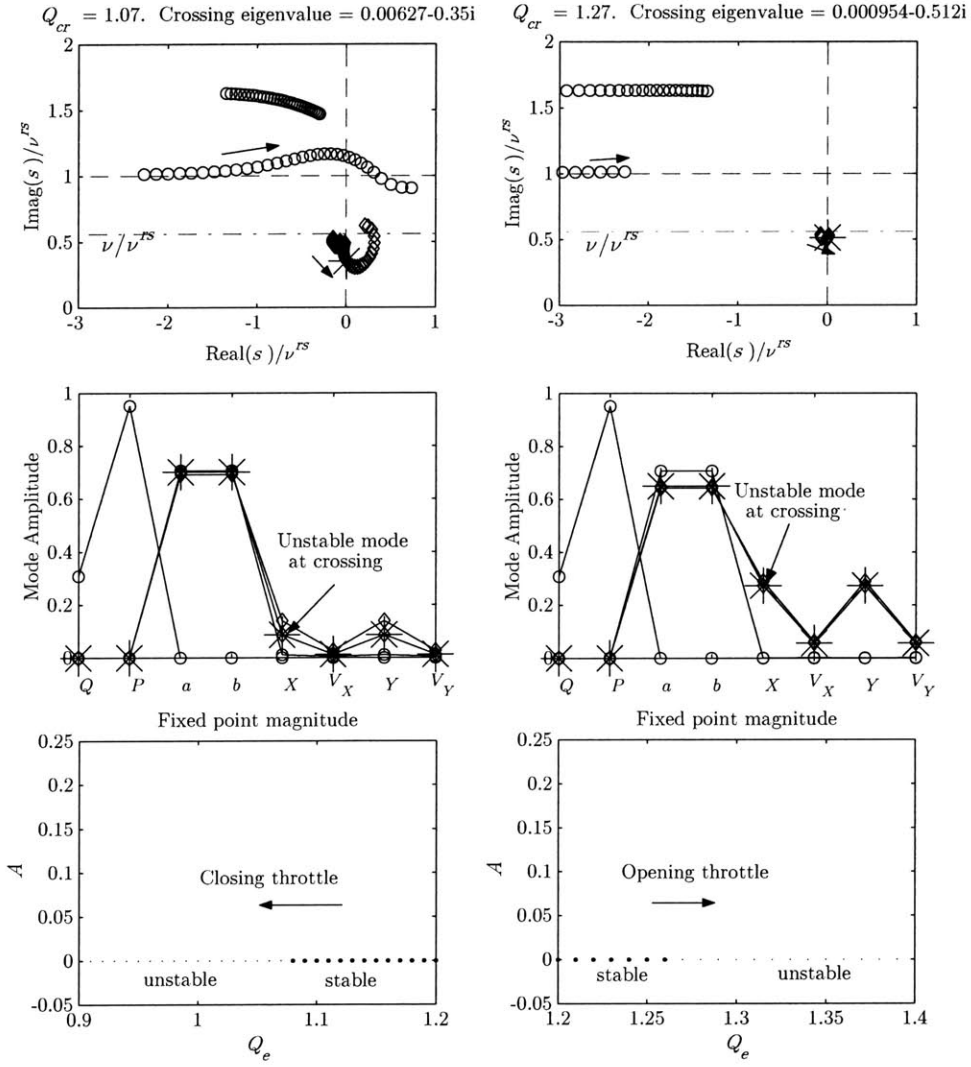

Figure 4-14: Eigenvalues and eigenvectors at crossing of stability boundary: for compressor C2, centered rotor, nominal $\nu = 0.23$, and $B = 0.1$.

same information for the case where the throttle is opened and Q_e is increased from the design point of 1.2 towards the chocked region of the characteristic. Here too a rotordynamic mode becomes unstable with the corresponding eigenvector showing larger contributions due to the structural states X and Y. Note that the scaling of different states should be taken into account when comparing their respective contributions to the mode shape. The current scaling of the dynamic equations has the aerodynamic states a and b at about an order of magnitude higher than the structural states X and Y.

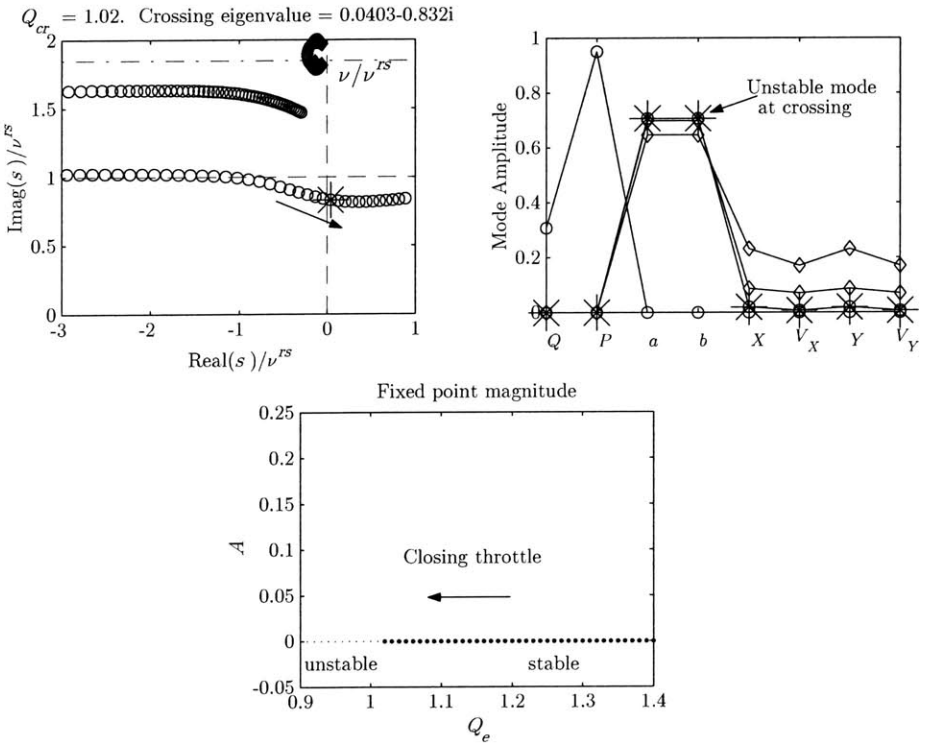

Figure 4-15: Eigenvalues and eigenvectors at crossing of stability boundary: for compressor C2, centered rotor, high $\nu = 0.75$, and $B = 0.1$.

Figure 4-15 shows the case of the higher rotor natural frequency $\nu = 0.75$ for which the stability margin is only bound on one side. In this scenario, the operating point is taken from $Q_e = 1.4$ and reduced all the way to 0.9, encountering only one crossing. Unlike the small ν case, an aerodynamic mode becomes unstable at a frequency very close to that of an uncoupled compressor. Further, the instability occurs at a much lower flow coefficient ($Q_e = 1.02$) which suggests a reduced influence

of the coupling.

4.3.2 Case of Off-centered Rotor

Typical Values of Coupling (χ)

In this case, we consider one scenario involving compressor C2 with nominal ν and same coupling used in the centered rotor case $\chi = (0.5)10^{-3}$. The results depicted in Figure 4-16 show that, in this case, there is only one stability boundary at low flow coefficients (i.e., as the compressor is throttled to low Q_e). The instability encountered as that boundary is crossed corresponds to a rotordynamic mode becoming unstable at a frequency of 53% of ν^{rs} which is very close to the rotor's natural frequency ν. Inspection of the mode shapes at crossing reveals that the unstable mode—unlike the centered case—is coupled to the surge states (Q, P). We also show in the figure the values of the main system states (i.e., A, η, r and Θ) at the various equilibrium points encountered as we lower Q_e. Recalling the aerodynamic force results obtained in Chapter 3 (see for example Figure 3-11), we note that the movement of the equilibrium points is consistent with the increase of aerodynamic forces as Q_e is reduced towards the peak of the compressor characteristic. In addition, the phase relation between the flow nonuniformity and the tip-clearance asymmetry discussed earlier in Chapter 3 is also maintained.

Very High Values of Coupling (χ): Existence of Multiple Fixed Points

It is interesting to observe—despite the lack of a clear practical application—that at very high values of χ, several branches of equilibrium points may appear, forming a complex picture of the stability of these equilibria such as the two examples shown in Figures 4-17 and 4-18. Although compressor C1 is the basis of these two examples, compressors C2 and C3 displayed similar behavior at very high values of χ, especially in the highly supercritical range of the rotor's natural frequency (e.g., in the neighborhood of ν^{rs}). In reference to Figure 4-12, these observations indicate that

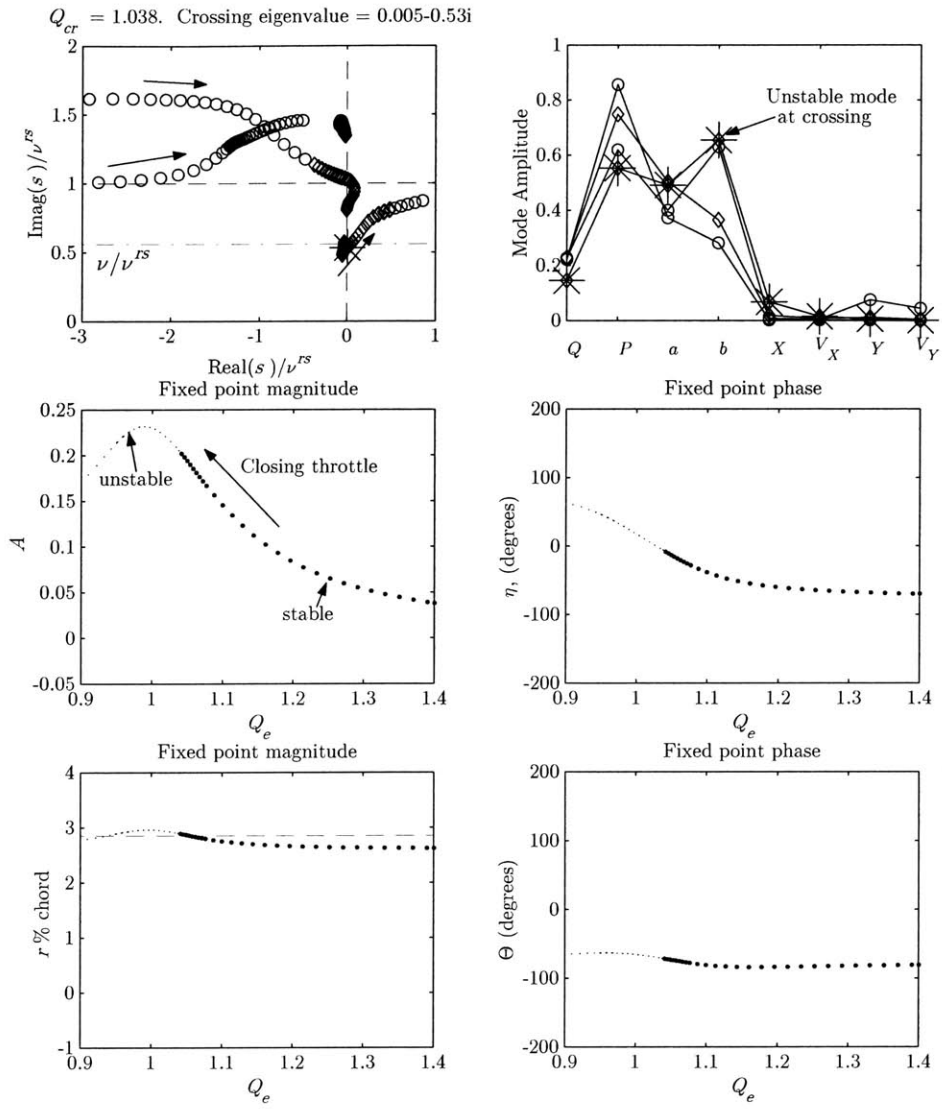

Figure 4-16: Eigenvalues and eigenvectors at crossing of stability boundary: for compressor C2, centered rotor, nominal $\nu = 0.23$, and $B = 0.1$.

the stability boundary established in that figure can not be extended to very large values of χ, since no single stability boundary can be established for the multiple equilibrium points that can exist in that region.

4.4 Summary and Discussion

The parametric studies presented in this chapter establish the significance of the interaction between aerodynamics and rotordynamic in determining the overall, coupled

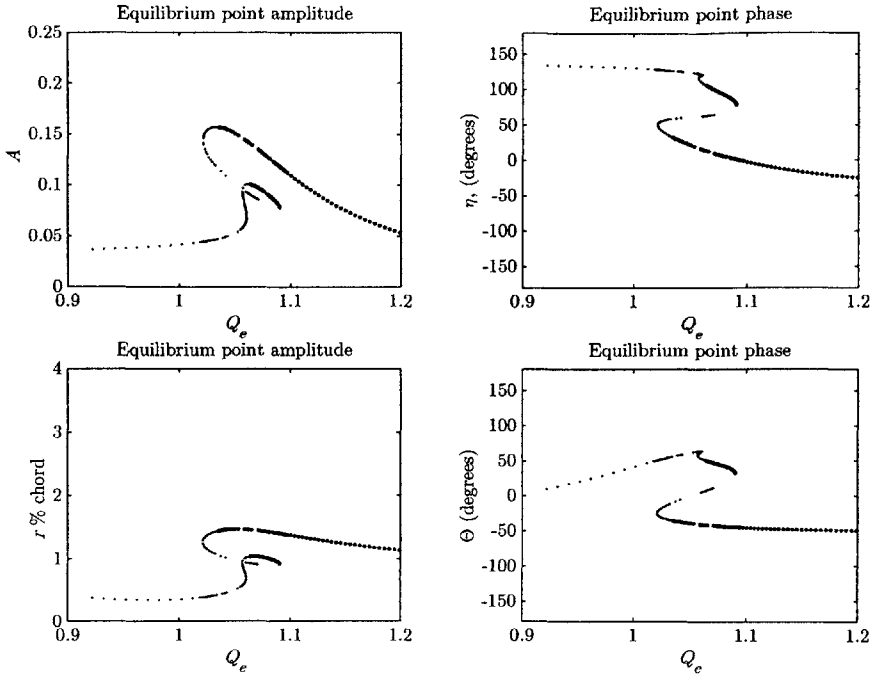

Figure 4-17: Multiple equilibrium points at high coupling: compressor C1, $\chi = 0.01$, $\nu = 0.23$, and $B = 0.1$.

system stability. We summarize the overall stability picture of the coupled system in the schematic shown in Figure 4-19 together with the following conclusions.

- The coupling changes the nature of overall stability picture in that it creates a stability margin with two bounds, one on each side of the design operating point.
- As the coupling is increased, these two bounds move closer to the design point resulting in a smaller stable operating range.
- Locally, the mode that loses stability upon crossing either of the two boundaries is mostly rotordynamic (except when the rotor's natural frequency is very high and the coupling impact is minimal). Nevertheless, we expect rotating stall to appear soon after crossing the low flow boundary as the growing rotordynamic instability promotes larger flow nonuniformity. This, however, can not be shown from the linearized analysis, and requires examining the post-instability behavior of the system—the subject of the next chapter.

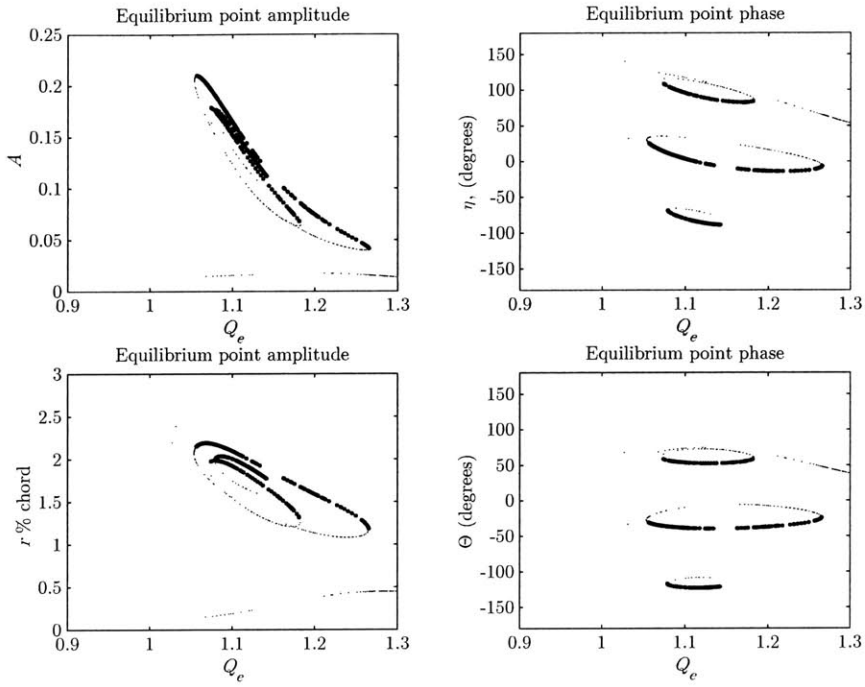

Figure 4-18: Multiple equilibrium points at higher coupling: compressor C1, $\chi = 0.03$, $\nu = 0.23$, and $B = 0.1$.

- Highly supercritical rotors tend to be more susceptible to fluid-induced instabilities. This is confirmed by the above results and is consistent with observations (Ehrich [21]).
- Variation of the rotor's natural frequency (from supercritical to subcritical) stabilizes the rotor and thus reduces the overall destabilizing effect of the coupling. This variation takes place gradually except in the neighborhood of the rotating stall frequency and for operating points close to the peak of the characteristic. In such cases (except for the axial liquid pump C4), rotors with $\nu/\nu^{rs} < 1$ tend to retain their stability only for a very small further reduction in flow coefficient.
- This gain in stability margin is reversed in the case of the axial liquid pump where rotors with $\nu/\nu^{rs} > 1$ retain their stability at operating points to the left of the peak. In addition, the gain in stability margin in this case is finite, Figure 4-6.
- In general, introducing a fixed rotor deflection has a stabilizing effect on the coupled system in that it restricts the movement of the rotor and thus prevents

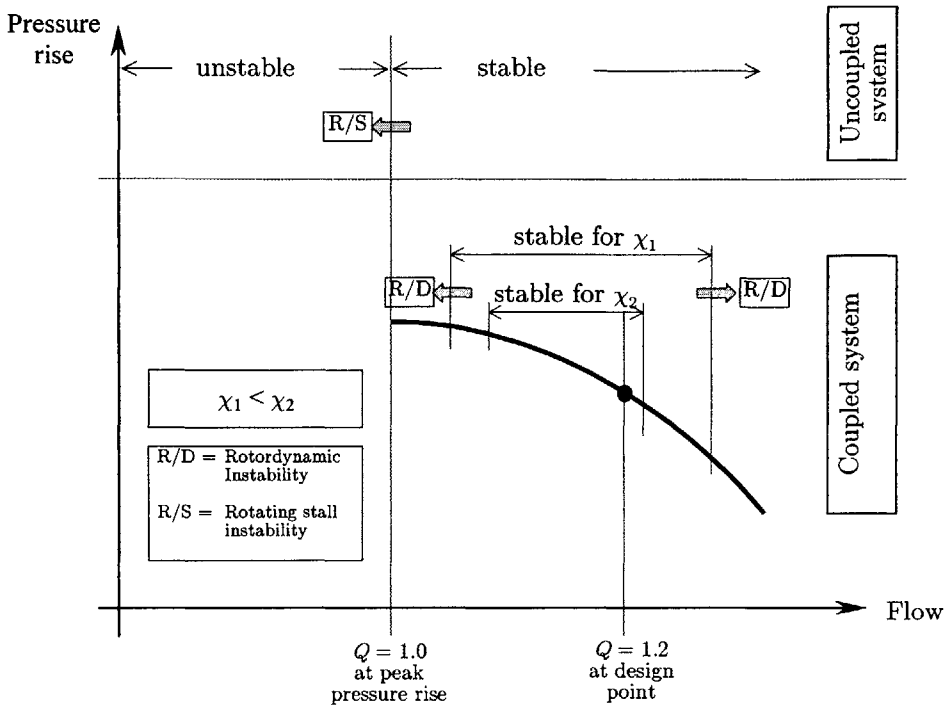

Figure 4-19: Schematic depiction of stability boundaries on the compressor map.

whirl-like disturbances that, in turn, produce rotating flow nonuniformities.

- For compression systems in the same class as C1, C2 and C3, a design parameter space is identified in which the effects of all the relevant system parameters are captured, and in which the stability boundaries for any compressor in this class are roughly the same. This parameter space is defined by the ratio of rotordynamic to aerodynamic uncoupled frequencies, ν/ν^{rs} on one hand and the product of the two coupling parameters, $\psi_{c\varepsilon}\chi$, on the other, with the operating point Q_e as the third parameter.

CHAPTER 5

POST-INSTABILITY BEHAVIOR

A numerical survey of the nonlinear post-instability behaviour of the baseline model is presented in this chapter. First, we present numerical simulations which demonstrate the different modes of instability encountered as the coupled system crosses the stability boundaries described in the previous chapter. Also through a series of simulations, we show an example of how the coupling can alter the nature of the post-instability behavior by forcing the system into a rotating stall mode instead of the surge mode known to be dominant for the uncoupled system with the same set of parameters. We end this chapter by presenting an overview of the map of post-instability behavior for both small and large values of the B parameter.

5.1 Demonstration of Post-Instability System Responses

In order to demonstrate the different modes of instability that the coupled system can exhibit, we consider one of the prototype compressors; namely C2, operating at a steady equilibrium point, say the design point $Q_e = 1.2$. We numerically integrate the nonlinear baseline model equations in nondimensional time to obtain the system response to either a set of initial conditions or to a step change in throttle setting. The numerical integrations are carried out in the computational environment of

MATLAB [53] and using its ODE numerical integration suite. In many cases, different integration routines, such as ODE45, ODE23s and ODE15s, are used to generate the same scenario in order to increase confidence in the results and eliminate the possibility of numerical artifacts.

5.1.1 Aerodynamic and Rotordynamic Instabilities

We now present simulation results for three scenarios pertaining to compressor C2. We first recall that the linear analysis of this compressor with a nominal rotor natural frequency of $\nu = 0.23$ and a value of coupling $\chi = (0.5)10^{-3}$, as shown in Figures 4-1 and 4-14, predicted that the system is stable for operating points within $1.07 < Q_e < 1.27$.

The first simulation we present here corresponds to crossing the upper boundary at $Q_e = 1.27$. Figure 5-1 shows the phase plane and time histories as the system is taken from the design point at $Q_e = 1.2$ to $Q_e = 1.32$ through a step change in the throttle. We observe that the surge states shift smoothly to the new operating point and remain there, while the rotor deflection r grows with time in a forward whirl motion until it is limited by the rotor stiffness nonlinearity. In addition, a small flow nonuniformity ($A \approx 0.025$) is associated with this final deflection. The last row of sub-plots shows the ratio of whirl frequency $\dot{\Theta}$ to flow nonuniformity frequency $\dot{\eta}$; the radial (restoring) and tangential (whirl-inducing) force amplitudes; and the tangential components of the three force contributions. It can be seen that the rotor and the flow nonuniformity are orbiting at the same frequency, (i.e., $\dot{\Theta}/\dot{\eta} = 1$), and that all the tangential contributions as well as the net tangential force are positive throughout the simulation, consistent with the positive whirl observed. In addition, these forces are also consistent with the predictions of Chapter 3 for the given deflection and operating point.

In the second simulation, shown in Figure 5-2, the lower boundary at $Q_e = 1.07$ is crossed as the system is taken from the design point $Q_e = 1.2$ to $Q_e = 1.07$ through

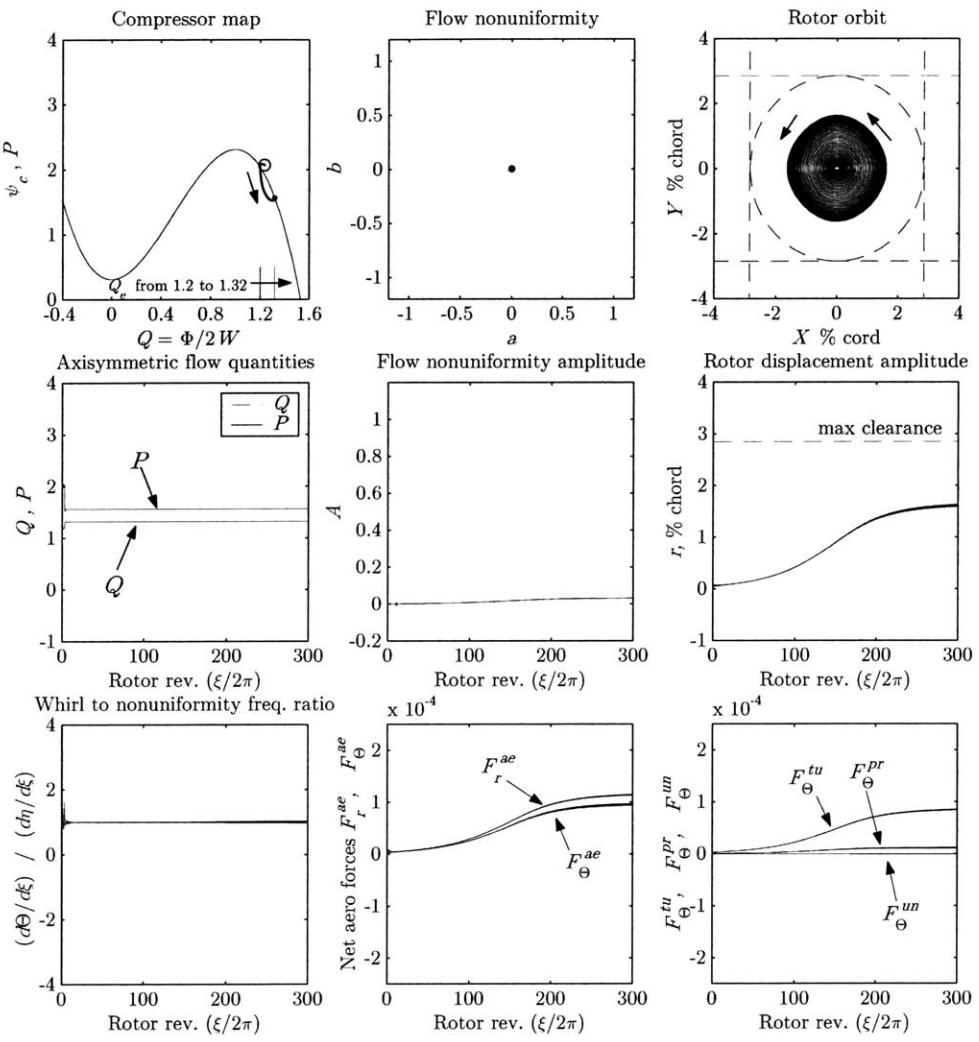

Figure 5-1: Demonstration of post-instability behavior: rotor whirl at high $Q_e = 1.32$ for compressor C2, no gravity, $\chi = (0.5)10^{-3}$, nominal $\nu = 0.23$, and $B = 0.1$.

a step change in throttling. Just as predicted by the linear analysis, a rotordynamic instability emerges in the form of forward rotor whirl. However, in this case of low flow coefficient, the amplitude of the whirl orbit is about 50% smaller than in the previous case of high flow. Further, the aerodynamic force forces are different in that the turning contribution tends to induce backward whirl while the pressure contribution (which is larger) tends to induce forward whirl. The net effect is a forward whirl motion of a smaller amplitude. Although there are no aerodynamic instabilities present at this point, we note that the flow nonuniformity is larger in amplitude ($A \approx 0.05$) than in the previous case, despite the smaller rotor deflection. This is because of

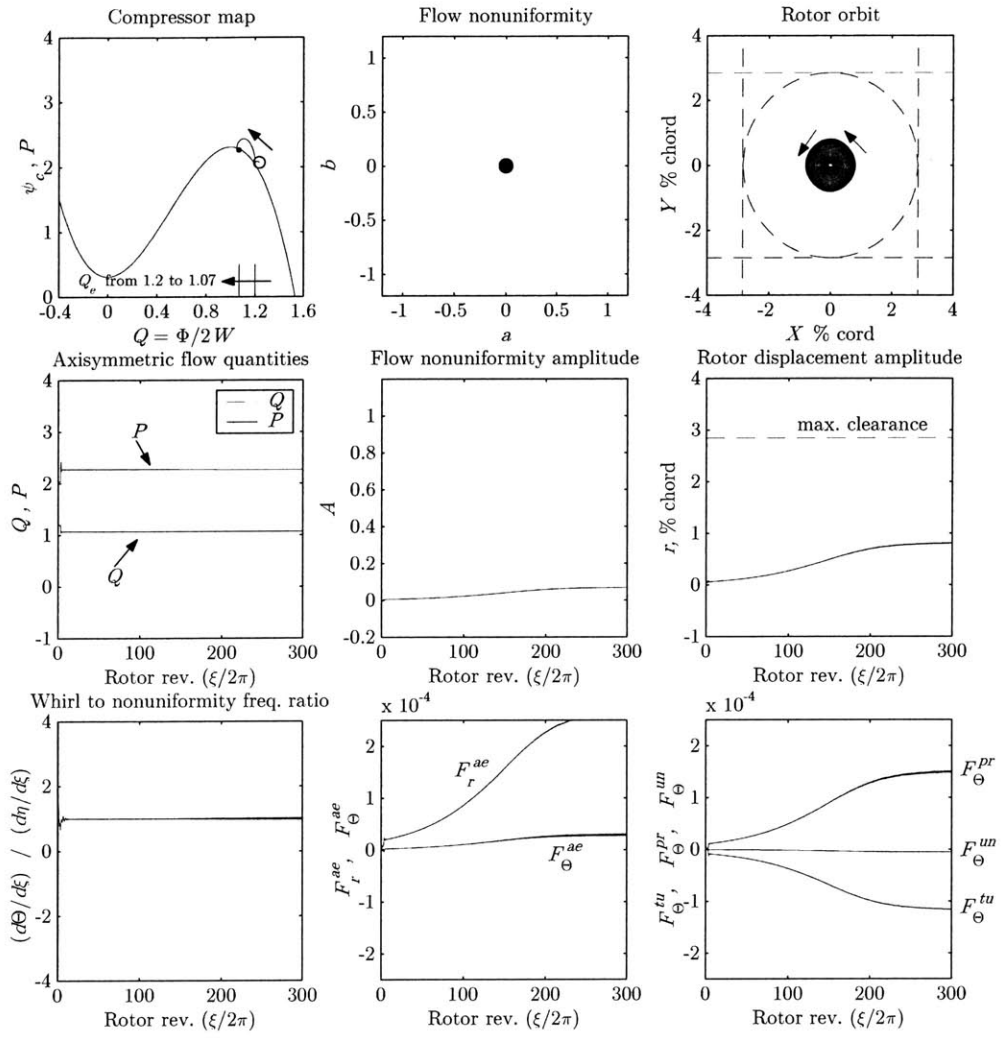

Figure 5-2: Demonstration of post-instability behavior: rotor whirl at low $Q_e = 1.08$ for compressor C2, no gravity, $\chi = (0.5)10^{-3}$, nominal $\nu = 0.23$, and $B = 0.1$.

the proximity of this operating point to the peak of the characteristic, where the compressor tends to strongly amplify nonuniformities. Both of these observations are consistent with the results presented in Chapter 3, which suggest similar trends as the operating point is moved from right to left (towards the peak of the characteristic) on the compressor map.

In the third simulation, shown in Figure 5-3, the operating point is moved from design at $Q_e = 1.2$ to $Q_e = 1.06$, a point slightly further to the left from the previous case. In this case, an aerodynamic instability arises in the form of rotating stall indicated by the large amplitude of the flow nonuniformity ($A \approx 1.0$). The rotordynamic

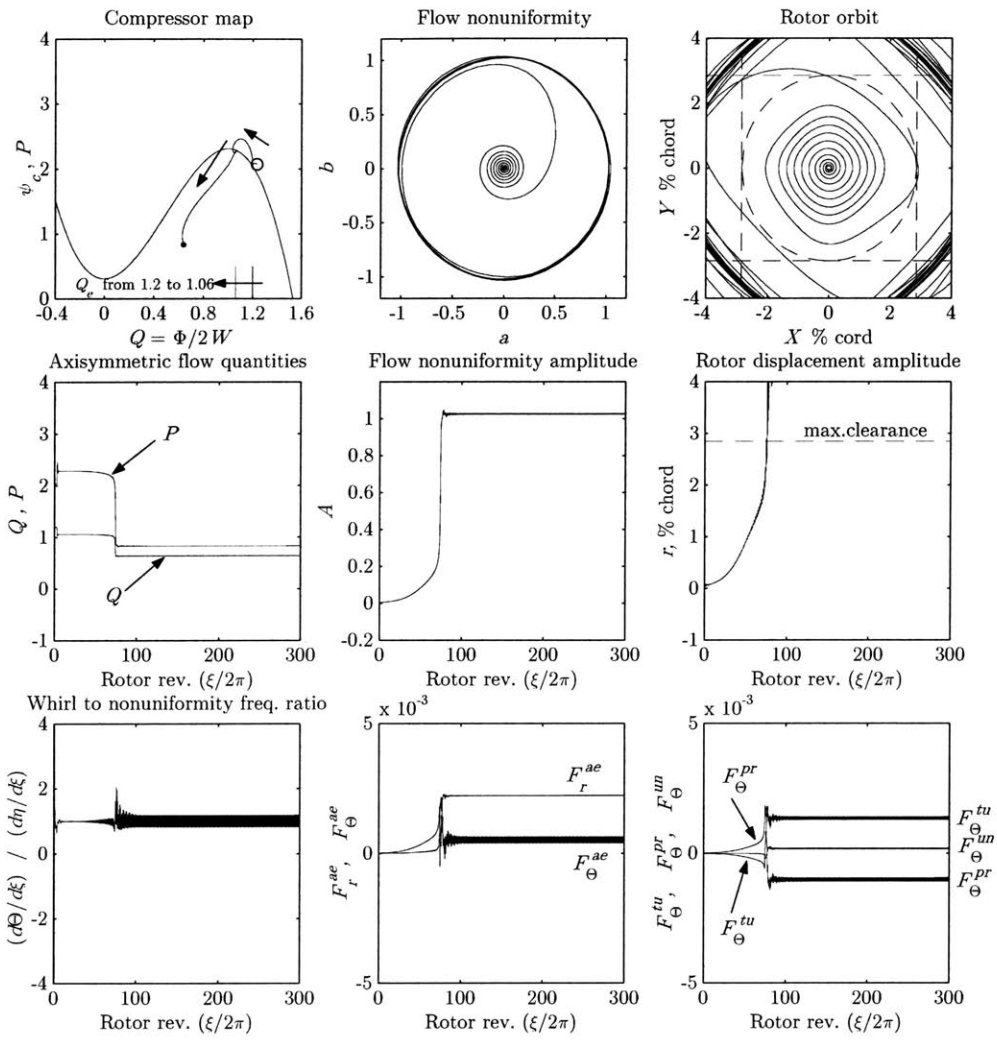

Figure 5-3: Demonstration of post-instability behavior: rotor whirl at low $Q_e = 1.08$ for compressor C2, no gravity, $\chi = (0.5)10^{-3}$, nominal $\nu = 0.23$, and $B = 0.1$.

behavior is even more violent here[1] as the aerodynamic forces are much higher due to the large amplitude of the flow nonuniformity. In the early part of the simulation, the different force contributions tend to follow a trend similar to that of the previous case. However, as the flow nonuniformity magnitude grows, the turning and pressure contributions reverse signs while net effect remains in the forward whirl direction. Finally, we note that the unsteady force contribution is very small as compared to

[1] Although the rotor deflection is larger that the maximum clearance for this system, the simulation is allowed to continue until the system approaches a final state. However, in evaluating the integrated characteristics $\bar{\psi}_c^{Cc}$ and $\bar{\psi}_c^{Cs}$, the maximum deflection is used whenever the instantaneous rotor deflection exceeds it.

the other two, largely due to the difference in their respective scaling terms χ^{tu}, χ^{pr} and χ^{un} as given in Table 3.1.

5.1.2 Coupling Alters the Post-instability Behavior

In this section, we present a series of four simulations that demonstrate how the aerodynamic-rotordynamic interaction may alter the nature of the post-instability behavior of the coupled system. The response of compression system C1 with a rotor natural frequency in the supercritical range is considered (We take $\nu = 0.44$, 25% of the nominal value). We also assign a large value of the B-parameter so that surge is the dominant mode of instability for the uncoupled system. We start by examining the stability of an operating point to the left of the characteristic peak, say at $Q_e = 0.95$. The first simulation, part (a) in Figure 5-4, shows the system response to initial conditions with no coupling, i.e., $\chi = 0.0$.

As expected, the uncoupled compressor displays a surge instability where sustained oscillations in axisymmetric flow and pressure are dominant. The second simulation, part (b) in Figure 5-4, shows the system response in an identical situation except for the introduction of coupling by setting $\chi = (0.5)10^{-3}$. In this case, the system response exhibits one surge-like cycle (due to the large initial conditions) but goes into rotating stall as the the ultimate form of post-instability behavior. Equilibrium points further to the left show the same change in behavior until the point $Q_e = 0.9$ is reached, Figure 5-4(c). Any further throttling gives rise to sustained surge oscillations that are slightly modified due to the interaction with the flow nonuniformity and rotor vibrations, both of which are present and large in this case, Figure 5-4(d).

Similar simulations carried out for system C2 with its nominal value of ν show that it exhibits the same behavior. In that case, rotating stall dominates until the operating point is throttled back to $Q_e = 0.86$, as opposed to 0.89 for C1.

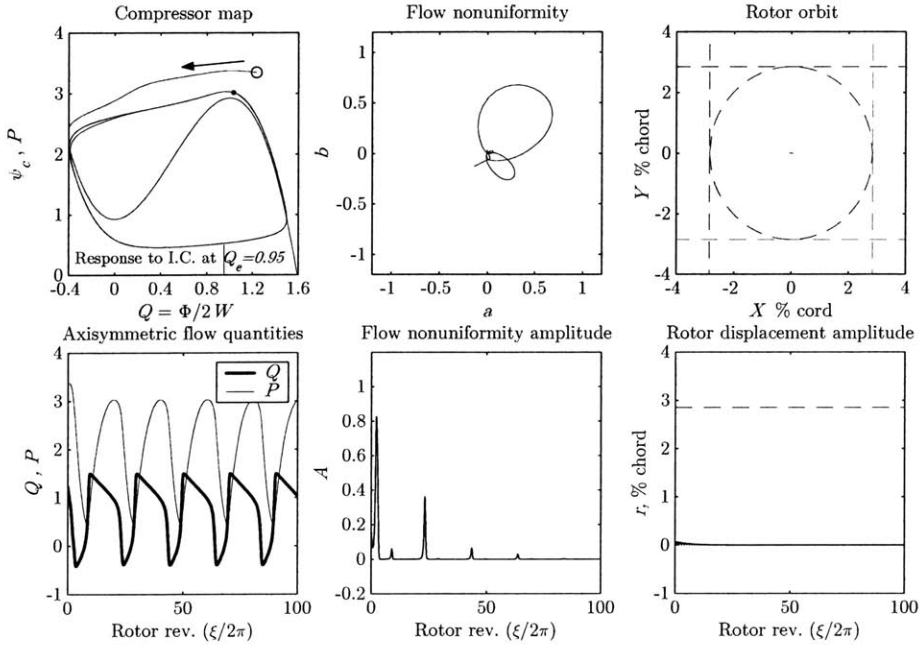

(a) Surge dominates with no coupling, $\chi = 0$

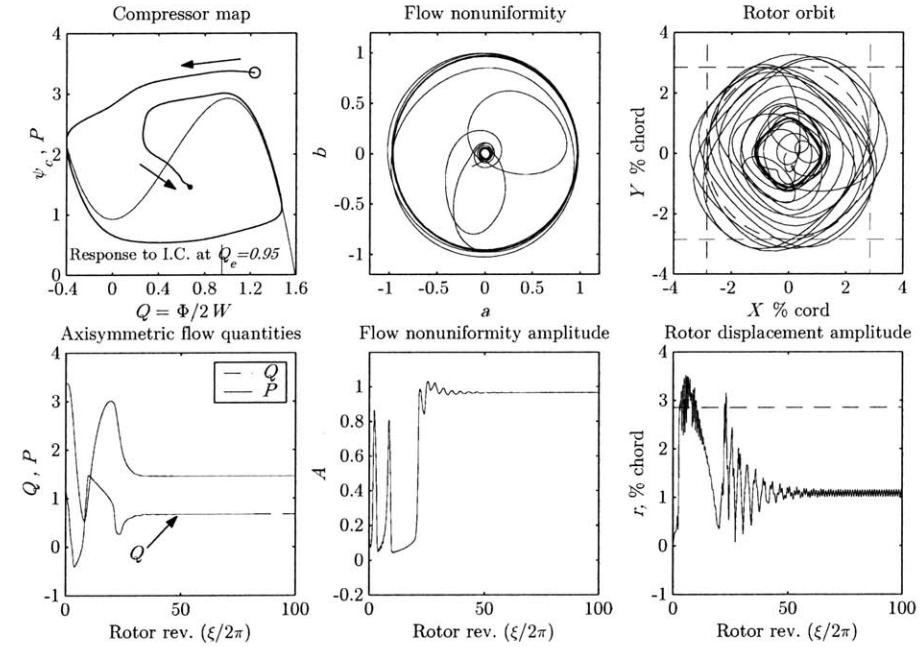

(b) Rotating stall replaces surge with coupling, $\chi = (0.5)10^{-3}$

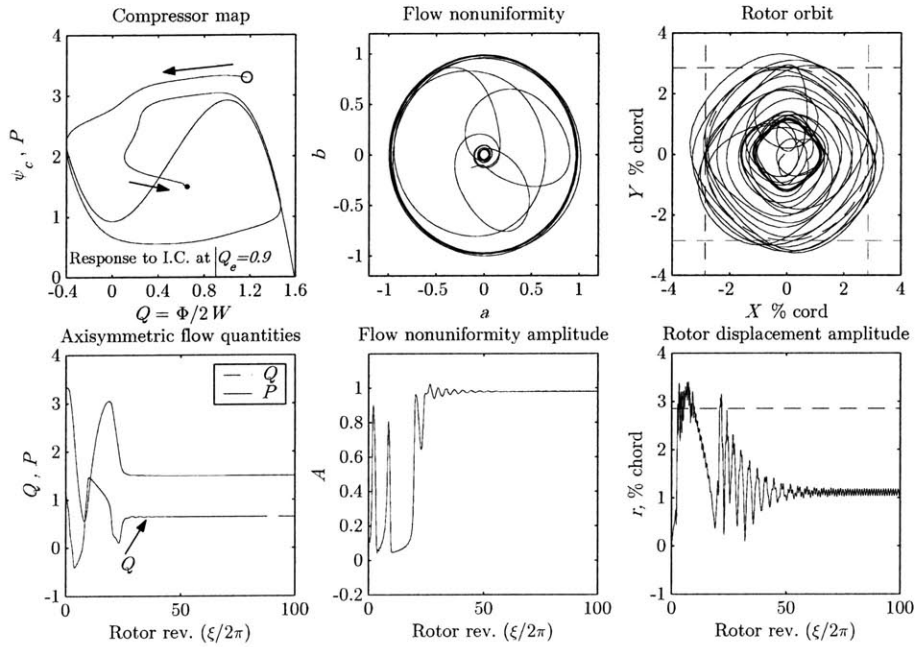

(c) Rotating stall persists with coupling $\chi = (0.5)10^{-3}$ until Q_e is reduced to 0.90

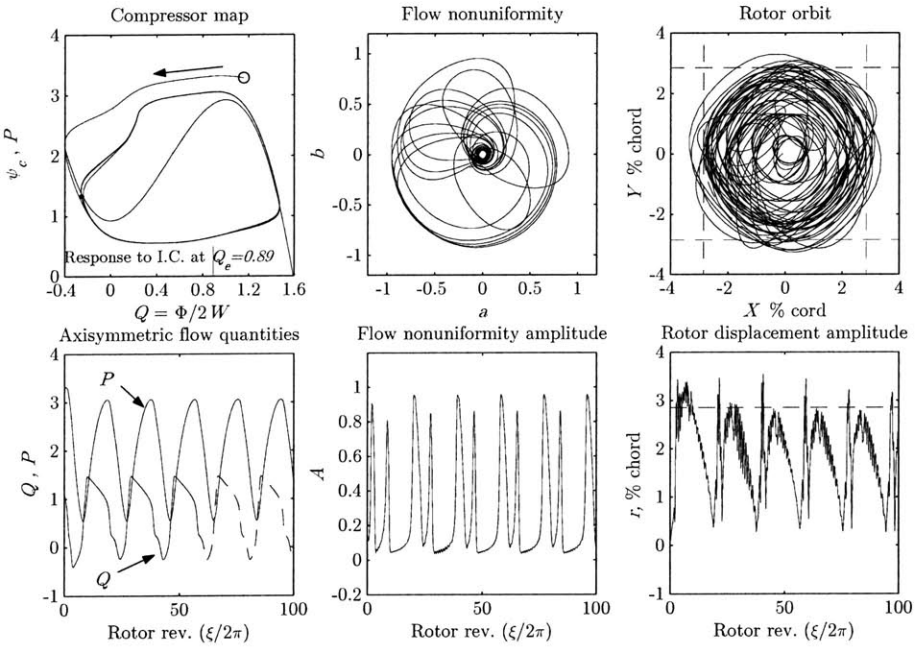

(d) Surge is finally reached with coupling $\chi = (0.5)10^{-3}$ at $Q_e = 0.89$

Figure 5-4: Demonstration of how coupling alters post-instability behavior: Response to initial conditions for compressor C1, centered rotor, $\nu = 0.44$ (25% of nominal), and $B = 1.0$.

5.2 Overall Map of Post-Instability Behavior

The results presented so far in this chapter suggests that the post-instability behavior of the coupled system may, in certain regions of the parameter space, exhibit remarkable differences from either the uncoupled compressor or the uncoupled rotor. Therefore, we set out in this section to construct bifurcation maps of the post-instability behavior for a few cases of parameter combinations. We divide this exercise into two main groups: low B-parameter systems where only rotordynamic and rotating stall type instabilities are expected, and high B-parameter systems where surge is also possible. In each group, we construct a bifurcation map with the compressor operating point Q_e as a bifurcation parameter (which is equivalent to using the throttling coefficient γ). We also compare different values of coupling parameters χ, but restrict the rotor natural frequency to the supercritical region where coupling effects are observed the most.

5.2.1 Low B-Parameter

We consider the prototype compression system C2 with $B = 0.1$ and nominal $\nu = 0.23$, and compare the two cases of moderate coupling ($\chi = (0.5)10^{-3}$) and no coupling ($\chi = 0.0$).

Figure 5-5 shows the various limit cycles that exist throughout the operating range in terms of the maximum and minimum of sustained oscillations in Q, and the peak amplitude of the nonuniformity A and rotor deflection r. Starting from operating points with high flow coefficient, say $Q_e = 1.4$, and following the coupled case first, we observe that the post-instability behavior is mainly rotordynamic, characterized by a (forward) whirling motion with a large rotor deflection and a relatively small aerodynamic nonuniformity, consistent with the simulation shown in Figure 5-1. As the operating point is moved to the left (towards the peak of the characteristic) the amplitude of rotor whirl decreases while that of the flow nonuniformity remains small and constant. This is so because the compressor tends to generate larger distortions

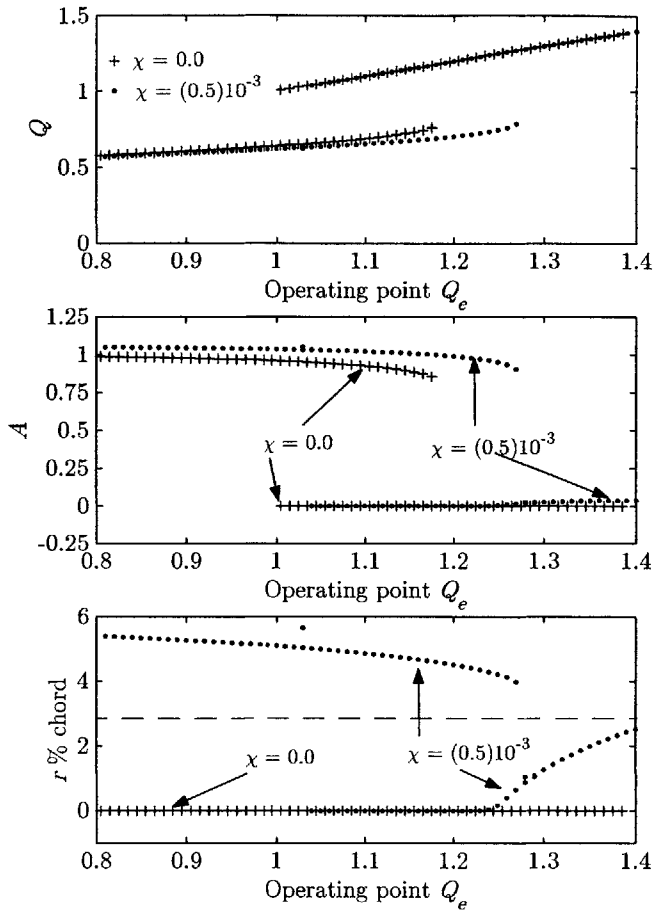

Figure 5-5: Bifurcation map for compressor C2, centered rotor, $\chi = 0.0$, $(0.5)10^{-3}$, nominal $\nu = 0.23$, and $B = 0.1$.

per unit rotor deflection as it operates closer to the characteristic peak. Further reduction in Q_e eventually results in the disappearance of the instability and the convergence to a stable equilibrium point around $Q_e = 1.27$. The gradual decrease in the amplitude of rotor whirl and the lack of hysteresis indicate that the bifurcation at $Q_e = 1.27$ is of the supercritical type. Further throttling moves the operating point through a series of locally stable operating points that extend between $1.07 < Q_e < 1.27$. Once below $Q_e = 1.07$, aerodynamic instability dominates in the form of rotating stall. The large aerodynamic nonuniformity associated with rotating stall produces large forces in the rotor and results in a large rotordynamic response. The presence of a large hysteresis at $Q_e = 1.07$ indicates that the bifurcation is of the more harmful, subcritical type. The size of the hysteresis in this case is about 20% of

peak flow coefficient. In contrast, the uncoupled case exhibits only an aerodynamic instability in the form of rotating stall. The uncoupled compressor loses its stability at $Q_e = 1.0$ as expected, and the size of the hysteresis is about 18%.

From these results, it can be seen that the coupling not only increases the hysteresis (by 2% in this case), but also renderes the whole operating range unstable for large disturbances.

5.2.2 High B-Parameter

Motivated by the results of Section 5.1.2, we return to system C1 and consider again a large value of $B = 1.0$ and a supercritical rotor with $\nu = 0.44$ (25% of the nominal value). We then perform a set of three simulation-based experiments to construct a picture of the limit cycle responses that exist at different operating points. We note that the post instability behavior here depends not only on the parameters B, ν and the operating point Q_e, but also on the size of disturbances the system is subjected to at each operating point (i.e., initial conditions of the simulation).

In the first experiment, whose results are shown in Figure 5-6, we present the uncoupled case, $\chi = 0$, where the main mode of instability is shown to be deep surge[2] In this experiment, we start from an equilibrium point with a small flow coefficient, $Q_e = 0.8$, and impose a large initial condition ($Q(0) = 1.5Q_e$) where the mode of instability is, indeed, deep surge. As we open the throttle to higher flow coefficients, we note that deep surge persists until stable operation is achieved at $Q_e = 1.0$.

The second experiment, Figure 5-7, is performed with a value of coupling parameter $\chi = (0.5)10^{-3}$, equal to that used in most previous simulations. Here, we start from an equilibrium point with a small flow coefficient, $Q_e = 0.8$, and impose a small initial condition ($Q(0) = 1.05Q_e$). In this case, the compressor goes into ro-

[2]Deep surge and classic surge are two types of surge instabilities encountered in axial compression systems, [31], [54]. In deep surge, sustained oscillations in axisymmetric flow are accompanied by small flow nonuniformities observed over a limited portion of the cycle. On the other hand, in classic surge, oscillations in axisymmetric flow are accompanied by larger flow nonuniformities over a significant part of the cycle.

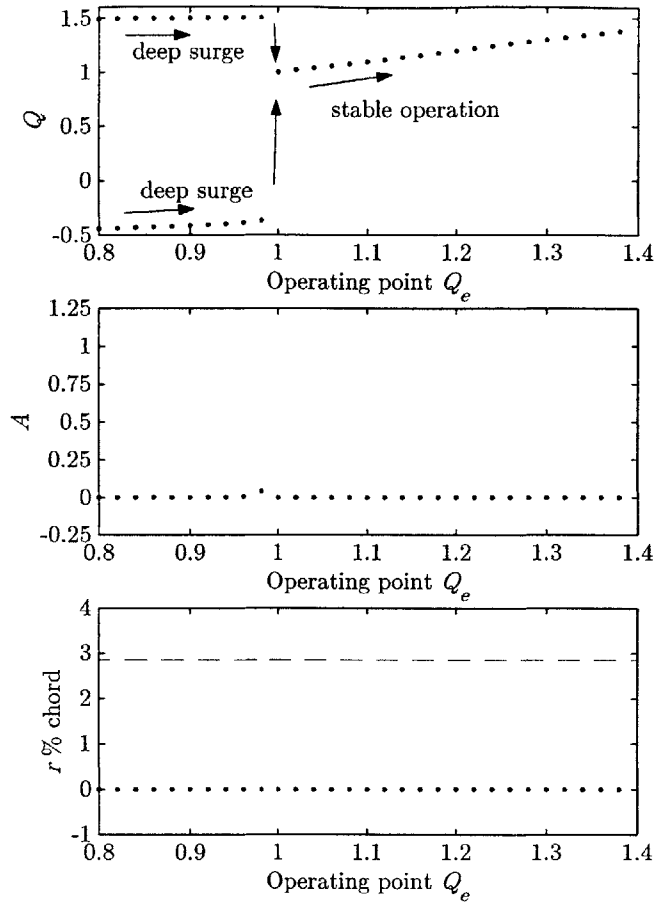

Figure 5-6: Map of post-instability behavior of compressor C1: deep surge for uncoupled case, $\chi = 0$, $\nu = 0.44$, and $B = 1.0$.

tating stall accompanied by a relatively large deflection of the rotor. As we open the throttle, the same behavior persists until stable operation is achieved at $Q_e = 1.077$, more than 5% higher than the linear stability boundary of 1.02 which reflects the hysteresis involved in recovering from rotating stall. It can also be seen that for this relatively high value of ν there exists no rotordynamic instability at operating points with $1.077 < Q_e < 1.4$, in contrast to cases with lower values of ν, such as the results shown in Figure 5-5.

In the third experiment, we start again from $Q_e = 0.8$ and impose a large initial condition ($Q(0) = 1.5Q_e$). In contrast to the uncoupled case, the compressor goes into classic surge where rotating stall is present over most of the cycle, accompanied by a very large rotor deflection due to the very large aerodynamic forces resulting

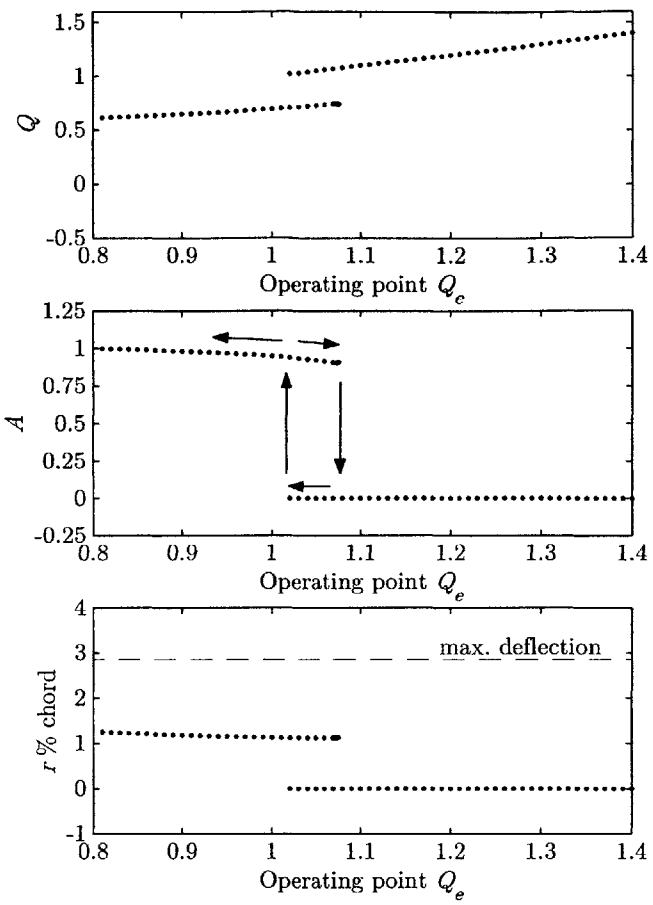

Figure 5-7: Map of post-instability behavior of compressor C1: rotating stall for coupled case, small initial conditions in Q, $\chi = (0.5)10^{-3}$, $\nu = 0.44$, and $B = 1.0$.

from the coexistence of surge and rotating stall. As we open the throttle to higher flow coefficients, surge disappears at about $Q_e = 0.9$ (as suggested by the series of simulations in Figure 5-4). Now, throttling the compressor back to lower flow coefficients does not produce surge again unless large disturbances are imposed (not the case in this figure). At higher flow coefficients, the transition from rotating stall to stable operation is similar to that observed in the second experiment, Figure 5-7.

In closing, we state that the above results do not constitute a complete bifurcation map of the system post-instability behavior. Nevertheless, they shed some light on several important aspects of the impact of aerodynamic-rotordynamic interaction on the complex behavior of these systems.

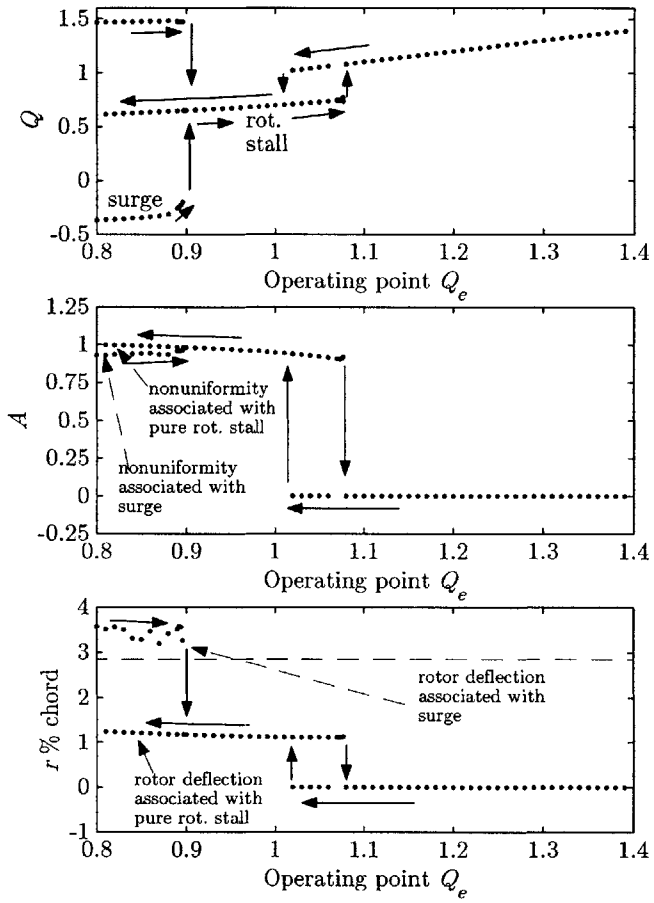

Figure 5-8: Map of post-instability behavior of compressor C1: classic surge and rotating stall for coupled case, large initial conditions in Q, $\chi = (0.5)10^{-3}$, $\nu = 0.44$, and $B = 1.0$.

CHAPTER 6

CONCLUSIONS

6.1 Summary and Conclusions

In this thesis, we addressed the interaction between the aerodynamics and rotor structural vibrations in axial compression systems. The work presented involved modeling of the coupling between the aerodynamic and rotordynamic domains, a comprehensive parametric investigation of the linearized stability of the coupled system, and a survey of the impact of coupling on the post-instability behavior.

Summary of the Modeling Efforts

The baseline model developed and used in this thesis is comprised of a single-harmonic, two-dimensional version of the Moore-Greitzer model that describes the flowfield and a simple, mass-spring-damper Jeffcott-type model of the rotor that describes the rotordynamics. The coupling between the fluid and structural dynamics is captured by a linear compressor sensitivity to tip clearance, and a momentum-based model of the aerodynamic forces on the rotor. Careful nondimensionalization of the overall model gives rise to a set of parameters that govern the system behavior. There are two main coupling parameters, each of which governs the influence of one domain on the other: The nondimensional sensitivity of the compressor pressure-rise characteristic to tip clearance describes the rotordynamic influence on aerodynamics, while the ratio of

fluid mass (or density) to the rotor solid mass (or density) describes the aerodynamic influence on rotordynamics.

Aerodynamic Forces on Compressor rotors

The aerodynamic force model reveals that there are three physical contributions to the total aerodynamic force on the rotor. In the presence of a flow nonuniformity, the three contributions arise, respectively, from nonuniform turning done by the blades, nonuniform hydrostatic pressure acting on the hub (directly on the rotor), and the unsteady momentum storage within the rotor blade passages. Each of the three force contributions scales with a nondimensional parameter that depends only on blade and stage geometry.

We also derived simple analytical expressions for the aerodynamic forces for a given compressor geometry, characteristics, operating point, and rotor deflection. These expressions give physical insight which establishes a link between the direction of the three force contributions and the flow nonuniformity. Consequently, the aerodynamic forces are locked to the flow nonuniformity and not to the tip-clearance asymmetry as is traditionally assumed. Using the analytical and numerical results of this force model (presented in Chapter 3), we showed that in order to predict whether the rotor tends to whirl backward or forward, all force contributions as well as the compressor operating point have to be taken into account. This is especially true close to the design operating point where the pressure and turning contributions are of comparable magnitude but different signs. The force model compares well with recently published data of aerodynamic force measurements and computational results over the narrow range of operating conditions in which they are available.

Stability of the Coupled System

Using a linearized version of the model, we studied the stability of the coupled system through a comprehensive set of parametric studies. In doing so, we determined the

regions in the parameter space where coupling has the most effect. We also shed light on the nature of the different types of instabilities that may be encountered as the stability boundaries are crossed. From these results, we conclude that the coupling generally has an adverse effect on system stability in that the stability margin for the coupled system is smaller than that of the uncoupled compressor. This adverse effect was found to be most pronounced in the cases of supercritical rotors. Further, we found that as the coupling increases this effect grows, until a coupling limit is reached. Above this limit the system becomes unstable for all operating conditions.

For typical levels of coupling, we found that the stability margin to the left of the design operating point can be reduced relative to that of the uncoupled compressor by as much as 5% to 10% in flow coefficient. In addition, at such coupling levels, the system displays another instability at operating points higher than design. This instability is mostly in the form of rotordynamic forward whirl.

The scope of these parametric studies also includes the effects of compressor geometry and characteristics, which we accounted for by considering four prototype compression systems representative of low and high pressure-rise compressors as well as subcritical and supercritical rotors. Among the prototype systems studied is an axial liquid pump for which the large difference in characteristics and coupling parameter values translated into several qualitative and quantitative changes in the overall stability picture.

Post-instability behavior

Having identified an upper and lower linear stability boundary, we employed numerical simulations to study the post-instability behavior of the system. The instability is of rotordynamic nature (forward rotor whirl) at typical coupling levels and as the operating point is moved to higher flow coefficients. On the other side of the stability margin, we showed that a rotordynamic instability also arises at operating points just past the stability boundary. But, aerodynamic instabilities dominate for any further throttling of the compressor. In such cases, the rotordynamic response

is very violent owing to the large forces associated with aerodynamic instabilities. Also using numerical simulations, we identified examples in which the coupling has a noticeable effect on the dominant post-instability mode. We showed that the coupled system with a large B parameter exhibited rotating stall within an operating range of about 10% to the left of the peak where surge is known to be the dominant mode of instability of the uncoupled compressor.

Finally, we surveyed a wide range of the operating range and constructed maps of the overall post-instability picture for two representative cases.

6.2 Recommendations for Future Rersearch

Since this work represents the first treatment of the aerodynamic-rotordynamic interaction in axial compression systems, we sought the simplest possible models that capture the phenomena of interest while remaining tractable. Such models are usually the best tools to explore basic phenomena and gain physical insight. Nevertheless, more sophisticated models may be constructed in order to build on the understanding developed in this thesis.

In order to obtain a quantitative representation of an actual gas turbine or a jet engine, several modeling extensions may be included. A higher order flowfield description can be considered by including more than one mode in the Fourier series representing the flow coefficient. Further, a more sophisticated representation of the compressor sensitivity to tip clearance can be incorporated to capture the shift in the peaks of the pressure-rise characteristic (in contrast to the vertically aligned peaks of this model). Other aerodynamic forces should also be accounted for—with those due to axial turbines that may be mounted on the same rotor being the most important. Other forces that may be considered include those due to seals and journal bearings. Several rotordynamic effects that were briefly described in Chapter 2, such as internal rotor damping with hysteresis and parametric excitaion due to shaft stiffness orthotropy, should be considered. In particular, the forced response of the

coupled system (e.g., to imbalance) should also be investigated and compared to that of uncoupled rotors.

The regions of the multi-dimensional parameter space of such systems that have been considered in this thesis reveal few desirable effects of the coupling. Nevertheless, the case of the axial liquid pump indicates that such a favorable interaction is, in principle, feasible. Further exploration should be carried out in order to exploit such effects and utilize them in the design of more stable machines.

A full understanding of the post-instability dynamics of the system will require a detailed bifurcation analysis. Simulation results show that under most conditions the loss of stability is subcritical (i.e., the bifurcation map shows hysteresis). In addition, the transition from rotating stall to surge appears to involve a crisis-type bifurcation.

Active control of aerodynamic instabilities using magnetic bearings have been proposed and assessed by several researchers. The model and results developed in this thesis may be used as the basis for designing and carrying out such experiments. Finally, perhaps in the course of such experiments, the stability boundaries and post-instability behaviors predicted by this model can be validated.

APPENDIX A

HIGHER ORDER FLOWFIELD MODEL

In this appendix, we give further details pertaining the flowfield model developed in Chapter 2 and provide expressions for the integrated characteristics obtained when considering higher harmonics in the Fourier series solution used in the Galerkin procedure.

The main equations describing the flowfield were given in Eqs. (2.22), (2.31) and (2.32), which are listed here in the rescaled version as

$$\frac{dQ}{d\xi} = \frac{S}{2\mathcal{L}}\left[\bar{\psi}_{cN}^{C} - P\right] \tag{A.1}$$

$$\frac{da_n}{d\xi} = \frac{n\lambda}{m+n\mu}\left[\frac{S}{2\lambda}\bar{\psi}_{cN}^{Ccn} - nb_n\right] \tag{A.2}$$

$$\frac{db_n}{d\xi} = \frac{n\lambda}{m+n\mu}\left[\frac{S}{2\lambda}\bar{\psi}_{cN}^{Csn} + na_n\right] \tag{A.3}$$

where $n = 1, 2, \ldots, N$ is the mode number and N is the total number of modes considered in the Fourier series. Since our goal in this thesis is to develop the simplest possible model that describes the phenomena of interest, the baseline model used in this thesis is based on the case where $N = 1$. However, including higher harmonics should improve the accuracy of the flowfield description and should therefore be considered whenever precise, machine-specific predictions are sought.

Using the same compressor characteristic ψ_c and rescaling introduced in Section

2.3, we may carry out integrations and write the above flowfield equations for any $N > 1$ which will produce $2N + 1$ equations. Below we provide a sample (Maple V) code that would generate such results. We set $N = 5$ in this code just for demonstration, while higher modes can be obtained by setting N appropriately and adding the corresponding expressions towards the end.

```
> restart:
> assume(n,integer):

Choose total number of modes to include in Fourier series, N

> N := 5:
> psi_c := psi_c0 + 1 + 3*(q-1/2) - 4*(q-1/2)^3 +
  psi_ce*r*cos(theta-Theta):
> q := Q + sum(a[n] * cos(n*theta) + b[n] * sin(n*theta), n =1..N);
```

$$q := Q + a_1 \cos(\theta) + b_1 \sin(\theta) + a_2 \cos(2\,\theta) + b_2 \sin(2\,\theta) + a_3 \cos(3\,\theta) + b_3 \sin(3\,\theta) + a_4 \cos(4\,\theta) + b_4 \sin(4\,\theta) + a_5 \cos(5\,\theta) + b_5 \sin(5\,\theta)$$

```
Evaluate all integrated characteritics

> psi_bar_C_N    :=
  collect(expand(1/(2*Pi)*int(psi_c,theta=0..2*Pi)),Q):

> psi_bar_CcN_1 :=
  collect(expand((1/(Pi)*int(psi_c*cos(theta),theta=0..2*Pi))),Q):
> psi_bar_CsN_1 :=
  collect(expand((1/(Pi)*int(psi_c*sin(theta),theta=0..2*Pi))),Q):

> psi_bar_CcN_2 :=
  collect(expand((1/(Pi)*int(psi_c*cos(2*theta),theta=0..2*Pi))),Q):
> psi_bar_CsN_2 :=
  collect(expand((1/(Pi)*int(psi_c*sin(2*theta),theta=0..2*Pi))),Q):

> psi_bar_CcN_3 :=
  collect(expand((1/(Pi)*int(psi_c*cos(3*theta),theta=0..2*Pi))),Q):
> psi_bar_CsN_3 :=
  collect(expand((1/(Pi)*int(psi_c*sin(3*theta),theta=0..2*Pi))),Q):

> psi_bar_CcN_4 :=
  collect(expand((1/(Pi)*int(psi_c*cos(4*theta),theta=0..2*Pi))),Q):
> psi_bar_CsN_4 :=
  collect(expand((1/(Pi)*int(psi_c*sin(4*theta),theta=0..2*Pi))),Q):

> psi_bar_CcN_5 :=
  collect(expand((1/(Pi)*int(psi_c*cos(5*theta),theta=0..2*Pi))),Q):
> psi_bar_CsN_5 :=
  collect(expand((1/(Pi)*int(psi_c*sin(5*theta),theta=0..2*Pi))),Q):
```

We also provide expressions for the case of $N = 2$, obtained using the above code,

as follows

$$q(\theta,\xi) = Q(\xi) + a_1(\xi)\cos\theta + b_1(\xi)\sin\theta + a_2(\xi)\cos 2\theta + b_2(\xi)\sin 2\theta \tag{A.4}$$

and,

$$\begin{aligned}
\bar{\psi}_{c2}^{C} &= \frac{1}{2\pi}\int_0^{2\pi} \psi_c \, d\theta \\
&= \psi_{c0} - 4Q^3 + 6Q^2 - 6\left[a_1^2 + b_1^2 + a_2^2 + b_2^2\right] Q \\
&\quad + 3\left[a_1^2 + b_1^2 + a_2^2 + b_2^2 - a_2(a_1^2 - b_1^2) - 2a_1 b_1 b_2\right]
\end{aligned} \tag{A.5}$$

$$\begin{aligned}
\bar{\psi}_{c2}^{Cc1} &= \frac{1}{\pi}\int_0^{2\pi} \psi_c \, \cos(\theta) \, d\theta \\
&= -12a_1 Q^2 - 12\left[-a_1 + a_1 a_2 + b_1 b_2\right] Q \\
&\quad - 3a_1\left[a_1^2 + b_1^2 + 2(a_2^2 + b_2^2 - a_2)\right] + 6b_1 b_2 + \psi_{c\varepsilon} X
\end{aligned} \tag{A.6}$$

$$\begin{aligned}
\bar{\psi}_{c2}^{Cc2} &= \frac{1}{\pi}\int_0^{2\pi} \psi_c \, \cos(2\theta) \, d\theta \\
&= -12a_2 Q^2 - 12\left(\frac{1}{2}(a_1^2 - b_1^2) - a_2\right) Q \\
&\quad - 3\left[a_2\left(2(a_1^2 + b_1^2) + a_2^2 + b_2^2\right) - a_1^2\right]
\end{aligned} \tag{A.7}$$

$$\begin{aligned}
\bar{\psi}_{c2}^{Cs1} &= \frac{1}{\pi}\int_0^{2\pi} \psi_c \, \sin(\theta) \, d\theta \\
&= -12b_1 Q^2 - 12\left[a_1 b_2 - b_1 a_2 - b_1\right] Q \\
&\quad - 3b_1\left[a_1^2 + b_1^2 + 2(a_2^2 + b_2^2 + a_2)\right] + 6a_1 b_2 + \psi_{c\varepsilon} Y
\end{aligned} \tag{A.8}$$

$$\begin{aligned}
\bar{\psi}_{c2}^{Cs2} &= \frac{1}{\pi}\int_0^{2\pi} \psi_c \, \sin(2\theta) \, d\theta \\
&= -12b_2 Q^2 - 12\left(a_1 b_1 - b_2\right) Q \\
&\quad - 3\left[b_2\left(2(a_1^2 + b_1^2) + a_2^2 + b_2^2\right) + 2a_1 b_1\right]
\end{aligned} \tag{A.9}$$

APPENDIX B

SELECTION AND ESTIMATION OF COMPRESSION SYSTEMS PARAMETERS

As described briefly in Chapter 3, the parameters of the four prototype compression systems are either based on available dimensions and quantities, or are chosen (and varied) to represent certain regions in the parameter space. In this Appendix, we give further details pertaining to the selection and estimation of the main dimensional and nondimensional parameters, especially those that are not discussed in the body of the thesis.

Compression System Parameters

These include inlet, exit and stagger blade angles, blade chord and span, rotor mean radius, hub-to-tip ratio, compressor inlet and exit duct lengths, plenum volume, and compressor flow-through area. Derived from these are nondimensional parameters that include the B parameter, the nondimensional duct lengths, and compressor inertia parameters. With the exception of C4, all of these dimensional and nondimensional quantities are based on actual dimensions and geometry of the first stage of the compression system at hand. In the case of C4, parameters that are not reported in the original references (e.g., some blade angles) were assigned reasonable values and the compressor characteristics were then adjusted on the basis of the Euler turbine equation using these assumed parameters. Also included are the running (spinning)

Param.	Units	C1	C2	C3	C4
l	m	0.0452	0.0452	0.0955	0.0923
h	m	0.0366	0.0366	0.1143	0.07
R	m	0.286	0.286	0.705	0.195
$\frac{R_{hub}}{R_{tip}}$	N.D.	0.88	0.88	0.85	0.6952
$\bar{\alpha}_{r1}^{in}$	deg.	0.0	0.0	13.0	0.0
$\bar{\beta}_{r1}^{out}$	deg.	41.0	41.0	36.0	68.0
γ_r	deg.	43.0	43.0	50.4	70.0
ρ	kg/m^3	1.2	1.2	1.17	1000.0
Ω	rad/s	251.33	251.33	84.0	75.4

Table B.1: Compression system parameters for different prototype systems.

speed of the rotor and fluid density. Table B.1 shows a list of this group of parameters (excluding those already listed in Table 3.1 and those which can easily be derived from these tables.)

Rotordynamic Parameters

These include rotor mass, shaft length and average radius, linear and nonlinear shaft stiffness, and average coefficient of viscous damping. Table B.2 gives a list of the nominal values used for the four prototype compression systems.

These parameters are estimated as follows. The nominal value of the mass of the rotor is approximated based on its dimensions, material, and configuration. The linear stiffness coefficient is approximated as that of a simply supported beam having a uniform circular cross section as given by the formula

$$k_X = \frac{48 E_{(shaft)} I_{(shaft)}}{L_{(shaft)}^3} \tag{B.1}$$

where $I_{(shaft)} = \frac{\pi}{4} R_{(shaft)}^4$ is the area moment of inertia of the rotor shaft, $R_{(shaft)}$ is

Param.	Units	C1	C2	C3	C4
M	kg	100.0	300.0	300.0	100.0
k_X	N/m	$(1.95)10^7$	$(9.75)10^5$	$(6.4)10^7$	$(6.95)10^6$
$L_{(shaft)}$	m	0.463	1.256	1.62	1.5
$R_{(shaft)}$	m	0.0225	0.0225	0.0775	0.042

Table B.2: Rotordynamic parameters for different prototype compression systems.

its average radius, $L_{(shaft)}$ is its axial length, and $E_{(shaft)}$ is the Young's modulus of elasticity of the shaft material and is taken as $(2.0)10^{11}$ Pa in all cases. The rotor's natural frequency is simply $\omega = \sqrt{k_X/M}$. The value of the nonlinear stiffness k_X^{ns} is linked to the linear stiffness by requiring that the total spring force (linear and nonlinear) at maximum rotor deflection is three times the force produced by the linear stiffness alone. This gives the following relation

$$\varpi = 2\nu^2/r_{max}^2 \tag{B.2}$$

The viscous damping coefficient ζ is fixed in all cases at an average value of 0.05, from which $c_X = 2\zeta\omega M$ can be calculated.

APPENDIX C

LINEARIZED EQUATIONS OF THE BASELINE MODEL

In this appendix, we give the elements of the Jocobian matrix $\mathbb{A}$ which was described in Chapter 4. For the eighth order baseline model, $\mathbb{A}$ is a constant 8×8 matrix with elements $\mathbb{A}_{ij}$ where i indicates the row number of the element in $\mathbb{A}$ (corresponding to the eight system equations given in Section 2.3.3), and j indicates the column number (corresponding to the state with respect to which the equation is differentiated). In other words, for the equation $\dot{x}_i = f_i(x_1, x_2, \ldots, x_j, \ldots)$, the element $\mathbb{A}_{ij}$ in the Jacobian matrix is given by $\mathbb{A}_{ij} = \frac{\partial f_i}{\partial x_j}$ evaluated at the equilibrium point.

We now substitute the expressions of the integrated characteristics and aerodynamic forces into the system equations, define new parameters to simplify the notation, and list the resulting equations again for convenience.

$$\begin{aligned}\dot{Q} = f_1 &= k_Q \left[\bar{\psi}_c^C(Q,a,b) - P\right] \\ &= k_Q \left[\psi_{c0} + 1 + 3(Q-0.5) - 4(Q-0.5)^3 - 6(a^2+b^2)(Q-0.5) - P\right]\end{aligned} \tag{C.1}$$

$$\dot{P} = f_2 = k_P \left[Q - \gamma\sqrt{P}\right] \tag{C.2}$$

$$\dot{a} = f_3 = k_{a1}\bar{\psi}_c^{Cc}(Q,a,b,X) \; - \; k_{a2}b$$

$$= k_{a1}\left\{-3a\left[4Q(Q-1)+(a^2+b^2)\right]+\psi_{c\varepsilon}X\right\} \; - \; k_{a2}b \tag{C.3}$$

$$\dot{b} = f_4 = k_{b1}\bar{\psi}_c^{Cs}(Q,a,b,Y) \; + \; k_{b2}a$$

$$= k_{b1}\left\{-3b\left[4Q(Q-1)+(a^2+b^2)\right]+\psi_{c\varepsilon}Y\right\} \; + \; k_{b2}a \tag{C.4}$$

$$\dot{X} = f_5 = V_X \tag{C.5}$$

$$\dot{V}_Y = f_6 = -2\zeta\nu\; V_X - \nu^2 X - \varpi X^3 + \chi(F_X^{ae})_i$$

$$= -2\zeta\nu\; V_X - \nu^2 X - \varpi X^3$$

$$+ \chi\left[\frac{1}{4}\chi^{tu}\left\{b\;\left(\tau_{c1}+2\tau_{c2}\;Q+3\tau_{c3}\left[Q^2+\frac{1}{4}(a^2+b^2)\right]\right)+\tau_{c\varepsilon}Y\right\}\right.$$

$$+ \chi^{pr}\; W^2\; Q\; a$$

$$- \chi^{un}\; W\;\left\{k_{b1}\left\{-3b\left[4Q(Q-1)+(a^2+b^2)\right]+\psi_{c\varepsilon}Y\right\}+k_{b2}a\right\}\Big] \tag{C.6}$$

$$\dot{Y} = f_7 = V_Y \tag{C.7}$$

$$\dot{V}_Y = f_8 = -2\sigma^{da}\zeta\nu\; V_Y - \sigma^{st}\nu^2 Y - \sigma^{ns}\varpi Y^3 - G_Y$$

$$+ \chi\left[-\frac{1}{4}\chi^{tu}\left\{a\;\left(\tau_{c1}+2\tau_{c2}\;Q+3\tau_{c3}\left[Q^2+\frac{1}{4}(a^2+b^2)\right]\right)+\tau_{c\varepsilon}X\right\}\right.$$

$$+ \chi^{pr}\; W^2\; Q\; b$$

$$+ \chi^{un}\; W\;\left\{k_{a1}\left\{-3a\left[4Q(Q-1)+(a^2+b^2)\right]+\psi_{c\varepsilon}X\right\} \; - \; k_{a2}b\right\}\Big] \tag{C.8}$$

where the the new coefficients are defined as

$$k_Q = \frac{S}{2\mathcal{L}} \qquad\qquad k_P = \frac{1}{2SB^2\mathcal{L}}$$

$$k_{a1} = k_{b1} = \frac{S}{2(m+\mu)} \qquad\qquad k_{a2} = k_{b2} = \frac{\lambda}{m+\mu} = \nu^{rs}$$

The elements of the Joacobian matrix evaluated at an equilibrium point $\mathbf{x}_e$ are

given below. Note that only nonzero elements are listed.

$$\mathbb{A}_{11} = \left.\frac{\partial f_1}{\partial Q}\right|_{\mathbf{x}_e} = k_Q[3Q_e - 12(Q_e - 0.5)^2 - 6(a_e^2 + b_e^2)] \tag{C.9}$$

$$\mathbb{A}_{12} = \left.\frac{\partial f_1}{\partial P}\right|_{\mathbf{x}_e} = -k_Q \tag{C.10}$$

$$\mathbb{A}_{13} = \left.\frac{\partial f_1}{\partial a}\right|_{\mathbf{x}_e} = -12k_Q(Q_e - 0.5)a_e \tag{C.11}$$

$$\mathbb{A}_{14} = \left.\frac{\partial f_1}{\partial b}\right|_{\mathbf{x}_e} = -12k_Q(Q_e - 0.5)b_e \tag{C.12}$$

$$\mathbb{A}_{21} = \left.\frac{\partial f_2}{\partial Q}\right|_{\mathbf{x}_e} = k_P \tag{C.13}$$

$$\mathbb{A}_{22} = \left.\frac{\partial f_2}{\partial P}\right|_{\mathbf{x}_e} = -\frac{\gamma k_P}{2\sqrt{P_e}} \tag{C.14}$$

$$\mathbb{A}_{31} = \left.\frac{\partial f_3}{\partial Q}\right|_{\mathbf{x}_e} = k_{a1}[-3(8Q_e - 4)a_e] \tag{C.15}$$

$$\mathbb{A}_{33} = \left.\frac{\partial f_3}{\partial a}\right|_{\mathbf{x}_e} = k_{a1}[-12Q_e(Q_e - 1) - 9a_e^2 - 3b_e^2] \tag{C.16}$$

$$\mathbb{A}_{34} = \left.\frac{\partial f_3}{\partial b}\right|_{\mathbf{x}_e} = k_{a1}(-6a_e b_e) - k_{a2} \tag{C.17}$$

$$\mathbb{A}_{35} = \left.\frac{\partial f_3}{\partial X}\right|_{\mathbf{x}_e} = k_{a1}\psi_{c\varepsilon} \tag{C.18}$$

$$\mathbb{A}_{41} = \left.\frac{\partial f_4}{\partial Q}\right|_{\mathbf{x}_e} = k_{b1}[-3(8Q_e - 4)b_e] \tag{C.19}$$

$$\mathbb{A}_{43} = \left.\frac{\partial f_4}{\partial a}\right|_{\mathbf{x}_e} = k_{b1}(-6a_e b_e) + k_{b2} \tag{C.20}$$

$$\mathbb{A}_{44} = \left.\frac{\partial f_4}{\partial b}\right|_{\mathbf{x}_e} = k_{b1}[-12Q_e(Q_e - 1) - 3a_e^2 - 9b_e^2] \tag{C.21}$$

$$\mathbb{A}_{47} = \left.\frac{\partial f_4}{\partial Y}\right|_{\mathbf{x}_e} = k_{b1}\psi_{c\varepsilon} \tag{C.22}$$

$$\mathbb{A}_{56} = \left.\frac{\partial f_5}{\partial V_X}\right|_{\mathbf{x}_e} = 1.0 \tag{C.23}$$

$$\mathbb{A}_{61} = \left.\frac{\partial f_6}{\partial Q}\right|_{\mathbf{x}_e} = \chi\left\{\left[\frac{1}{4}\chi^{tu}b_e(2\tau_{c2} + 6\tau_{c3}Q_e)\right] + \left[\chi^{pr}W^2 a_e\right] - \left[\chi^{un}W\mathbb{A}_{41}\right]\right\} \tag{C.24}$$

$$\mathbb{A}_{63} = \left.\frac{\partial f_6}{\partial a}\right|_{\mathbf{x}_e} = \chi\left\{\left[\frac{3}{8}\chi^{tu}\tau_{c3}a_e b_e\right] + \left[\chi^{pr}W^2 Q_e\right] - \left[\chi^{un}W\mathbb{A}_{43}\right]\right\} \tag{C.25}$$

$$\mathbb{A}_{64} = \left.\frac{\partial f_6}{\partial b}\right|_{\mathbf{x}_e} = \chi\left\{\left[\frac{1}{4}\chi^{tu}\left(\tau_{c1} + 2\tau_{c2}Q_e + 3\tau_{c3}(Q_e^2 + \frac{1}{4}a_e^2 + \frac{3}{4}b_e^2)\right)\right] - \left[\chi^{un}W\mathbb{A}_{44}\right]\right\} \tag{C.26}$$

$$\mathbb{A}_{65} = \left.\frac{\partial f_6}{\partial X}\right|_{\mathbf{x}_e} = -\nu^2 - 3\varpi\ X_e^2 \tag{C.27}$$

$$\mathbb{A}_{66} = \left.\frac{\partial f_6}{\partial V_X}\right|_{\mathbf{x}_e} = -2\zeta\nu \tag{C.28}$$

$$\mathbb{A}_{67} = \left.\frac{\partial f_6}{\partial Y}\right|_{\mathbf{x}_e} = \chi\left\{\left[\frac{1}{4}\chi^{tu}\tau_{c\varepsilon}\right] - \left[\chi^{un}W\mathbb{A}_{47}\right]\right\} \tag{C.29}$$

$$\mathbb{A}_{78} = \left.\frac{\partial f_7}{\partial V_Y}\right|_{\mathbf{x}_e} = 1.0 \tag{C.30}$$

$$\mathbb{A}_{81} = \left.\frac{\partial f_8}{\partial Q}\right|_{\mathbf{x}_e} = \chi\left\{\left[-\frac{1}{4}\chi^{tu}a_e(2\tau_{c2}+6\tau_{c3}Q_e)\right] + \left[\chi^{pr}W^2 b_e\right] + \left[\chi^{un}W\mathbb{A}_{31}\right]\right\} \tag{C.31}$$

$$\mathbb{A}_{83} = \left.\frac{\partial f_8}{\partial a}\right|_{\mathbf{x}_e} = \chi\left\{\left[-\frac{1}{4}\chi^{tu}\left(\tau_{c1}+2\tau_{c2}Q_e+3\tau_{c3}(Q_e^2+\frac{3}{4}a_e^2+\frac{1}{4}b_e^2)\right)\right] + \left[\chi^{un}W\mathbb{A}_{34}\right]\right\} \tag{C.32}$$

$$\mathbb{A}_{84} = \left.\frac{\partial f_8}{\partial b}\right|_{\mathbf{x}_e} = \chi\left\{\left[-\frac{3}{8}\chi^{tu}\tau_{c3}a_e b_e\right] + \left[\chi^{pr}W^2 Q_e\right] + \left[\chi^{un}W\mathbb{A}_{34}\right]\right\} \tag{C.33}$$

$$\mathbb{A}_{85} = \left.\frac{\partial f_8}{\partial X}\right|_{\mathbf{x}_e} = \chi\left\{\left[-\frac{1}{4}\chi^{tu}\tau_{c\varepsilon}\right] + \left[\chi^{un}W\mathbb{A}_{35}\right]\right\} \tag{C.34}$$

$$\mathbb{A}_{87} = \left.\frac{\partial f_8}{\partial V_Y}\right|_{\mathbf{x}_e} = -\sigma^{st}\nu^2 - 3\sigma^{ns}\varpi\, Y_e^2 \tag{C.35}$$

$$\mathbb{A}_{88} = \left.\frac{\partial f_8}{\partial Y}\right|_{\mathbf{x}_e} = -2\sigma^{da}\zeta\nu \tag{C.36}$$

BIBLIOGRAPHY

[1] ABED, E., HOUPT, P., AND HOSNY, W. "Bifurcation Analysis of Surge and otating Stall in Axial Flow Compressors". *ASME Journal of Turbomachinery, Vol. 115* (Oct. 1993), pp. 817–824.

[2] AKIN, J., FEHR, V., AND EVANS, D. "Analysis and Solution of the Rotor Instability Problem in the Advanced Model TF30 P111+ Engine". AIAA-88-3166 (1988).

[3] ALFORD, J. "Protecting Turbomachinery from Self-Excited Rotor Whirl". *ASME Journal of Engineering for Power* (Oct. 1965), pp. 333–334.

[4] BAGHDADI, S. "Modeling Tip Clearance Effects in Multi-stage Axial Compressors". ASME Paper 95-GT-291 (1995).

[5] BRENNEN, C. *Hydrodynamics of Pumps.* Concepts ETI and Oxford University Press, New York, 1994.

[6] CHILDS, D. *Turbomachinery Rotordynamics, Phenomena, Modeling & Analysis.* John Wiley, New York, 1993.

[7] COLDING-JORGENSEN, J. "Prediction of Rotor Dynamic Destabilizing Forces in Axial Flow Compressors". *ASME Journal of Fluid Engineering, Vol. 114* (Dec. 1992), pp. 621–625.

[8] CRANDALL, S. "The Physical Nature of Rotor Instability Mechanisms". *Applied Mechanics Division, ASME, Vol. 55* (June 1983), pp. 1–18. The Applied Mechanics, Bioengineering, and Fluids Engineering Conference, Houston, Texas.

[9] CUMPSTY, N. *Compressor Aerodynamics.* Longman Scientific and Technical, Essex, England, 1989.

[10] CUMPSTY, N., AND GREITZER, E. "A Simple Model for Compressor Stall Cell Propagation". *ASME Engineering for Power, Vol. 104* (Jan. 1982), pp. 170–176.

[11] DAY, I. *Axial Compressor Stall.* PhD thesis, Cambridge University, 1976.

[12] DAY, I. "Stall and Surge in Axial Flow Compressors". In *Axial Flow Compressors.* von Karman Institute for Fluid Dynamics, Lecture Series 1992-02, 1992.

[13] DAY, I. "Review of Stall, Surge and Active Control in Axial Compressors". Eleventh International Symposium of Air Breathing Engines, ISABE 93-7011 (1993), pp. 97–105.

[14] DAY, I. "Stall Inception in Axial Flow Compressors". *ASME Journal of Turbomachinery, Vol. 115* (Jan. 1993), pp. 1–9.

[15] DAY, I. "Axial Compressor Performance During Surge". *AIAA Journal of Propulsion and Power, Vol. 10* (June 1994), pp. 329–336.

[16] DEN HARTOG, J. *Mechanical Vibration.* Dover Publications Inc., 1985.

[17] EASTLAND, A. "Investigation of Compressor Performance in Rotating Stall: I–Facility Design and Construction and Initial Steady State Measurements". Tech. Rep. 164, Massachusetts Institute of Technology, Gas Turbine Lab Report, 1982.

[18] EHRICH, F. *Handbook of Rotordynamics.* McGraw-Hill Inc., New York, 1992.

[19] EHRICH, F. "Rotor Whirl Forces Induced by the Tip Clearance Effect in Axial Flow Compressors". *Journal of Vibrations and Acoustics, Vol. 115* (Oct. 1993), pp. 509–515.

[20] EHRICH, F. "Nonlinear Phenomena in Dynamic Response of Rotors in Anisotropic Mounting Systems". *Special 50th Anniversary Design Issue, Transactions of the ASME, Vol. 117* (June 1995), pp. 154–161.

[21] EHRICH, F., 1997-2000. Massachusetts Institute of Technology, Gas Turbine Lab, Personal Communication.

[22] EHRICH, F., SPAKOVSZKY, Z., MARTINEZ-SANCHEZ, M., SONG, S., WISLER, D., STORACE, A., SHIN, H.-W., AND BEACHER, B. "Unsteady Flow and Whirl-Inducing Forces in Axial-Flow Compressors. Part II – Analysis". ASME-IGTI Paper 2000-GT-0566 (2000).

[23] EMMONS, H., PEARSON, C., AND GRANT, H. "Compressor Surge and Stall Propagation". *ASME Transactions, Vol. 27* (Apr. 1955), pp. 455–469.

[24] EPSTEIN, A., FFOWCS WILLIAMS, J., AND GREITZER, E. "Active Suppression of Aerodynamic Instabilities in Turbomachines". *AIAA Journal of Propulsion and Power, Vol. 5* (1989), pp. 204–211.

[25] FEULNER, M., HENDRICKS, G., AND PADUANO, J. "Modeling for Control of Rotating Stall in High Speed Multi-Stage Axial Compressors". ASME Paper 94-GT-292 (1994).

[26] GAMACHE, R. *Axial Compressor Reversed Flow Performance.* PhD thesis, Massachusetts Institute of Technology, 1985.

[27] GAMACHE, R., AND GREITZER, E. "Reversed Flow in MultiStage Axial Compressors". AIAA/ASME/SAE/ASEE 22nd Joint Propulsion Conference, AIAA-86-1747 (1986).

[28] GORDON, K. *Three-Dimensional Rotating Stall Inception and Effects of Rotating Tip Clearance Asymmetry in Axial Compressors.* PhD thesis, Massachusetts Institute of Technology, 1999.

[29] GRAF, M. "Effects of Asymmetric Tip Clearance on Compressor Stability". Master's thesis, Massachusetts Institute of Technology, 1996.

[30] GRAF, M., WONG, T., GREITZER, E., MARBLE, F., TAN, C., SHIN, H.-W., AND WISLER, D. "Effects of Non-axisymmetric Tip Clearance on Axial Compressor Performance and Stability". Tech. Rep. 228, Massachusetts Institute of Technology, Gas Turbine Lab Report, 1997.

[31] GREITZER, E. "Surge and Rotating Stall in Axial Flow Compressors, Part I. Theoretical Compression System Model, Part II. Experimental Results and Comparison With Theory". *ASME Engineering for Power, Vol. 98*, No. 2 (Apr. 1976), pp. 190–217.

[32] GREITZER, E. "Review — Axial Compressor Stall Phenomena". *ASME Journal of Fluids Engineering, Vol. 102* (June 1980), pp. 134–151.

[33] GREITZER, E., EPSTEIN, A., GUENETTE, G., GYSLING, D., HAYNES, J., HENDRICKS, G., PADUANO, J., SIMON, J., AND VALAVANI, L. "Dynamic Control of Aerodynamic Instabilities in Gas Turbine Engines". *???* (1900).

[34] GREITZER, E., AND MOORE, F. "A Theory of Post-Stall Transients in Axial Compression Systems: Part II — Application". *ASME Journal of Engineering for Gas Turbines and Power, Vol. 108* (Apr. 1986), pp. 231–239.

[35] GYSLING, D. *Dynamic Control of Rotating Stall in Axial Flow Compressors Using Aeromechanical Feedback.* PhD thesis, Massachusetts Institute of Technology, 1993.

[36] HAWTHORNE, W., AND HORLOCK, J. "Actuator Disc Theory of the Incompressible Flow in Axial Compressors". *Proc. Instn. Mech. Engrs., Vol. 176*, No. 30 (1962), pp. 789–803.

[37] HAYNES, J. *Active Control of Rotating Stall in a Three-Stage Axial Compressor.* PhD thesis, Massachusetts Institute of Technology, 1993.

[38] HAYNES, J., HENDRICKS, G., AND EPSTEIN, A. "Active Stabilization of Rotating Stall in a Three-Stage Axial Compressor". *ASME Journal of Turbomachinery, Vol. 116* (Apr. 1994), pp. 226–239.

[39] HENDRICKS, G., BONNAURE, L., LONGLEY, J., GREITZER, E., AND EPSTEIN, A. "Analysis of Rotating Stall Onset in High Speed Axial Flow Compressors". AIAA paper 93-2233 (1993).

[40] HENNECKE, D. "Active and Passive Tip Clearance Control". In *Tip Clearance Effects in Axial Turbomachines*, C. Sieverding, Ed. von Karman Institute for Fluid Dynamics, Lecture Series 1985-05, 1985.

[41] HORLOCK, J. *Axial Flow Compressors.* Robert E. Krieger, New York, 1973.

[42] HORLOCK, J., AND GREITZER, E. "Non-uniform flows in axial compressors due to tip clearance variation". *IMechE, Proc. Instn. Mech. Engrs., Vol. 197C* (1983), pp. 173–178.

[43] HU, J., AND FOTTNER, L. "Calculations of Effects of Rotating Inlet Distortion on Flow Instabilities in Compression Systems". ASME paper 95-GT-196 (1995).

[44] HYNES, T., AND GREITZER, E. "A Method for Assessing Effects of Circumferential Flow Distortion on Compressor Stability". *ASME Journal of Turbomachinery, Vol. 109* (July 1987), pp. 371–379.

[45] J.A., S., AND N.A., C. "An Approximate Analysis and Prediction Method for Tip Clearance Loss in Axial Compressors". ASME Paper 93-GT-140 (1993).

[46] JEFFCOTT, H. "The Lateral Vibraion of Loaded Shafts in the Neighborhood of a Whirling Speed—The Effect of Want of Balance". *Philosophical Magazine and Journal of Science* (1919), pp. 304–314.

[47] KOCH, C. "Stalling Pressure Rise Capability of Axial Flow Compressor Stages". *ASME Journal of Engineering for Power, Vol. 103*, No. 4 (1981), pp. 645–656.

[48] LAVRICH, P. *Time Resolved Measurements of Rotating Stall in Axial Compresors.* PhD thesis, Massachusetts Institute of Technology, 1988.

[49] LITANG, Y., E. A. "Blade Tip Destabilizing Forces and Instability Analysis for Axial Rotors of Compressor". Proceedings of the Asian-Pacific Conference on Aerospace Technology and Science, 1st, Hangzhou, China, Accession No. A95-40315 (Oct. 1994), pp. 793–798.

[50] LONGLEY, J. "Measured and Predicted Effects of Inlet Distortion on Axial Compressors". ASME paper 90-GT-214 (1990).

[51] LONGLEY, J. "A Review of Non-Steady Flow Models for Compressor Stability". ASME paper 93-GT-17 (1993).

[52] LONGLEY, J., SHIN, H.-W., PLUMLEY, R., SILKOWSKI, P., DAY, I., GREITZER, E., TAN, C., AND WISLER, D. "Effects of Rotating Inlet Distortion on Multistage Compressor Stability". *ASME Journal of Turbomachinery, Vol. 118* (Apr. 1996), pp. 181–188.

[53] MATLAB, 1999. 5.3 for the PC, The MathWorks Inc.

[54] McCaughan, F. "Aplication of Bifurcation Theory to Axial Flow Compressor Instability". *ASME Journal of Turbomachinery, Vol. 111* (Oct. 1989), pp. 426–433.

[55] McCaughan, F. "Numerical Results for Axial Flow Compressor Instability". *ASME Journal of Turbomachinery, Vol. 111* (Oct. 1989), pp. 434–441.

[56] Moore, F. "A Theory of Rotating Stall of Multistage Axial Compressors: Part I. Small Disturbances; Part II. Finite Disturbances; Part III. Limit Cycles". *ASME Journal of Engineering for Gas Turbines and Power, Vol. 106* (1984), pp. 313–336.

[57] Moore, F., and Greitzer, E. "A Theory of Post-Stall Transients in Axial Compression Systems: Part I — Development of Equations". *ASME Journal of Engineering for Gas Turbines and Power, Vol. 108* (Jan. 1986), pp. 68–76.

[58] Murai, H., and Itoh, H. "Pressure Fluctuations in Axial Flow Pump Induced by Transient Cavitation". Cavitation in Hydraulic Structures and Turbomachinery, FED, Vol. 25 (1985), pp. 111–118.

[59] Murai, H., and Watanabe, H. "Pressure Fluctuations Induced by Cavitation in an Axial-Flow Pump at Partial Discharge". Symposium on Hydraulic Machinery in the Energy Related Industries, International Association for Hydraulic Research (Aug. 1984), pp. 316–340.

[60] Nayfeh, A., and Balachandran, B. *Applied Nonlinear Dynamics.* Wiley Series in Nonlinear Science. John Wiley, 1995.

[61] Nayfeh, A., and Mook, D. *Nonlinear Oscillations.* Wiley Classic Library. John Wiley, 1979.

[62] Nayfeh, M. *Bifurcation Control of Stall and Surge in Aeroengine Compression Systems.* PhD thesis, University of Maryland, 1999.

[63] Paduano, J., Epstein, A., Valavani, L., Longley, J., Greitzer, E., and Guenette, G. "Active Control of Rotating Stall in a Low Speed Axial Compressor". *ASME Journal of Turbomachinery, Vol. 115* (1993), pp. 48–56.

[64] Paduano, J., Valavani, L., Epstein, A., Greitzer, E., and Guenette, G. "Modeling for Control of Rotating Stall". *Automatica, Vol. 30*, No. 9 (Sept. 1994).

[65] Paduano, J. D., Greitzer, E., Epstein, A., Guenette, G., Gysling, D., Haynes, J., Hendricks, G., Simon, J., and Valvani, L. "Smart Engines: Concepts and Application". *Integrated Computer-Aided Engineering* (1993), pp. 3–28.

[66] SMITH, G., AND CUMPSTY, N. "Flow Phenomena in Compressor Casing Treatment". *ASME Journal of Engineering for Gas Turbines and Power, Vol. 106* (1984), pp. 532–541.

[67] SMITH, L. "The Effect of Tip Clearance on the Peak Pressure Rise of Axial-flow Fans and Compressors". *ASME Symposium on Stall* (1958), pp. 149–152.

[68] SMITH, L. "Casing Boundary Layers in Multistage Axial-Flow Compressors". *Proceedings of the Symposium on Flow Research on Blading* (1969), pp. 275–304.

[69] SONG, S., AND CHO, S. "Non-Uniform Flow in a Compressor Due to Asymmetric Tip Clearance". ASME-IGTI Paper 2000-GT-0416 (2000).

[70] SONG, S. J., AND MARTINEZ-SANCHEZ, M. "Rotordynamic Forces Due to Turbine Tip Leakage, Parts I and II". *ASME J. of Turbomachinery, Vol. 119* (Oct. 1997), pp. 695–713.

[71] SPAKOVSZKY, Z. "Analysis of Aerodynamically Induced Whirling Forces in Axial Flow Compressors". ASME-IGTI Paper 2000-GT-0418 (2000).

[72] SPAKOVSZKY, Z. *Applications of Axial and Radial Compressor Dynamic System Modeling.* PhD thesis, Massachusetts Institute of Technology, 2000.

[73] STORACE, A., WISLER, D., SHIN, H.-W., BEACHER, B., EHRICH, F., SPAKOVSZKY, Z., MARTINEZ-SANCHEZ, M., AND SONG, S. "Unsteady Flow and Whirl-Inducing Forces in Axial-Flow Compressors. Part I – Experiment". ASME-IGTI Paper 2000-GT-0565 (2000).

[74] STORACE, A. F. "A simplified method of predicting the stability of aerodynamically excited turbomachinery". Proceedings of the 6th workshop on rotordynamic instability problems in high performance turbomachinery, Texas A&M (1990), pp. 272–286.

[75] THOMAS, H. J. "Unstable Natural Vibration of Turbine Rotors Induced by the Clearance Flow in Glands and Blading". *Bull. De l'A.I.M., Vol. 71, No. 11/12* (1958), pp. 1039–1063.

[76] VAN SCHALKWYK, C. *Active Control of Rotating Stall With Inlet Distortion.* PhD thesis, Massachusetts Institute of Technology, 1996.

[77] VAN SCHALKWYK, C., PADUANO, J., GREITZER, E., AND EPSTEIN, A. "Active Stabilization of Axial Compressors with Circumferential Inlet Distortion". ASME Paper 97-GT-279 (1997).

[78] VANCE, J. *Rotordynamics of Turbomachinery.* John Wiley, New York, 1988.

[79] VANCE, J. M., AND LAUDADIO, F. J. "Experimental Measurements of Alford's Force in Axial Flow Turbomachinery". *ASME J. Eng. Gas Turbines and Power, Vol. 106* (July 1984), pp. 585–590.

[80] WANG, Y. *Effects of Actuator Limits in Bifurcation Control with Applications to Active Control of Fluid Instabilities in Turbomachinery.* PhD thesis, California Institute of Technology, 2000.

[81] WEIGL, H. *Active Stabilization of Rotating Stall and Surge in a Transonic Single Stage Axial Compressor.* PhD thesis, Massachusetts Institute of Technology, 1997.

[82] WEIGL, H., PADUANO, J., FRÉCHETTE, L., EPSTEIN, A., GREITZER, E., BRIGHT, M., AND STRAZISAR, A. "Active Stabilization of Rotating Stall and Surge in a Transonic Single Stage Axial Compressor". ASME Paper 97-GT-411 (1997).

[83] ZWILLINGER, D. *Handbook of Differential Equations.* Academic Press, Inc., 1992.